Characterizing the 2D Properties of Protoplanetary Disks Using Thermo-Chemical Modeling Techniques and High-Resolution Observations

by

Jenny Calahan

A dissertation submitted in partial fulfillment
of the requirements for the degree of
Doctor of Philosophy
(Astronomy and Astrophysics)
in the University of Michigan
2023

Doctoral Committee:

Professor Edwin Bergin, Chair
Professor Fred Adams
Professor Nuria Calvet
Professor Ke Zhang

Jenny Calahan
jcalahan@umich.edu
ORCID iD: 0000-0002-0150-0125

DEDICATION

This thesis is dedicated to my Grandmas: Lois Krantz and June Calahan. They are strong, independent women that I've been looking up to for my whole life. They are where I get my strong sense individualism and the confidence that is required to dare to get a PhD. They made personal sacrifices for the benefit of their children and families, and thanks to them, the sky was the limit for me and my brother. I believe if she was afforded the same opportunities as I had, my Grandma June would have been the first member of our family to receive a PhD. This is for you.

ACKNOWLEDGMENTS

First and foremost, I must thank my advisor Ted Bergin. Ted has the ability to see the big picture, come up with innovative ideas on the spot, and make connections between results seemingly instantaneously. This has helped tremendously in building this thesis on the fly, after his initial proposed project for me fell apart (R.I.P. the HIRMES instrument and SOFIA). In addition to being a fantastic scientific mentor and collaborator, he is an ally and advocate for graduate students within his group and for the department. The rest of my thesis committee is comprised of individuals that have played critical roles on my scientific journey. Coco Zhang was a co-advisor alongside Ted for the first two years of grad school, and taught my all I know about 2D thermo-chemical modeling. I would not be a 2D thermo-chemical modeling expert without her (or at the very least it would have taken at least one more year of grad school). I also always felt comfortable enough with her to ask my "dumb" questions, which are essential to ask in order to climb the steep learning curve that is the first few years of graduate school. Nuria Calvet is the reason the University of Michigan entered my radar for graduate school. My undergraduate advisor introduced me to Nuria after she gave a colloquium at the University of Arizona in 2017 and we talked about how strong of a program it was for star and planet formation research. I doubt she remembers that interaction, but it had a profound impact and I became one of hundreds if not thousands of students that Nuria has positively impacted their life. Nuria was also my favorite professor, she wants each of her students to deeply understand each topic she teaches us, and has full faith that we can even if we don't have faith in ourselves.

I also have to thank the rest of my research community, including all of my co-authors and collaborators. I feel so lucky to have found the astrochemistry and protoplanetary disk community. This is the most friendly and supportive field I have ever intersected with, and I am so honored to be given a seat at the table. Going back to undergrad, I need to profusely thank my advisor Yancy Shirley. You welcomed me into your research group with enthusiasm, which made me feel like I belonged in this field. You ensured that I got over a hundred hours on the 12m, and that experience was not only a blast, but really set me up for success and helped me stand out in graduate applications. One of the best parts about being at Michigan, and in Ted's group, is that you always have more advisors besides Ted. Rich Teague and Coco Zhang set me up for success in my first two years here, and Merel, Arthur, and Jane helped me reach the finish line. To my future collaborators and advisors, I am so excited to keep working with you! I am particularly energized by my peers, future leaders in this field who will advance this field beyond what we are dreaming about today. This is includes (but certainly not limited to) Majo, Marbeley, Levi, Charles, Abby, Samantha, Alice, Teresa, and most of all Felipe - my forever science sibling. I only had the 2022 Berlin and 2023 Gordon conferences to meet my peers in person so I am sure I am missing some names.

My graduate experience was made memorable and enjoyable by the graduate student community at the University of Michigan. The graduate students here are so intelligent, kind, hilarious, and above all caring. I have made life-long friends here at Michigan, and cannot express how lucky I feel to have found this graduate community. Annie and Irene, especially, have seen me at some of my lowest-lows and highest-highs and continue to love and support me in ways that confuse my brain. In addition to the graduate students at Michigan, I must also acknowledge and thank the graduate students involved in Astrobites. This was yet another supportive and powerful community that allowed me to grow as a science communicator and leader. Astrobite members continue to blow me away with their thoughtfulness and care that to bring to every initiative, no matter how small or big. Astrobites has had a profound impact on the Astronomy community and it is rarely recognized. Next time you see an Astrobite author, please buy them a coffee or tea.

While applying for postdocs, Kate Storey-Fisher reached out to me and asked if I wanted to form a “solidarity squad”. So along with Alex Gagliano and Hayley Beltz we met about once a week to work on statements, give each other advise, and to generally vent. If you are applying to postdocs soon, I highly recommend forming your own solidarity squad, they will keep you sane. We all got great jobs, and I am so excited to see what y’all do.

I must also thank my family for their unwavering support through out my entire life. Academia as a career was a foreign concept growing up, and while my parent may have thought I was crazy to pursue a major like astronomy, they never wavered in their support. My parents prioritized my and my brother’s education, and ensured that all possibilities were on the table. I know I broke my mother’s heart when I moved so far away to Tucson for undergrad, but I hope (and know) that she is proud of me for following my passion and chasing every opportunity that comes my way. I want to thank my brother, Luke, for being the sweetest, kindest, and fiercely caring brother anyone could ask for. I know you will drop everything to help me if I needed you, and I hope you know I’d do the same for you.

There are certainly people I did not name out right that have been instrumental in my happiness and success. If we ever crossed paths, thank you for being great.

TABLE OF CONTENTS

CHAPTER

LIST OF FIGURES

FIGURE

LIST OF TABLES

TABLE

LIST OF APPENDICES

LIST OF ACRONYMS

ALMA Atacama Large Millimeter Array

AU Astronomical Unit

COM Complex Organic Molecule

MMSN Minimum Mass Solar Nebula

IR Infrared

ISM Interstellar Medium

PAH Polycyclic Aromatic Hydrocarbon

SED Spectral Energy Distribution

SMA Sub-Millimeter Array

ABSTRACT

Protoplanetary disks harbor the building blocks of planet formation and are the medium in which planets start their journeys. The determination of their mass, temperature, and chemical distribution is critical, as these parameters set the stage for planet formation. Extracting these parameters requires a theoretical understanding of the protoplanetary disk environment, and supporting that theory with the highest quality observations available. In this thesis, I walk through the process of created highly-constrained 2D thermo-chemical models using sub-mm observations from the Atacama Large Millimeter Array (ALMA). These models were used to characterize the thermal structure and mass of well-studied disks, and make predictions for future JWST observations. These models also solved a chemical conundrum present in the emission in complex organic molecules, or COMs. The physical solution I present to explain COMs emission leads to a major shift in the way we understand the chemical environment present during late stage planet formation. I also observed 5 FU Ori-type objects that show a varying level of chemical complexity. Masses were determined for the ‘cloud’ and ‘disk’ component of each object.

CHAPTER 1

Introduction

Over 5,000 exoplanets have been discovered in the past 27 years, revolutionizing our understanding of our place in the Galaxy. The discovered population of exoplanets span a wide range of planetary radii, distance from host star, mass, and composition beyond what we see within our own solar system. The questions that humans have been asking since our existence suddenly becomes more complex. Not only are we wondering *How did we get here?* but now, *How could such a diversity of planetary systems come to be?* To answer these questions, we must turn to protoplanetary disks, or the birth-place of planets.

1.1 Setting the State for Planet Formation

Stars form out of clouds of dust and gas. Within massive clouds and filaments ($0.1 - 1$ parsec scales) there are over-densities of dust and gas ($\approx$ 10,000 au scales), which provide the initial conditions necessary to produce a star (or two) and planets. These over-densities may exhibit infall motion (Calahan et al., 2018) and in the center will form a hot protostar. To conserve angular momentum, the gas and dust forms a disk around the protostar (Cassen & Moosman, 1981). This disk is a circumstellar disk, or protoplanetary disk, and is the birthplace of planets.

1.1.1 Star Formation

Molecular clouds are turbulent environments with non-uniform density distributions. Within clouds, there are filimentary structures containing over-dense regions often called ‘clumps’ within which exists multiple ‘cores’. Turbulence combined with self-gravity will result in collapse of these cores to form protostars. Gravitational fragmentation will take place over scales defined by the Jean’s length, which is derived from the balance between the free-fall time and sound speed. Once a core reaches a density in which the material does not have time to react and recover against perturbations, that core enters a collapsed state. Gas pressure and magnetic fields are the main forces working against gravity. Eventually, gravity wins and a rapid collapse begins. As the density increases, opacity increases, trapping heat within the inner parts of the core. That heat halts the gravitational collapse and sends an accretion shock outward, disassociating the molecular hydrogen, triggering a second collapse. This marks the formation of the protostar (McKee & Ostriker, 2007).

1.1.2 Disk Formation

In order to conserve angular momentum, a disk of infalling material forms around the protostar. This disk acts as a transportation mechanism, continuing to accrete material on to the protostar. The radius of this disk is determined by the specific angular momentum of the system as well as the viscosity and magneto-hydrodynamic affects. The radius starts large during the collapse and infall stage. With observations, it has been shown that observed disk structures follow Keplarian rotation.

In the first million years (1 Myr) of the protostellar lifetime, the disk and protostar remain embedded in an envelope of gas and dust that will dissipate, or fall onto the disk. Streamer-like features have recently been discovered, catching this transport mechanism in the act, and potentially influencing disk substructure early in the disks' life time (Pineda et al., 2020; Kuznetsova et al., 2022). After the envelope has dissipated, the protoplanetary disk remains around the protostar for another $\sim$few Myrs (Fig. 1.3). Eventually, the disk material will dissipate, fall onto the star, or form planets and the gaseous part will be depleted. Disks with large gaps between the star and inner disk edge are thus called transition disks, thought to be a transition point between the gas-rich stage and the gas-poor phase (Calvet et al., 2002; Wyatt et al., 2015). Over time, the gas will be gone, and there remains a disk of only solid material - the debris disk. This disk contains rocky and icy material akin to the asteroid belt and Kuiper belt. The disk system will dynamically equilibrate and retain any of its planetary bodies, which we have now observed a veritable zoo of in our Galaxy.

The first indications of any disk or envelope material around young stars came from their observed spectral energy distributions, or SEDs. The SED of a single star follows a planck-function and can be estimated as a blackbody. The protoplanetary disk is comprised of cool dust and gas, and the dust emits in IR wavelengths, extending the SED beyond that of a star alone (see Figure 1.2). The slope between $\approx$3-22 μm defines the classification of a protoplanetary disk, and classes range from 0-III, with 0/I representing an embedded disk, II being the classic gas-rich protoplanetary disk, and III being a debris disk (Lada, 1987). Now, we have evidence beyond the SED that allows us to directly observe the envelope of a protostar or how gas-rich a disk may be, but those classification schemes stick around today. We now live in an era in which telescopes have much

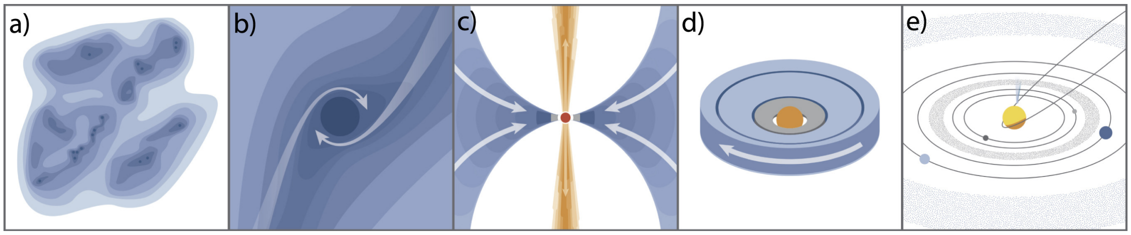

Figure 1.1 *The stages from molecular cloud to exoplanetary system from left to right. Figure 1 in Öberg et al. (2021)*

finer spatial and spectral resolution, and can resolve disk and envelope structures.

Somewhere in this schema of protoplanetary disk evolution, exoplanets undergo crucial formation stages. In order to learn about how planets form, we must find ways to characterize each of these stages of disk evolution. Only now do we have the tools to resolve the two-dimensional (height vs radius) mass, density distribution, and chemical abundances throughout a protoplanetary disk. ALMA is a radio interferometer that supplies us with a spatial resolution to resolve protoplanetary disks down to 10s of au scales. ALMA and many other telescopes have the spectral resolution to resolve individual emission lines which allows us to highly constrain temperatures and emitting areas, which can be used to infer the disks physical and chemical properties. JWST promises an exciting future, giving us an IR view of the terrestrial-planet forming zone within protoplanetary disks, which is otherwise nearly impossible to view from the Earth. In addition to these observing tools, computer simulations and modeling has made significant improvement over the years and now can take into account the temporal evolution of thousands of chemical species and their influence on the temperature structure of a disk. This information is combined to create simulated observations, which can reproduce multiple high-resolution observations simultaneously, giving us insight into the physical and chemical processes of the protoplanetary disk. This is an extremely exciting time to be learning about the planet-forming disk.

1.2 The Anatomy of a Protoplanetary Disk

1.2.1 Class II Protoplanetary Disks

After the envelope of material has dispersed, a young star is left with a gas-rich protoplanetary disk. Protoplanetary disks consist of three main components: (1) the gaseous disk (2) the large-grain dust disk and (3) the small-dust population. The gas and small dust population extends significantly above and beyond the large-grain dust disk. Each of these components are observed in different ways, and then must be considered simultaneously in order to understand the full planet-forming environment.

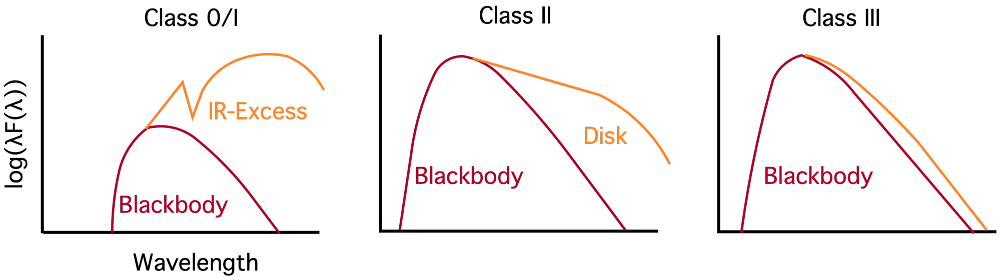

Figure 1.2 *Example SEDs for different classifications of young stellar object with accompanying disk or envelope. Figure modified from Lada (1987)*

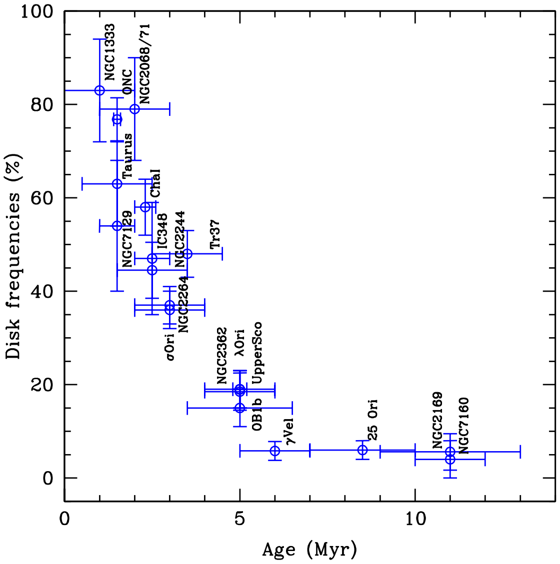

Figure 1.3 *The occurrence rate of protoplanetary disks over group lifetime (Hernández et al., 2007, 2008)*

Large-Dust Disk: The large-dust disk is arguably the most accessible out of the three populations, as dust thermal-emission dominates the total flux across sub-mm wavelengths. Large-dust consists of particles greater than $\sim$1 micron, and since emitting wavelength corresponds to dust size (max grain radius $\sim 3\lambda$) the use of millimeter interferometers are required to be sensitive to and resolve the large-dust disk. The James Clark Maxwell Telescope was one of the first instruments able to observe the submillimeter disk (Koerner et al., 2001), and ability significantly increased with the SMA (sub-millimeter array). This early work (i.e. Andrews et al., 2010) showed that there were resolved large-dust grain disks surrounding protostars, thus in protoplanetary disks there is significant dust evolution in terms of dust grown and settling beyond what is found in the ISM. There is clear dust grain size evolution strongly impacts the formation of planets. Here dust evolution is the growth of grains to larger sizes and their gravitational settling to a dust rich midplane (Weidenschilling, 1977). One of the first large programs that focused on protoplanetary disks with ALMA was the Disk Substructures at High angular Resolution Project (DSHARP) (Andrews et al., 2018). DSHARP surveyed twenty disks that were nearby, bright, and large. Using a beam size of $\sim$5 au, it became clear that every disk has a unique large-grain substructure (see Figure 1.4). This includes gaps and rings, often associated with the formation of planets. The presence of rings and gaps does not appear to correspond to stellar properties. While sub-mm continuum observations are easily accessible, and probe the planet-forming midplane containing echos of planet formation processes, the vast spatial extent and mass of the protoplanetary disk exists within the gaseous disk.

Gas and Small Dust: The gas and small dust (sub-micron) population co-exist as an atmosphere of the disk, surrounding the large-dust grains. This portion of the disk is flared, due to the conditions of hydro-static equilibrium assuming an isothermal vertical temperature structure (Lynden-Bell & Pringle, 1974). The surface density follows a tapered powerlaw:

$$\Sigma(r) = \Sigma_c(\frac{r}{r_c})^{-\gamma}\mathrm{exp}[-(\frac{\mathrm{r}}{\mathrm{r_c}})^{2-\gamma}]. \tag{1.1}$$

This flared structure has broad implications on the observed emission of each population, the way that radiation travels throughout parts of the disk, and temperature structure. The small dust contains the lowest amount of the total mass out of the three distinct populations, however it is incredibly important to consider the distribution of small dust while characterizing the disk, as it acts as a filter for radiation coming from the central star, which impacts temperature and chemistry. One of the ways to view the small dust population is via scattered light. Light from the star scatters off of these grains and re-radiates within the disk to a lower energy wavelength, and can be observed in the IR and optical regimes. It can be difficult to extract the surface of the small dust population using scattered light, as the brightness drops off as a function of radius squared, and the flared shape of the disk produces non-trivial projection effects (Stolker et al., 2016).

The gaseous part of the disk contains the vast majority of the total mass of the disk, however is less accessible than dust because the gas content can only be observed through molecular transitions at very narrow and specific wavelengths. The gas consists mostly of molecular hydrogen, H_2, however H_2 is extremely difficult to observe as it does not have a permanent dipole moment thus is unobservable in the lowest energy rotational transitions. Additionally, the energy difference between the first and second energetic states is large, thus in the cold disk environment the bulk of the H_2 exists in the lowest vibrational state, non-emissive in the gas. Astronomers instead turn to other molecules as mass-tracers, and use molecular ratios to determine the total mass of the disk. CO is the most common molecule after H_2 that has accessible rotational transitions, and is often used as a tracer of the gaseous population of a protoplanetary disk (i.e. Ansdell et al., 2016; Zhang et al., 2020c). Similar to DSHARP, an ALMA large-program was dedicated to survey the gaseous profile of protoplanetary disks. The Molecules at Planet-forming Scales (MAPS) project surveyed five bright and nearby disks and targeted 20 different molecular species that traced the C/N/O/S reservoir (see Fig. 1.5). This data set, similar to DSHARP, also showed that the gas population contains unique substructures that may or may not directly align with corresponding dust substructure (Law et al., 2021c).

One final population within the disk is the icy mantle around both the small and large dust grains. Molecules exist either within the gas-phase or ice-phase, primarily driven by the ambient temperature. Much of the disk is cold, less than 50 K, and many critical molecular species are frozen-out onto ice grains. Molecules like H_2O, CO_2, and complex organic molecules (COMs) have freeze out temperatures at or above 50 K thus are not observable throughout most of the spatial extent of the protoplanetary disk. Once a molecule is frozen, it cannot access its rotational transitions. The only way to directly access the icy reservoir of the disk is through absorption observations. Using a background source, either a background star or the host star itself, absorption features unique to ice species can be observed in the IR. These absorption features are complex, due to the fact that they contain a lot of information regarding the icy composition. These features are not only affected by the molecule, but what molecules are surrounding the targeted molecule, and the porosity of the ice itself (McClure et al., 2023). With JWST, these absorption features are being observed and understood in select disks with unique environments. The only other way to access the icy reservoir would be to observed disks that undergo sudden increases in temperature that sublimate species off of the ice and into the gas (see Chapter 6 of this Thesis).

Protoplanetary disks set the stage for planet formation. To best understand how planets like our own Earth, Jupiter, or other-worldly exoplanets form, we must find ways to characterize the fundamental properties of the protoplanetary disk. This includes finding ways to constrain the temperature and mass/density distribution of the gas and dust populations, and chemical abundances throughout the vertical and radial extent of the disk.

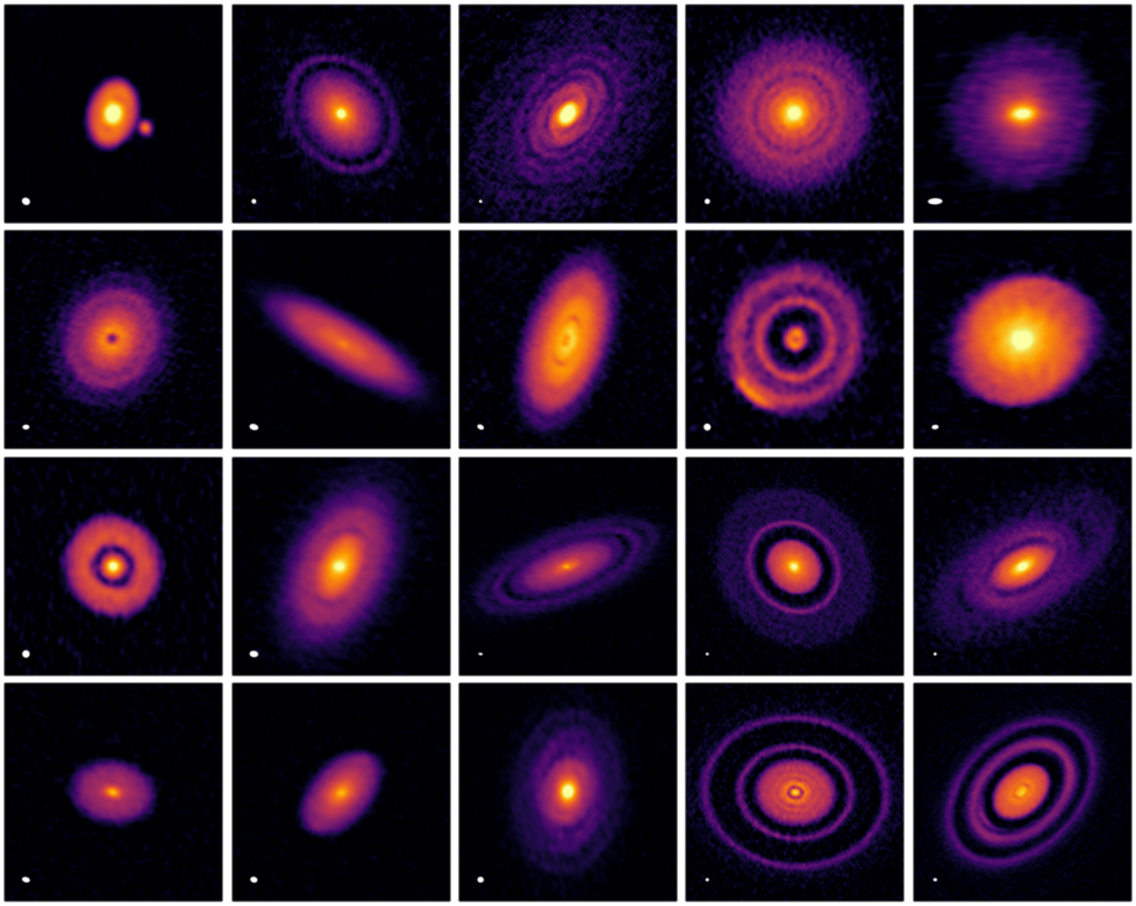

Figure 1.4 *Mosaic of protoplanetary disks observed in the DSHARP large-program. These observations highlight the large-dust population of the protoplanetary disk, and these represent highly resolved observations, going down to beam sizes (white ellipse) at* $\approx$*5 au* (Andrews et al., 2018)

1.3 Temperature, Mass, and Chemical Abundance Measurements of Protoplanetary Disks

In every scientific field, the basic properties of temperature, mass, and density are critical to understanding that subject. Protoplanetary disks are no exception. The temperature, total mass, density distribution, and chemical compositions are critical for informing planet formation theories. Temperature impacts local sound speeds and influences the derived mass and abundance of molecular species. The exact temperature throughout the disk also impacts chemistry, e.g., the rate and efficiency of reactions and whether or not a molecule is in the ice vs gas. Mass impacts the number of planets that may form, and the distribution of the disks' mass influences where and how massive each potential planet may be. The chemical distribution acts as an initial condition influencing the final chemical fingerprint of a planet. A leading question in our field is *how do planets form?*. Connecting the explosion of exoplanet detections and atmosphere characterizations to their initial conditions in planet-forming disks is the way to answer this question. Proper characterization of the base properties of a protoplanetary disks is essential.

1.3.1 Dust and Gas Temperature

The primary heating source for the disk is the protostar. The protostar will heat up the dust and gas disk, and for much of spatial extent of the disk it can be assumed that the dust and gas temperature are coupled. However, there are critical heating and cooling mechanisms that impact gas temperature only. Having a detailed view on the temperature by accounting for these specific heating and cooling mechanisms will allow for a determination of the freeze-out location for individual molecules, isolate where in the disk specific molecules are located, and play a role in whether a disk is gravitationally unstable or not. If a disk is gravitationally unstable, that is a pathway for giant planet formation and would be crucial for the evolution of the planetary system that forms out of the protoplanetary disk.

Gas-specific Heating and Cooling Mechanisms: Gas-phase heating and cooling mechanisms come from chemical reactions, gas-grain collisions, emission from energetic atomic and molecular transitions, and high-energy radiation. The formation and destruction of molecules can be associated with an energy release or sink. If a reaction releases energy into the medium, it is exothermic and heats up the surrounding area. If a reaction requires energy, it is endothermic and cools its environment. The amount of energy required or released in a particular reaction requires lab work and a theoretical understanding, and has been compiled in large reaction databases. In order to calculate the total impact of chemical reactions on the final gas temperature, one must sum up over all possible reactions and determine an overall heating or cooling factor throughout different regions

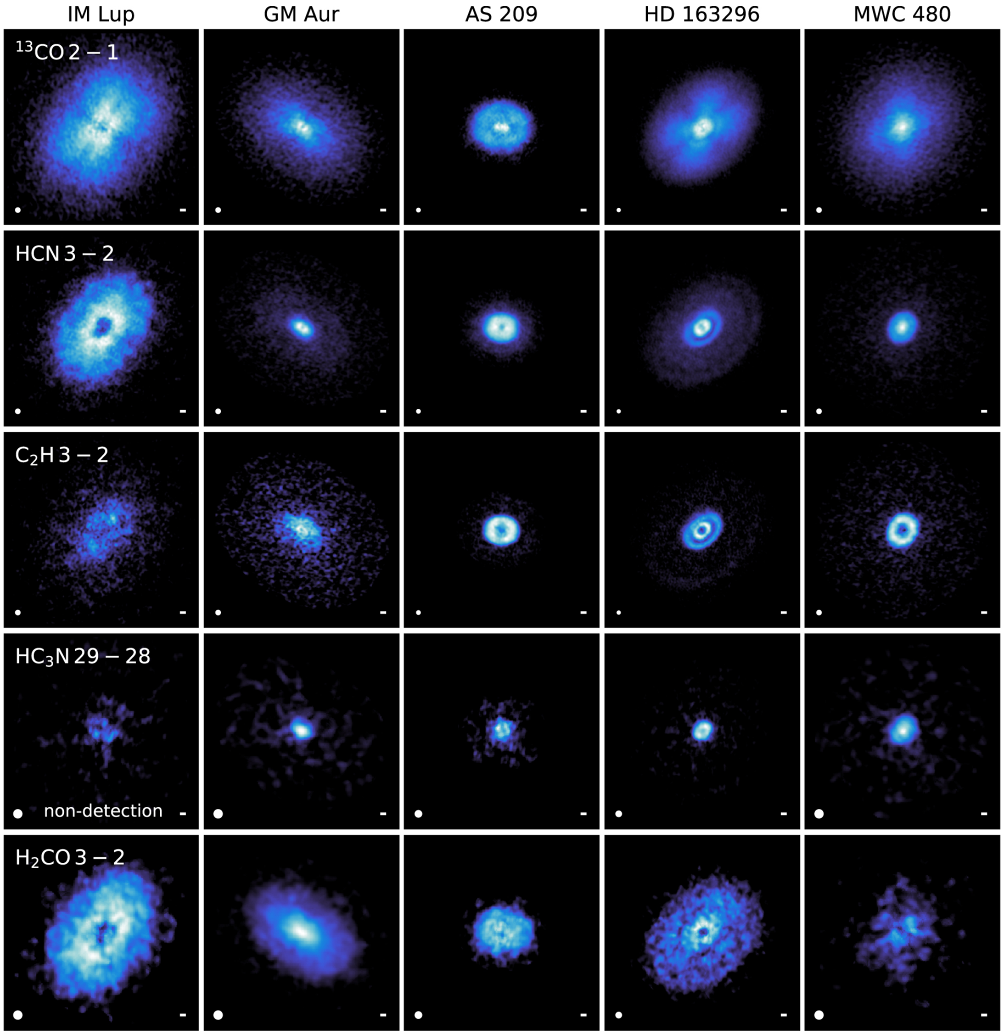

Figure 1.5 *The five MAPS disks and select molecular species that were observed. Figure 6 from Öberg et al. (2021)*

of the disk. Another key heating mechanism comes from viscous/hydrodynamic dissipation. This rate of heating depends on the density of the gas, the viscosity, sound speed, and keplarian velocity. The viscosity is a difficult value to measure, but is often assumed to be low in protoplanetary disks, as high viscosity does not reproduce observations (Hartmann et al., 1998). Viscous heating can significantly increase the gas temperature in regions of the disk that are well above the disk midplane, at very low densities. The inner disk midplane can also be highly impacted by viscous heating. There are many other mechanisms that can independently heat or cool the gas, and then there is also a chance to equillibriate the gas and dust temperature through gas-grain collisions.

1.3.1.1 How to Predict Disk Temperature:

Due to the interplay between the chemical distribution and temperature, thermo-chemical mechanisms need to be considered iteratively in order to understand the 2D temperature distrubution within a disk. One of the first attempts is Kamp & Dullemond (2004), where they assumed a photochemical equilibrium and balanced seven different heating processes, and nine cooling processes. This included photoelectric heating from PAHs and small grains, H2 collisions, formation, and dissociation, rotational lines, cosmic rays, and gas-grain collisions. The thermal mechanism that appeared to impact the final gas temperature the most was heating via the photoelectric effect from PAHs, which seemed to drive the de-coupling of the gas and dust temperature in the upper atmosphere of the disk. However, below the $\tau \gtrapprox 1$ surface of the dust, the gas and dust temperature did appear to be coupled, both primarily driven by the stellar radiation. Other notable studies that were some of the first to calculate disk gas temperature via a balance of heating and cooling mechanisms are seen in Glassgold et al. (2004); Nomura & Millar (2005); Nomura et al. (2007).

Now, there are multiple 2D thermo-chemical codes commonly used in the field today. They all have the same basic steps. Given a analytic expression of the gas and dust density structure, they complete radiative transfer calculations determining how the stellar input parameters result in a 2D dust temperature structure. That dust temperature is taken as an initial 2D gas temperature, then the iterative chemical evolution and temperature evolution calculations take place. Hundreds of molecular species with thousands of reactions can be considered along with tens of different heating and cooling mechanisms unique to the gas. These heating and cooling mechanisms are mentioned above, and the rates of heating and cooling are balanced in an ordinary differential equation (ODE) which influences changes in the temperature over time. The three most commonly used codes that follow this prescription are PRODIMO (Pinte et al., 2009), DALI (Bruderer et al., 2012; Bruderer, 2013) and RAC2D (Du & Bergin, 2014). This thesis utilized DALI and RAC2D. These thermo-chemical codes act as powerful tools that can be used to interpret observations come from ALMA, and soon from JWST. Emission from different molecules originate from unique regions of the disk, thus constraining the density and temperature from distinct regions. Reproducing multiple observations simultaneously using a thermo-chemical code not only produces a well constrained 2D density and temperature profile, but we now have the tools to explain the physical and chemical processes behind the final result. Chapter two and three of this thesis are some of the first instances of using high resolution ALMA data from multiple isotopologues of CO coming from distinct vertical emitting heights to constrain the 2D temperature using thermo-chemical modeling.

1.3.1.2 How to Observe Disk Temperature:

Under the assumption of Local Thermodynamic Equilibrium (LTE), the thermal emission from a continuum source, such as the dust emission, can be used to determine temperature. The brightness temperature (T_B) is a proxy for observed intensity, and corresponds to the temperature of a blackbody. Using the Plank function, the brightness temperature is defined by

$$T_B = \frac{h\nu}{k_B}(\ln(\frac{2\mathrm{h}\nu^3}{\mathrm{c}^2\mathrm{I}_\nu}) + 1)^{-1}. \tag{1.2}$$

When observing flux from a ratio telescope, the intensity of the emission (I_ν) is not what is directly measured, instead it is the flux density, S_ν. The flux density is defined as the intensity integrated over the beam-size of the telescope:

$$I_\nu = \frac{S_\nu}{\theta^2}. \tag{1.3}$$

Thus, the brightness temperature is an observed quantity directly from the observed flux from a radio telescope. Given optically thick emission ($\tau >$1), the brightness temperature can be assumed to be equal to the physical temperature (Weaver et al., 2018). Observations of the dust in protoplanetary disks have been used to map out the disk's temperature, and it was often assumed that the gas temperature was perfectly coupled to that of the dust.

Similar to optically thick dust emission, optically thick gas emission has a derived brightness temperature that can be assumed to be equal to the physical temperature. ^{12}CO, ^{13}CO, and C^{18}O have been seen to be optically thick in gas-rich disks, and emit from distinct vertical layers. Thus, observations alone can give us a rough 2D temperature profile within massive disks. Tools such as DISKSURF now allow for direct extraction of 2D temperature maps from optically thick observations, and this is lead to now multiple disks with directly observed 2D temperature maps (Pinte et al., 2018a; Teague et al., 2021; Law et al., 2022). These 2D maps have shown tentative correlation between gradients in the temperatures structure and gaps and rings within the dust substructure, and act as a direct constraint to results coming from 2D thermo-chemical models (see Chapter 3 of this Thesis)

1.3.1.3 Combining Observations and Models - This Thesis

2D thermo-chemical models predict gas and dust temperatures given initial chemical abundances, a series of reaction rates, a stellar spectrum, and disk gas and dust distribution. The output of these models can then be used to make simulated spectra, intensity profiles, and moment zero maps which can be directly compared to observations. Creating a model that reproduces as many observations as possible, originating from distinct regions of the disk, would then provide a highly

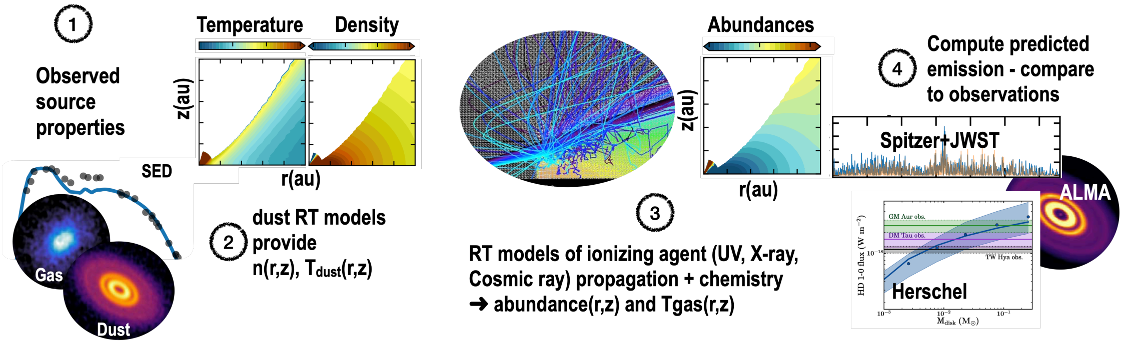

Figure 1.6 *A schematic highlighting key stages of the core work of this thesis - connection observations to 2D thermochemical models to produce 2D temperature profiles of protoplanetary disks. Image credit: M. van t' Hoff, T. Bethell, E. Bergin.*

detailed view and deep understanding of the chemistry and temperature. The goal of this thesis is to take the highest quality observations available and produce 2D models that will become the most well constrained models of individual disks. I use observations from ALMA, *Spitzer*, and *Herschel*, and make predictions for JWST. The process in which I use observations, 2D thermochemical models, and radiative transfer models is shown in Figure 1.6. 2D temperature profile determinations motivated Chapters 2 and 3 of this thesis, and led to projects that provided insight to disk mass determinations and understanding the chemical composition within planet-forming disks.

1.3.2 Disk Mass

1.3.2.1 Dust Emission

The total mass of the disk is a fundamental property that will influence the amount of material available to form planets and if the disk is gravitationally unstable. The most straightforward way to measure the mass of the disk is to measure the mass of the dust, and use the ratio between gas and dust to determine the total mass. Under the assumption that dust emission is optically thin, the mass can be derived from a measurement of the mm-continuum flux, a temperature of the dust, and an assumed dust opacity. These assumptions work for dust emission beyond $\sim$10 au of the disk (Williams & Cieza, 2011), which was the majority of the resolved emission from SMA observations. Using a max grain size of 1mm, dust temperature of 20 K, and a gas to dust ratio equal to 100, typical disk mass measurements centered around 10^{-2} $M_\odot$ (Mann & Williams, 2010). This is on the lower end of the minimum mass solar nebula (MMSN) which is the lowest required mass to reproduce the mass found in the solar system beyond the sun. There are potential flaws with these assumptions. The bulk of the dust mass is potentially in large grains ($>$10 cm) which do not emit in radio waves that ALMA nor the SMA are sensitive to. Additionally, mass may be

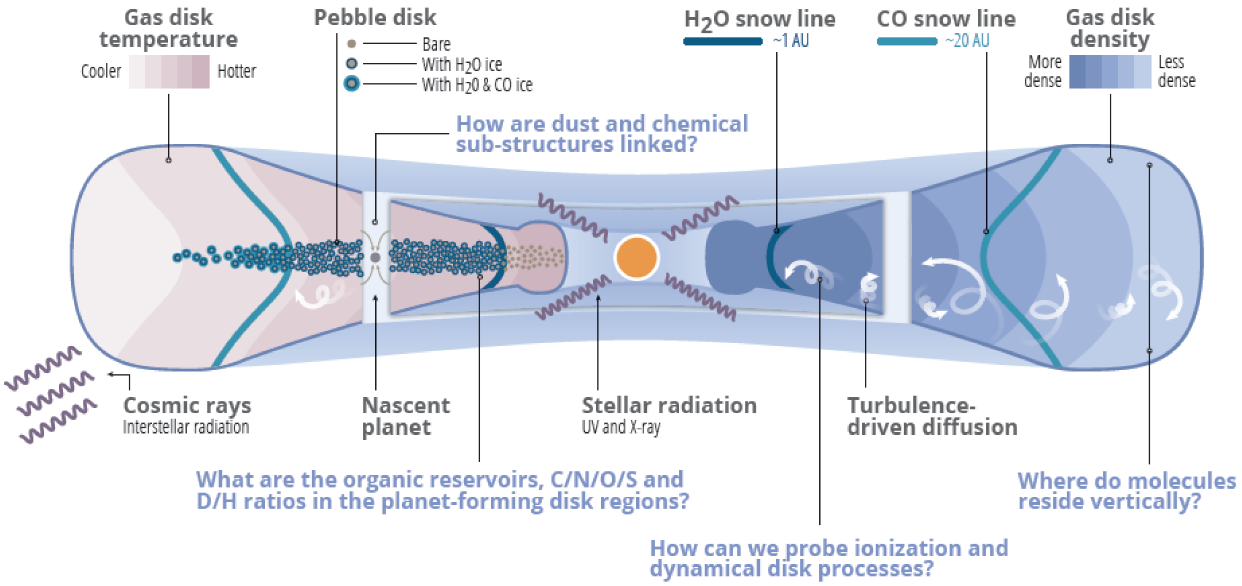

Figure 1.7 A schematic of a cross-section of a protoplanetary disk showing processes that impact chemistry andthe physical evolution of a protoplanetary disk (adapted from Öberg et al. (2021))

hidden within optically thick dust emission inside of $\approx$10 au (see Figure 1.7). The dust properties, such as opacity, albedo, and radius distribution are difficult to determine, and often degenerate with each other, however their assumed values have major implications on the final dust mass (Birnstiel et al., 2018; Manara et al., 2018).

1.3.2.2 CO Emission

CO is one of the most accessible and bright molecules observed within disks due to its high abundance, low freeze-out temperature, and strong emission at low energy rotational transitions. The ratio between CO/H_2 in the ISM has been measured to be 10^{-4} and has been assumed to be true within protoplanetary disks as well. The most abundant ^{12}CO is optically thick in most gas-rich disks, thus its emission only probes the upper regions of the molecular zone. To determine the total gas mass of the disk, optically thinner tracers are necessary. In some of the most massive gas-rich disks, observations of $^{13}C^{17}O$ showed that even $C^{18}O$ was optically thick, and that mass estimates from the optically thin $^{13}C^{17}O$ resulted in higher masses than had been previously determined (Booth et al., 2019; Booth & Ilee, 2020). $^{13}C^{17}O$ is extremely rare and likely only necessary for the most massive disks, thus most disk surveys utilize ^{13}CO and $C^{18}O$ as mass tracers. The general findings of these surveys was that CO isotopologue emission was fainter than expected, leading to gas disk masses to be lower than the MMSN and on par with single exoplanet masses, with some even lower that a Jupiter mass (Ansdell et al., 2016; Miotello et al., 2016). Using the assumptions of optically thin dust emission, this lead to dust-to-gas ratios on order of 100 or lower. Given faint

CO emission and relatively bright dust emission, this implied two possible scenarios. Either gas masses in young ($\sim$3-4 Myr) protoplanetary disks dispersed more quickly than originally thought and the bulk formation of giant gas-rich planets had already happened *or* there was significant CO chemical processing that lowered CO/H_2 ratio from the ISM value. With only CO and continuum observations, there is no solution to break this degeneracy. Alternative gas tracers are necessary.

Observations of N_2H^+ can break this degeneracy and provide constants to the CO abundance in gas. The main formation pathway to form N_2H^+ is with N_2 and $H_3{}^+$, however CO also can react with $H_3{}^+$ and form HCO^+. Additionally CO can destroy N_2H^+, thus N_2H^+ will only be abundant in the gas when CO is not present. The presence or lack of N_2H^+ then provides a constraint on the CO/H2 abundance. Determining the balance between observed CO and N_2H^+ emission and morphology and converting that in to a final gas mass requires the use of 2D thermo-chemical codes. Trapman et al. (2022) used $C^{18}O$ and N_2H^+ observations with DALI to determine likely mass ranges for three separate disks with additional mass constraints used as a benchmark (HD, see section below), and found improvements in the mass measurement by a factor of 5-10 when compared to using CO alone.

1.3.2.3 HD Emission

HD is the deuterated form of H_2, and has rotational transitions available in the far-IR. The ratio between HD and H_2 is expected to remain constant from the ISM to disk phase because these two molecules are chemical identical, making HD a robust mass tracer. *Hershel* was the last telescope sensitive to the wavelength regime in which HD transitions emit, and had three successful detections of HD within protoplanetary disks: TW Hya, DM Tau, and GM Aur. Determining the total gas mass from an HD observation requires an assumed 2D temperature profile which can be best determined by 2D thermo-chemical codes (see Chapter 2 of this Thesis). The derived gas masses from these HD detections were larger than was was determined from CO alone, suggesting the CO depletion theory as opposed to depleted gas mass (McClure et al., 2016). More observations of HD are pressing, as it is one of the most robust mass tracers available, however with the retirement of *Herschel* and no clear successor, HD remains hidden from view. Balloon missions and future mid-IR probes are currently being proposed.

1.3.3 How Chemical Abundances are Calculated in 2D Thermo-chemical Codes

The abundance and distribution of a molecule is critical information to (a) determine the chemical fingerprint inherited onto exoplanets and (b) reproduce and understand observed emission from protoplanetary disk and make total mass estimates of the disk. In a thermo-chemical modeling context, determining the abundance of a certain species will depend on the formation and destruction rates, and whether or not the species is frozen-out onto the dust.

The formation and destruction of molecules in the gas-phase is dominated by two-body reactions. Chemical networks must be included in the 2D thermo-chemical calculation, and reaction rates are determined based on a series of constants measured in laboratory experiments and the surrounding temperature. The reaction rate coefficient is given by

$$k = \alpha(\frac{T}{300})^{\beta}\exp(\frac{-\gamma}{\mathrm{T}})\mathrm{cm}^3\mathrm{s}^{-1} \tag{1.4}$$

where α, β, and γ (activation energy) are determined in the lab or otherwise estimated. These values are catalogued in the UMIST Database for Astrochemistry (McElroy et al., 2013). Also included in UMIST and other networks are surface-chemistry reactions, or reactions for frozen-out molecules on the surface of dust grains. There are specific two-body surface reactions that we know to be active and essential in the formation of H_2 and CH_3OH (Hasegawa et al., 1992). Whether a molecule is in the gas or the ice will determine the type of chemistry it can be involved in, thus careful determination of absorption and desorption (a molecule/atom attach or detach to a dust grain/ice mantel) are also considered. The adsorption of a species onto a grain is dependent on the dust density, sticking coefficient, cross section of dust grains, and thermal speed of the species which in turn rely on the gas temperature and mass of the species. There are multiple ways to desorb a species off of the grains, primarily through an increase in the temperature. The rate of thermal desorption is determined by the characteristic vibrational frequency and desorption energy unique to each species and the surrounding dust temperature. There is also desorption due to high energy photons, UV, X-ray, and Cosmic rays. These desorption rates are determined by constants unique to each molecular species determined in the lab and the rate of each high energy photon (see Du & Bergin (2014) for a detailed description of each desorption and adsorption rate accounted for in RAC2D).

Compounded all together, 2D thermo-chemical codes determine the chemical abundance of each molecular species by solving and ordinary differential equation (ODE) balancing the rates of formation, destruction, adsorption, and desorption for each dictated timestep. Solving these ODEs is time consuming but necessary, and provide a map of the chemical evolution of a certain species. This can go on to explain chemical abundances within each unique disk environment.

1.4 Chemical Composition - Critical Molecules for This Thesis

Beyond the bulk fundamental properties of a protoplanetary disk (temperature and mass) the distribution and abundance of specific molecular species are of particular interest. Here I highlight just a few of the interesting molecular conundrums and open questions in the field that are touched on in this thesis.

1.4.1 CO and its Isotopologues

As previously mentioned, CO is one of the most abundant species in the disk and is a powerful mass and temperature tracer. Its most abundant isotopologues are ^{13}CO, C^{18}O, C^{17}O, ^{13}C^{18}O, and finally ^{13}C^{17}O. The ratios between the isotopes are assumed to be as follows (Wilson, 1999):

$$^{12}\mathrm{C}/^{13}\mathrm{C} = 69 \pm 6$$
$$^{16}\mathrm{O}/^{18}\mathrm{O} = 557 \pm 30$$
$$^{18}\mathrm{O}/^{17}\mathrm{O} = 3.6 \pm 0.2$$

These values were measured based on ISM observations, however appear to remain consistent with protoplanetary disks (Qi et al., 2011; Booth et al., 2019). ^{12}CO becomes optically thick to UV rays at relatively low gas densities, thus can protect deeper ^{12}CO from photodissociating while ^{13}CO and C^{18}O are unprotected and will photodissociate at a faster rate. This will impact where the different isotopes of oxygen and carbon are distributed among various molecules (Miotello et al., 2016). For example, there is a region in the disk where ^{16}O is 'locked-in' to CO while ^{18}O is free to find a new host. This is explored alongside water UV-shielding in Chapter 4.

1.4.2 HD

HD (hydrogen deuteride) is an isotopologue of H_2, and has an electric dipole moment, making it multiple orders of magnitude more emissive than H_2 at the temperatures of protoplanetary disks. The bulk of the deuterium made in the universe came from the Big Bang, and the ratio between D/H does not change considerably within our local bubble (radius of $\sim$100-300 pc around our sun), with variations across the Galaxy that have been mapped out (Linsky et al., 2006). With a reliable D/H ratio, HD can be used as a mass tracer directly to the bulk gas mass. The HD J=1-0 line is the transition that has been used to observe a small handful of disks with *Herschel*. The J=1-0 line is not densely populated at the low temperatures expected within protoplanetary disks, its fractional population is proportional to $\exp -128.5\mathrm{K}/\mathrm{T}_{\mathrm{gas}}$ (Bergin et al., 2013). This makes the assumed mass of an HD J=1-0 flux highly dependent on temperature. This motivates Chapter 2, and provides a distinct example of a precise temperature determination is powerful.

1.4.3 Carbon-rich Species

Complex organic molecules (COMs) are defined as a molecule with six or more atoms, at least one of which must be carbon. One of the most common COMs is CH_3OH, which is thought to primarily exist within the ice-phase within cold protoplanetary disks, and thus has not been widely observed in cold gas-rich disks (Walsh et al., 2016). CH_3OH has, however, been widely observed in earlier stages of star and planet formation, including starless cores, hot cores, and the Class 0/I phases (Nazari et al., 2022). CH_3CN is also a COM, and has been a relatively common observational feature when targeted towards Class II protoplanetary disks (Bergner et al., 2018). Approximately 10 disks have targeted and have successful observed spatially resolved CH_3CN emission. These observations appear to be quite unique compared to other carbon-rich species, the emission appears to be uniformally centrally peaked, and brighter than models had expected based on the lack of gas-phase CH_3OH emission (Walsh et al., 2014). CH_3CN is a symmetric-top molecule, thus has two unique rotation axes. One of those rotational transitions rely only on collisions, thus sensitive only to the density and temperature of the medium, not the radiation field. This makes CH_3CN a strong density and temperature probe using rotational diagram analysis (see Loomis et al., 2018, for first example in a Class II disk). These observations of multiple lines of CH_3CN showed that this emission was coming from cold temperatures, and densities associated with close to the midplane of the disk (Ilee et al., 2021). This presented a conundrum, as it was unclear why CH_3CN and molecules like it (HCN, HC_3N) would exist in the gas when then should be frozen-out onto grains. Early work used reactive desorption, meaning that while CH_3CN was formed via surface reactions, there could be enough energy in that reaction to desorb the molecule from the grain. These reaction rate are difficult to measure in a lab, thus the rates necessary in modeling efforts are difficult to support with laboratory evidence. I present a unique solution to this conundrum that relies instead on the radiation environment of the disk, and is explored in Chapter 4.

1.4.4 Water

Water is one of the primary oxygen carriers and is fundamental to life as we know it. Where a planet forms in relation to the water snowline will greatly influence the amount of water on the planet. Inside the water snowline, water will be in the gas-phase, thus not frozen-out onto the icy pebbles and included in the pebble accretion that builds the seeds of planets. Water-rich exoplanets likely formed outside of the water snowline, where they accreted large amounts of the aqueous ice mantels surrounding dust grains. Our Earth, on the other hand, is relatively water poor and likely attained its critical mass of water from accretion of hydrated asteroid bodies. Since water freezes out at relatively high temperatures ($>$100 K), the spatial extent of water vapor-rich gas in a protoplanetary disk is extremely small (within $\sim$1 au around a typical solar-type star) and not easily resolvable with any instrument sensitive to water. ALMA has detected HDO and $H_2^{18}O$ in Class 0/I envelopes and disks and out-bursting objects (van't Hoff et al., 2022; Tobin et al., 2023), and otherwise evidence of a water reservoir has eluded radio frequencies. The bulk of the water reservoir emits in the IR, thus JWST is sensitive to bright water emission. JWST does not spatially resolve the water-emitting region, but will instead provide a spectrum from a few μm out to $\approx$20 μm. From that spectra, we will want to characterize the water-environment which overlaps with the terrestrial planet forming region.

The water abundance, temperature, and emitting regions can be extracted from JWST spectra. First, "slab" models will be used, which consider a slab of gas at a single temperature and density. The easiest version of these slab models assume LTE conditions, and in initial attempts to use LTE slab models do not reproduce all features well (JDISCs team, priv. communication). Non-LTE modeling may offer a better solution, however the clear next step is to consider the 2D physical and chemical processes that can impact water abundance, gas temperature, and thus their emission. This motivates Chapter 5 of this thesis, were I use a 2D thermo-chemical code and implement water self-shielding and add known chemical heating terms to determine the expected spectra of $H_2^{18}O$. $H_2^{18}O$ will likely probe more of the water reservoir as $H_2^{16}O$ will be optically thick high up in the atmosphere of the disk, thus the ratio between $H_2^{16}O$ and $H_2^{18}O$ is also determined.

1.5 This Thesis

This thesis comprises five chapters beyond this introduction and final conclusion that include published work by the Astrophysical Journal and Nature Astronomy. All chapters revolve around the ability of characterizing protoplanetary disk environments using 2D thermo-chemical modeling and high resolution observatinos. The first two chapters are examples of extracting a 2D temperature profile of protoplanetary disks with a vast array of high resolution ALMA data. The first of which focuses on TW Hya: one of the most commonly observed with multiple highly-resolved observations of CO isotopologues and an HD observation. Chapter 3 focuses on the HD 163296 disk and its associated MAPS data. I explore the impact on the large ring structures on the temperature profile. Chapter 4 utilizes the modeling work from chapter 1 and 3, and reproduces emission from carbon- and nitrogen-rich molecules that are sensitive to temperature and radiative environment. Reproducing these observations leads into a shift in our understanding of the radiative environment in protoplanetary disks. The fifth chapter dives into thermo-chemical modeling in the inner disk, and explores how the addition of water UV-shielding will impact the ratio between $H_2O/H_2{}^{18}O$. Chapter 6 lays out observations of a unique type of young stars: FU Ori objects. Using optically thin $C^{17}O$, masses are obtained for each system, and the molecular complexity of the icy reservoirs of each object are revealed.

CHAPTER 2

Resolving the Gaseous Thermal Profile of the Disk around TW Hya

This chapter published in the Astrophysical Journal (Calahan et al., 2021a) and was completed in collaboration with Edwin Bergin, Ke Zhang, Richard Teague, Ilsedore Cleeves, Jennifer Bergner, Geoffrey A. Blake, Paolo Cazzoletti, Viviana Guzmán, Michiel R.Hogerheijde, Jane Huang, Mihkel Kama, Romane Le Gal, Ryan Loomis, Karin Öberg, Ewine F. van Dishoeck, Jeroen Terwisscha van Scheltinga, Takashi Tsukagoshi, Catherine Walsh, David Wilner, and Charlie Qi. The paper is reproduced here under the non-exclusive rights of republication granted by the American Astronomical Society to the authors of the paper

Abstract

The thermal structure of protoplanetary disks is a fundamental characteristic of the system that has wide reaching effects on disk evolution and planet formation. In this study, we constrain the 2D thermal structure of the protoplanetary disk TW Hya structure utilizing images of seven CO lines. This includes new ALMA observations of ^{12}CO J=2-1 and C^{18}O J=2-1 as well as archival ALMA observations of ^{12}CO J=3-2, ^{13}CO J=3-2, 6-5, C^{18}O J= 3-2, 6-5. Additionally, we reproduce a *Herschel* observation of the HD J=1-0 line flux, the spectral energy distribution, and utilize a recent quantification of CO radial depletion in TW Hya. These observations were modeled using the thermo-chemical code RAC2D, and our best fit model reproduces all spatially resolved CO surface brightness profiles. The resulting thermal profile finds a disk mass of 0.025 $M_\odot$ and a thin upper layer of gas depleted of small dust with a thickness of $\sim$1.2% of the corresponding radius. Using our final thermal structure, we find that CO alone is not a viable mass tracer as its abundance is degenerate with the total H_2 surface density. Different mass models can readily match the spatially resolved CO line profiles with disparate abundance assumptions. Mass determination requires additional knowledge and, in this work, HD provides the additional constraint to derive the gas mass and support the inference of CO depletion in the TW Hya disk. Our final thermal

structure confirms the use of HD as a powerful probe of protoplanetary disk mass. Additionally, the method laid out in this paper is an employable strategy for extraction of disk temperatures and masses in the future.

Introduction

The radial and vertical (2D) thermal profile of a gaseous protoplanetary disk is difficult to uncover but has wide reaching effects on the physics, chemistry, and thus the planet formation potential of a disk. Further, temperature is often essential for estimation of other fundamental disk properties, such as the local sound speed and disk mass (Bergin & Williams, 2017). Any physical process that relies on sound speed will also be affected by temperature. Turbulent viscosity, as one example, relies on sound speed and plays an important role in the transportation and redistribution of disk material (Shakura & Sunyaev, 1973). The vertical density structure, in addition to the radial dependence, gives rise to the flaring of the disk, and is highly dependent on the thermal structure (Kenyon & Hartmann, 1995). In turn, the level of flaring sets the angle of incidence to stellar irradiation, producing strong vertical thermal gradients that lead to density profiles that deviate significantly from the derived Gaussian density profiles from assuming a vertically isothermal disk (Aikawa et al., 2002; Gorti et al., 2011; Woitke et al., 2009).

Temperature is also a determinate parameter to chemical processes. The gas temperature influences the rate of gas-phase exothermic reactions and, in particular, reactions that possess a significant activation barrier. Further, the midplane temperature controls the balance between gas-phase deposition and sublimation and thus the relative spatial composition of ices. For example, H_2O freezes out at dust temperatures lower than $\approx$ 120 K - 170 K (Fraser et al., 2001; Bergin & Cleeves, 2018), while CO freezes out below $\sim$21-25 K in TW Hya, (Bisschop et al., 2006; Fayolle et al., 2016; Schwarz et al., 2016; Zhang et al., 2017). Thus the gas/ice transition or snowline for water and CO is set by the thermal structure with water close to the star and CO at greater distances. Temperature-dependent snowlines are theorized to potentially be favorable sites for planet formation (Hayashi, 1981; Stevenson & Lunine, 1988; Zhang et al., 2015; Schoonenberg & Ormel, 2017). Further, across various snowlines of key elemental carriers, the relative chemical composition of the disk changes the gas/solid state balance of these carriers, which will directly influence the chemical composition of planetary atmospheres or cores at birth (e.g. C/O ratio, Öberg et al., 2011b; Öberg & Bergin, 2016).

Temperature is also essential in estimating one of the most fundamental properties of a protoplanetary disk: its mass. Assuming a constant mass ratio between gas and dust and a dust mass opacity, sub-mm thermal continuum emission is generally used as an approximate tracer for the gas mass (Bergin & Williams, 2017). However, this estimation is subject to large uncertainty as grain evolution alters the dust opacity, both spatially and temporally; compounding the issue, the growth

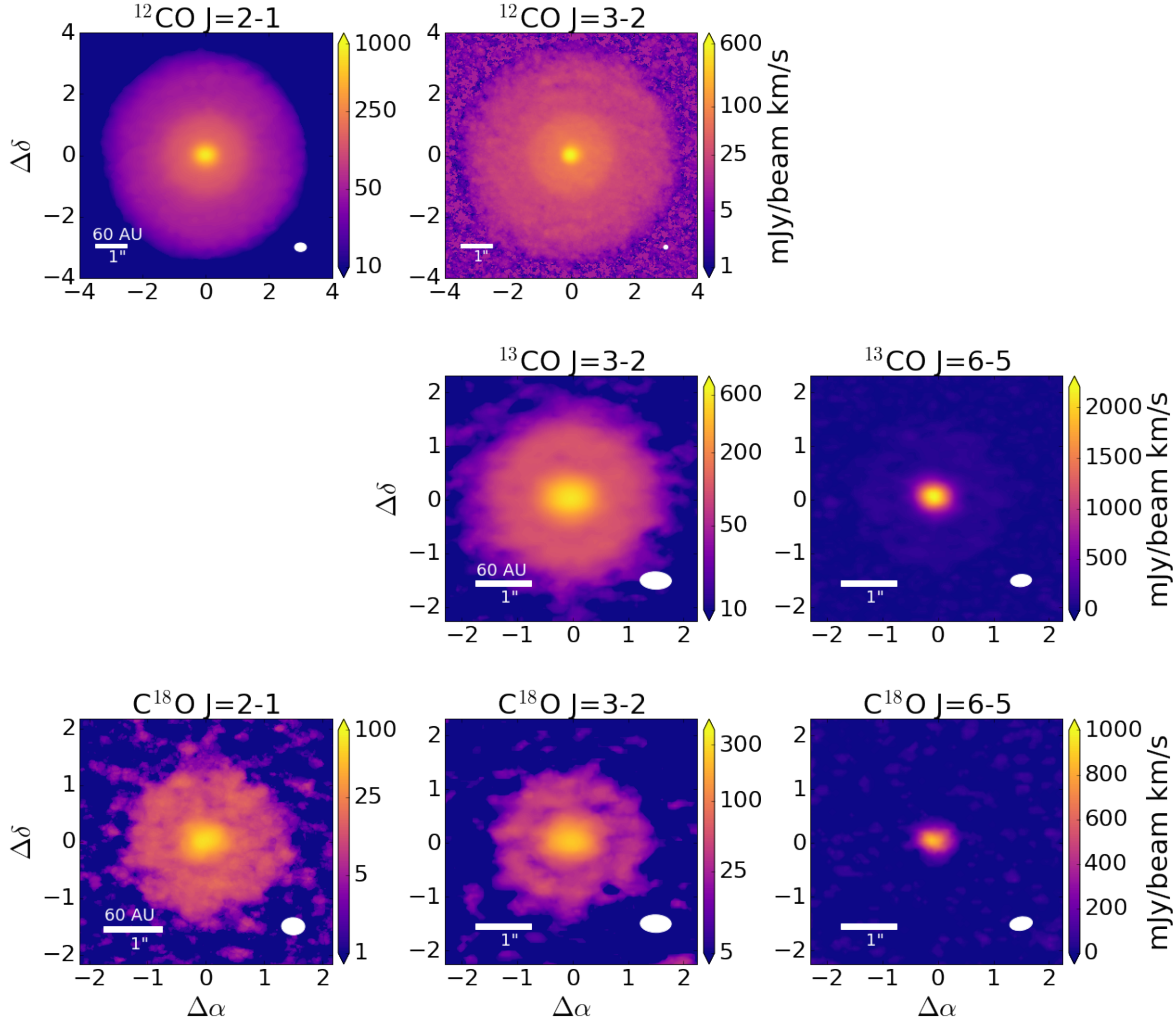

Figure 2.1 *Integrated emission maps of TW Hya in* ^{12}*CO J=2-1, 3-2,* ^{13}*CO J=3-2, 6-5, C*^{18}*O J=2-1, 3-2, and 6-5. The beam size is in the bottom right of each image. All lines of CO with the exception of the 6-5 lines are shown in log scale to amplify features. The 6-5 lines are shown on a linear scale as they have one peak and no substructure to highlight. The contour lines shown in* ^{13}*CO 3-2 and C*^{18}*O 6-5 are overlain on* ^{12}*CO 2-1 to compare emission region sizes.*

Table 2.1. ALMA Observations Summary

Program ID	P.I.	Species and Transition	Frequency (GHz)	E_{up}^{a} (K)	Beam [PA] (au × au) [°]	σ^{b} (mJy/ bm)	v_{σ}^{c} (km/ s)	I_{peak}^{d} (mJy/bm km/s)	F_{line}^{e} (Jy km/s)
2016.1.00311.S	I. Cleeves	^{12}CO J=2-1	230.538	16.6	22 × 16 [89.02]	3.9	0.56	828	17.8
2015.1.00686.S 2016.1.00629.S	S. Andrews I. Cleeves	^{12}CO J=3-2	345.795	33.2	8.3 × 7.7 [-74.96]	1.7	0.25	541	43.2
2012.1.00422.S	E. Bergin	^{13}CO J=3-2	330.587	15.9	30 × 18 [88.15]	9.2	0.09	574	4.35
2012.1.00422.S	E. Bergin	^{13}CO J=6-5	661.067	111.1	23 × 14 [-84.84]	56	0.11	2248	8.21
2016.1.00311.S	I. Cleeves	C^{18}O J=2-1	219.560	15.8	24 × 18 [87.65]	3.2	0.10	66	0.57
2012.1.00422.S	E. Bergin	C^{18}O J=3-2	329.331	31.6	30 × 18 [88.62]	12	0.11	252	1.16
2012.1.00422.S	E. Bergin	C^{18}O J=6-5	658.553	110.6	23 × 14 [-79.98]	77	0.09	973	1.56

[a] Mullet er al. 2005Müller et al. (2005)

[b] RMS Noise – measured from line free channels

[c] Velocity width assumed in RMS determination

[d] Peak Integrated Intensity Flux – errors are visualized in Figure 2.4

[e] Total Integrated Flux, calculated within a circle with radius 4“ for ^{12}CO 2-1 and 3-2; circle with radius 2“ for C^{18}O 2-1, 3-2, and ^{13}CO 3-2; and a circle with radius 1“ for C^{18}O, ^{13}CO 6-5 (See Figure 2.1). The error in the observed flux ranges from 10-15% based on the ALMA technical handbook.

to pebble sizes and larger renders a large fraction of the solids inemissive at sub-mm wavelengths and essentially undetectable (Andrews, 2020). CO emission provides an alternative method to estimate the gas mass as CO has long been used as a tracer of H_2 mass in molecular clouds. However, the conversion of line emission to column density requires a prior knowledge of the temperature, CO distribution, and opacity to account for the fact that observations generally only sample the upper state column of one rotational state. The CO abundance relative to H_2 remains relatively consistent throughout the dense ISM at approximately 10^{-4} relative to H_2 (Frerking et al., 1982; Lacy et al., 1994; Bergin & Williams, 2017; Lacy et al., 2017). In protoplanetary disks, however, CO appears to be physically depleted and such depletion varies not only disk by disk (Ansdell et al., 2016; Miotello et al., 2017; Long et al., 2017), but radially (Zhang et al., 2019, 2020a), and possibly temporally due to chemical and physical evolution (Reboussin et al., 2015; Bosman et al., 2018a; Cleeves et al., 2018; Eistrup et al., 2018; Krijt et al., 2018; Schwarz et al., 2019; Zhang et al., 2020c). All of these factors complicate the use of CO to provide a reliable estimate of the total gas mass.

HD is a promising mass tracer, as the ratio of HD/H_2 is well calibrated via measurements of the atomic D/H ratio (Linsky, 1998). However the conversion of emission of HD to mass is strongly temperature sensitive for typical temperatures between 20–50 K; this is due to the first rotational state (J = 1-0) having an E_{up} equal to 128.5 K above the ground (Bergin et al., 2013; Bergin & Williams, 2017; Kama et al., 2020a). A well constrained disk mass derived using HD, can only be determined if an accurate thermal structure is available (Trapman et al., 2017; Kama et al., 2020a).

Given the wide reaching impact of the thermal structure of a protoplanetary disk, it has long been a property sought after. Before the advent of the Atacama Large (sub-)Millimeter Array (ALMA), the spectral energy distribution (SED) and spatially unresolved gas observations provided the best available constraints for most disks. One of the first attempts to uncover a thermal structure with single dish observations was van Zadelhoff et al. (2001), which utilized isotopologues of CO, HCO^+, and HCN. By measuring the ratios of flux, they extrapolated densities and temperatures from which that flux originated. But with unresolved observations, spatial information becomes degenerate as each of the isotopologues can be sensitive to different radial and vertical layers in the disk (Gorti et al., 2011; Zhang et al., 2017; Woitke et al., 2019). Spectrally resolved observations of isotopologues have already been illuminating, shedding light onto the thermal profiles of a handful of disks, i.e. Fedele et al. (2016), which utilized both spectrally resolved and unresolved lines of high-J CO to extract thermal profiles of disks. While spatially unresolved, the spectrally resolved observations still can extract spatial information from the Keplerian rotation, if the disk inclination is known.

Spatially resolved observations allow for measurements of column densities and temperature information at different disk radii (Bruderer et al., 2012; Rosenfeld et al., 2013; Schwarz et al., 2016; Zhang et al., 2017; Pinte et al., 2018a) providing finer constraints in a forward modeling approach. Kama et al. (2016b) was one of the first to derive a thermal structure using a spatially resolved line, using CO 3-2 towards TW Hya. This resolved line in addition to much of the CO ladder produced improvements to the understanding of the TW Hya thermal profile. Towards IM Lup, Pinte et al. (2018a) observed the 2-1 transition of ^{12}CO, ^{13}CO, and $C^{18}O$ and directly extrapolated $T_{\rm gas}$ from spatially resolved optically thick lines, independent of any modeling.

The thermal structure of TW Hya has been probed using its SED in concert with a large array of spatially unresolved lines including various transitions of CO, HCO^+, and H_2O (van Zadelhoff et al., 2001; Gorti et al., 2011; Zhang et al., 2017; Woitke et al., 2019). Often these thermal profiles were empirically derived using these observations. With new thermo-chemical models that take into account radiative transfer and chemical evolution, the disk thermal structure can be derived using a forward modeling approach by reproducing observations (Woitke et al., 2019) including spatially resolved lines providing finer insight into radial structure (Kama et al., 2016b). The goals of this paper are to lay out a new approach to uncover a gaseous protoplanetary disk thermal profile by utilizing multiple spatially-resolved observations. Using a thermo-chemical code, we aim to reproduce seven spatially-resolved CO line observations towards the class II, nearby (60pc; Gaia Collaboration et al., 2018; Bailer-Jones et al., 2018), face-on TW Hya disk. It is worth noting that we do not seek to reproduce scattered light nor continuum observations. While these observations provide additional constraints on the temperature structure (more directly on the dust temperature and indirectly on gas temperature), a detailed dust model would require further assumptions on how dust properties vary with radius (Huang et al., 2018), as well as assumptions on dust scattering, which add uncertainty in dust temperature determinations (Zhu et al., 2019). Such simulated observations would be non-trivial with our current model, and the goal of this paper is to uncover the broader gaseous thermal profile and mass. While continuum and scattered light images provide insight into deviations from a smooth density distribution, that information may not translate into an effect on the gas density and temperature.

The present study uses data from the TW Hya Rosetta Stone Project (PI: Cleeves) along with other archival data sets. The complete set of observations, including the CO and isotopologue maps from Schwarz et al. (2016) and Huang et al. (2018), span a wide range of optical depths, thereby tracing both the vertical and radial temperature simultaneously when observations are spatially resolved, in the case for optically thick molecules. Molecules that turn out to be optically thin will provide column density information. Additionally, we seek to reproduce the HD flux measured with *Herschel* and the SED of the disk.

We detail our ALMA observations in Section 2.1 and our modeling procedure in Section 2.2. In Section 5.3 we explore our best fit thermal model to investigate possible model degeneracies. Comparisons to other models and the future of HD observations are explored in Section 2.4, and we summarize our findings in Section 2.5.

2.1 Observations

We present new observations of ^{12}CO 2-1 and C^{18}O 2-1 taken as a part of the Rosetta collaboration. Archival ALMA data were also used for ^{12}CO 3-2, C^{18}O 3-2, 6-5, and ^{13}CO 3-2, 6-5. The archival HD 1-0 flux measurement from *Herschel* and SED fluxes from the literature were also used. A summary of all observations can be found in Table 2.1. Using BETTERMOMENTS[1] (Teague & Foreman-Mackey, 2018), moment zero maps were calculated for each of the CO observations described below and are presented in Figure 2.1. Each moment zero map was then azimuthally averaged producing the radial emission profiles. These radial profiles provided the constraints that we used below to determine the 2D thermal structure of TW Hya.

2.1.1 CO Observations from TW Hya Rosetta Project

We report new observations of ^{12}CO 2-1 and C^{18}O 2-1 as part of the program 2016.1.00311.S (PI Cleeves). The compact observations (baselines down to 15 m) were obtained on December 16, 2016 in configuration C43-3 for a total on-source integration time of 81 minutes. The extended observations (baselines up to 1124 m) were carried out on May 5 and 7, 2017 in C43-6 with an

---

[1] https://github.com/richteague/bettermoments

on source integration time of 25 minutes. The data were calibrated by the CASA pipeline McMullin et al. (2007). For the extended observations, J1058+0133 and J1037-2934 were used as bandpass calibrators, J1107-4449 as the flux calibration, and J1037-2934 as the phase calibrator. For the compact observations, J1037-2934 was used for bandpass, flux, and phase calibration. We performed one additional round of phase self calibration on each of the extended and compact observations independently using CASA version 4.5.0. For the self calibration we adopted a solution interval of 30 seconds and averaged both polarizations. Spectral windows were not averaged in the self calibration step, and the solutions were mapped to the individual spectral windows.

Each data cube was first centered to the same central coordinate, then the continuum was subtracted from the line observations in the uv plane using the CASA routine *uvcontsub*. The continuum subtracted long and short baselines were then combined using the method *concat* where the spectral windows that excluded the lines were manually specified. The images were produced in CASA version 4.6.12 using *tclean*, with Briggs weighting and a robust parameter of 0.5. The final spectral resolution of CO and $C^{18}O$ were 246.08 kHz and 73.24 kHz respectively. The $C^{18}O$ restoring beam had FWHM dimensions of $0.''40 \times 0.''30$ and ^{12}CO had $0.''37 \times 0.''28$.

2.1.2 Archival CO Data

The ^{12}CO J = 3-2 analysis and imaging procedures are reported in Huang et al. (2018) and the ^{13}CO J = 3-2, 6-5 and $C^{18}O$ J = 3-2, 6-5 observations are described in Schwarz et al. (2016), and not repeated here. We utilize their final data reduction and images.

2.1.3 Spatially Unresolved Observations: HD Flux and SED

HD J=1-0 was observed using *Herschel* and the observed total integrated flux was $6.3(\pm 0.7) \times 10^{-18}$ W/m^2 (Bergin et al., 2013). The line is spatially unresolved, thus we only use the integrated line flux to compare the models.

TW Hya is one of the most thoroughly observed protoplanetary disks in the literature, with a well-characterized spectral energy distribution (SED). The main purpose of the SED is to constrain the thermally coupled small dust population. Data points for the SED were taken from Cleeves et al. (2015), which in turn used individual photometric measurements from the literature (Weintraub et al., 1989a, 2000; Mekkaden, 1998; Cutri et al., 2003; Hartmann et al., 2005; Low et al., 2005; Thi et al., 2010; Andrews et al., 2012; Qi et al., 2004; Wilner et al., 2000, 2003).

2.2 Modeling: RAC2D

We create a thermo-chemical model of the TW Hya disk that takes into account the gas and dust structure while simultaneously computing the temperature and chemical structure throughout the disk over time. Simulated observations are derived from the output model and compared to spatially-resolved line observations, as well as the SED and HD line flux. We use the time-dependent thermo-chemical code RAC2D (Du & Bergin, 2014). A brief description of the physical model follows; a higher-level detailed description of the code can be found in the aforementioned paper.

2.2.1 Physical Structure

Our model consists of three mass components: gas, a small dust (≤) population, and a large dust (≤ mm) population. Each population is described by a global surface density distribution (Lynden-Bell & Pringle, 1974) which has been widely used in modeling protoplanetary disks:

$$\Sigma(r) = \Sigma_c \left(\frac{r}{r_c}\right)^{-\gamma} \exp\left[-\left(\frac{r}{r_c}\right)^{2-\gamma}\right] \tag{2.1}$$

r_c is the characteristic radius at which the surface density is Σ_c and γ is the power-law index that describes the radial behavior of the surface density. Each dust population follows an MRN grain size distribution $n(a) \propto a^{-3.5}$ (Mathis et al., 1977) . The gas and small dust are spatially coupled and exist out to 200 au (van Boekel et al., 2017; Huang et al., 2018) and possess a scale height that is related to a critical radius (defined below). We assume that the large dust population is settled in the midplane and extends less than 100 au (Andrews et al., 2010). This reduced scale height approximates and represents the impact of dust evolution and pebble sedimentation to the midplane (Birnstiel et al., 2012; Krijt et al., 2016). The specific values for our TW Hya model are constrained by observation and detailed in the next section.

RAC2D is equipped with an exponential taper added to the surface density profile both in the inner and outer disk regions. This allows for more flexibility in the position of the exponential taper. If r_c is defined to be larger than the gas component (which would result in a flatter disk) an exponential taper can still be added. If we were to only use Equation 1, and required a large r_c value, there would be an abrupt cut-off at the user-defined outer radius. r_{exp} defines at what radius the exponential taper begins, and r_s describes the strength of that taper:

$$\Sigma'(r) = \Sigma(r) e^{(r - r_{\mathrm{exp_{in}}})/r_{s_{in}}}, \text{ if } r < r_{\mathrm{exp_{in}}}$$

$$\Sigma'(r) = \Sigma(r) e^{-(r - r_{\mathrm{exp_{out}}})/r_{\mathrm{s_{out}}}}, \text{ if } r > r_{\mathrm{exp_{out}}}$$

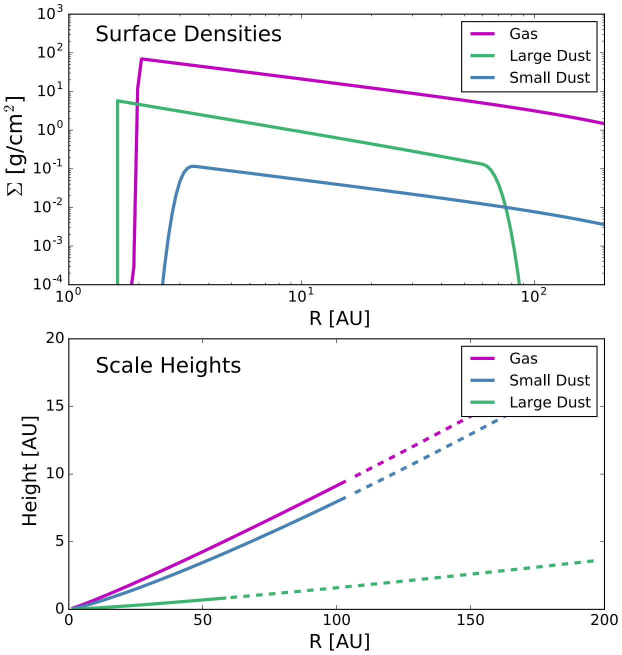

Figure 2.2 *The surface density (top) and the scale heights (bottom) of each component of our disk model. The exponential taper seen added to the surface densities at 60 au for the large dust and 104 au for the small dust and gas components. The location at which dashed line starts for the scale height also corresponds to where the exponential taper for that population begins, corresponding to a significant decrease in density.*

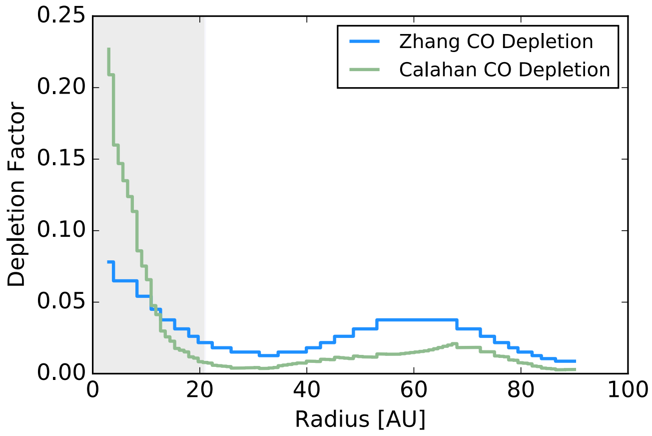

Figure 2.3 *The final radial depletion profile (green) as motivated by the depletion profiles derived in Zhang et al. (2019) (blue). CO was depleted radially according to the above factor at the beginning of the thermo-chemical calculation. The transparent grey corresponds to the beamsize of the C^{18}O 2-1 observation.*

A density profile for the gas and dust populations is derived from the surface density profile and a scale height:

$$\rho(r,z) = \frac{\Sigma(r)}{\sqrt{2\pi}h(r)} \exp\left[-\frac{1}{2}\left(\frac{z}{h(r)}\right)^2\right] \tag{2.2}$$

$$h = h_c \left(\frac{r}{r_c}\right)^{\Psi} \tag{2.3}$$

Where h_c is the scale height at the characteristic radius, and Ψ is a power-law index that characterizes the flaring of the disk structure. The final surface densities and scale heights for each component in our model is seen in Figure 2.2. In the surface density plot, we show that although all of our components (gas, small dust, and large dust) have a $\mathrm{r_c}$ value equal to 400 au, they exponentially drop off at their given $\mathrm{r_{exp_{out}}}$.

2.2.2 Dust and Gas Temperatures

After initializing RAC2D with a model density structure for each population, the code computes a dust and gas temperature. The determination of dust and gas temperature is an iterative process, allowed to change over time due to the evolving chemical composition. For the gas-phase chemistry, we adopt the reaction rates from the UMIST database (Woodall et al., 2007), with additional rates considering the self-shielding of CO, H_2, H_2O, and OH, dust grain surface chemistry driven by temperature, UV, cosmic rays, and two-body chemical reactions on dust grain surfaces (see references given by Du & Bergin, 2014). Chemical processes also provide heating or cooling to the surrounding gas. That, along with stellar and interstellar radiation drive the thermal gas structure. Our study explores models that account for 1 Myr of chemical evolution. Although the age of TW Hya is estimated to be 5-10 Myr (Debes et al., 2013), our assumed depletion profile for CO (Section 2.2.3) encapsulates the effects of earlier chemical evolution of CO. We are essentially modeling the thermal physics and chemistry after that evolution has occurred. Finally, at the end of a given run we extract the dust and gas thermal profiles and SED profile.

Simulated line images for CO, ^{13}CO, C^{18}O, and HD are necessary for our comparison to observations. We do not model isotopologue fractionation in this chemical network, as fractionation of CO is not significant in a massive disk like TW Hya (Miotello et al., 2014) . Thus, we compute ^{13}CO and C^{18}O abundances based on ISM ratios of CO/^{13}CO = 69 and CO/C^{18}O = 570 (Wilson, 1999). We then apply the depletion profile to each CO line. The HD abundance (see Table 3.2) remains constant. Given these abundances and the local gas temperature, RAC2D computes line images using a ray-tracing technique. We then manually convolve these simulated observations with the corresponding ALMA beam to make direct comparisons to data. Our HD 1-0 observations are spatially and spectrally unresolved, thus to recreate unresolved integrated flux measurements,

Table 2.2. Initial Chemical Abundances for Final Model

	Abundance Relative to Total Hydrogen Nuclei
H_2	5×10^{-1}
HD	2×10^{-5}
He	0.09
CO*	1.04×10^{-4}
N	7.5×10^{-5}
H_2O (ice)	1.8×10^{-4}
S	8×10^{-8}
Si+	8×10^{-9}
Na+	2×10^{-8}
Mg+	7×10^{-9}
Fe+	3×10^{-9}
P	3×10^{-9}
F	2×10^{-8}
Cl	4×10^{-9}

Note. — *CO has an imposed radial depletion profile as shown in Figure 3.1

we convolve our model HD line over a gaussian corresponding to the velocity resolution of the *Herschel* PACS instrument: ~300 $\mathrm{km\,s^{-1}}$ (Poglitsch et al., 2010).

The SED is created by RAC2D by counting the number of photons over a range of frequencies that interact with the disk and would fall within a given range of sight lines. Thus photons directly emitted from the star are not accounted for, a design motivated by computational efficiency. To create the final SED the input stellar blackbody of TW Hya (stellar mass = 0.8 $M_\odot$ and $T_{\mathrm{eff}} \approx$ 3400K) is added to the result produced by RAC2D.

2.2.3 Initial Parameter Setup of TW Hya

We set out to create a model which, given certain initial parameters and constraints for the disk physical state, produces a gas thermal profile that can reproduce the spatially resolved CO observations and other constraints. Our initial parameters are taken from Zhang et al. (2019) who compiled the most up-to-date constraints on disk parameters from the literature: Brickhouse et al. (2010); Andrews et al. (2012); van Boekel et al. (2017); Gaia Collaboration et al. (2018); Huang

Table 2.3. Gas and Dust Population Parameters: Ranges and Initial Values

	Gas	Small Dust (5×10^{-3} - 1)	Definition
Mass ($M_\odot$)	0.01 - [0.05] - 0.06	$2.5 \times 10^{-5} - [1 \times 10^{-4}] - 5 \times 10^{-4}$	Total Mass
Ψ	0.8 - [1.2] - 1.6	0.8 - [1.2] - 1.6	Flaring Parameter
γ	0.5 - [.75] - 1.1	0.5 - [.75] - 1.1	Surface Density Power-Index
h_c	8.4 - [42] - 84	8.4 - [42] - 84	Characteristic Height
$r_{\mathrm{exp_{out}}}$	60 - [104] - 200	60 - [104] - 200	Exponential Drop-off Radius in the Outer Disk
$r_{\mathrm{s_{out}}}$	70.7	70.7	Exponential Drop-off Strength in the Outer Disk
$r_{\mathrm{exp_{in}}}$	2	3.5	Exponential Drop-off Radius at the Inner Disk
$r_{\mathrm{s_{in}}}$	0.1	0.5	Exponential Drop-off Strength at the Inner Disk
r_{in} (au)	0.1	0.5	Inner Radius Cut-off
r_{out} (au)	200	200	Outer Radius Cut-off
r_c	400	400	Characteristic Radius

Note. — This table shows the range of parameter space explored in each variable of our thermo-chemical model, with the initial value in brackets. Since the parameter values for the large dust do not significantly impact the thermal structure, we do not explore variations in the equivalent parameters in the large dust component and keep these fixed to the Zhang et al. values (see Table 4). All length values are in units of au.

Table 2.4. Gas and Dust Population Parameters: Final Model Values

	Gas	Small Dust (5×10^{-3} - 1)	Large Dust (5×10^{-3} - 1×10^3)
Mass ($M_\odot$)	0.025	1.0×10^{-4}	4.0×10^{-4}
Ψ	1.1	1.2	1.2
γ	0.75	0.75	1.0
h_c	42	42	8.4
$r_{\mathrm{exp_{out}}}$	104	104	60
$r_{\mathrm{s_{out}}}$	70.7	70.7	10
$r_{\mathrm{exp_{in}}}$	2	3.5	N/A
$r_{\mathrm{s_{in}}}$	0.1	0.5	N/A
r_{in}	0.1	0.5	1
r_{out}	200	200	200
r_c	400	400	400

Note. — Final values of the TW Hya model that reproduces the CO, HD, and SED observations. All length values are in units of au.

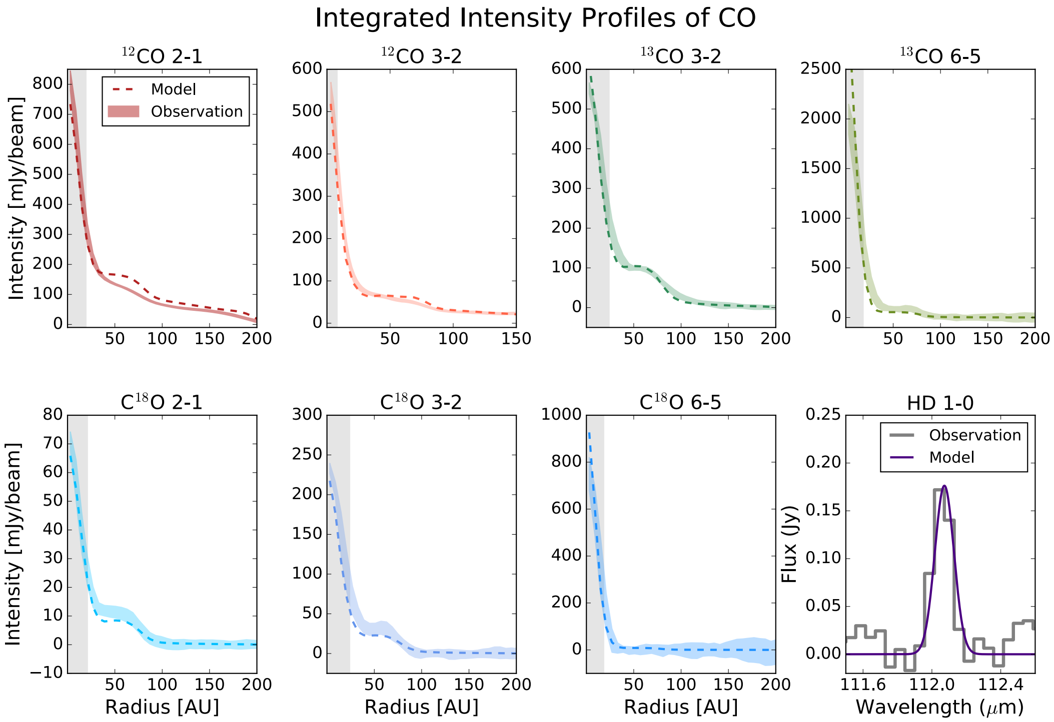

Figure 2.4 *Integrated radial intensity profiles of CO and its isotopologues ^{13}CO and $C^{18}O$. The solid lines are from observations from ALMA (see Table 2.1) and the dashed lines are from our best-fit model, and each observation's beam is shown in the filled region. The thermal profile that produced this best match to the observation is shown in Figure 2.6.*

et al. (2018). A table of source information is found in Table 3 of Zhang et al. (2019). For initial chemical abundances, we adopt values given in Table 3.2 motivated by Du & Bergin (2014) and Zhang et al. (2019). The disk inclination used is 6°, as past studies of TW Hya tend to use a range of inclination values between 5-7° (Qi et al., 2004; Andrews et al., 2012; Huang et al., 2018)

In this study, we begin with a radial CO abundance profile motivated by Zhang et al. (2019), which calculated two depletion profiles, one for ^{13}CO and one for C^{18}O. They were calculated to fit the isotopologue observations. The depletion profile dictates how much CO should be depleted from the expected total value, including both gas and solid state ($\sim 10^{-4}$ for ^{12}CO) at each radius. The difference in the observed depletion profiles between the isotopologues can be understood by differential effects between ^{13}CO and C^{18}O such as fractionation and isotopic selective self-shielding (e.g. Visser et al., 2009; Woods & Willacy, 2009; Miotello et al., 2014, 2016). Note that the impact of isotope selective self-shielding is much smaller than the overall removal of CO from the surface layers (Du & Bergin, 2014). Hence, our initial depletion profile was the average of the ^{13}CO and C^{18}O observed depletion, and is shown in Figure 3.1. In this study, we implemented the CO depletion at the start of the chemical and thermal evolution, as the lack of CO will affect the temperature structure. We found that with the Zhang et al. (2019) CO depletion profile, our simulated radial profiles did not reproduce the C^{18}O 2-1 and ^{13}CO 2-1 profiles, in particular. This is due to both the chemical processing over the timescale of 1 Myr and the change in temperature at which each of these transitions emit. Reducing the chemical time to 0.01 Myr removed the effect of chemical processing, which should be encompassed through the implemented CO depletion. Further iterations on the radial CO depletion profile were made until we reached a model that reproduced the C^{18}O 2-1 observations within the margins of uncertainty. Our final CO depletion profile is shown in comparison to that of Zhang et al. (2019) in Figure 3.1. The largest difference between the two exists within the inner 20 au where we found that we did not require as extreme a CO depletion factor. Beyond 20au the final CO depletion profile is on average 2.5 times less than what was derived in Zhang et al. (2019).

2.2.4 Parameter Exploration

This study relies on a suite of CO line observations, as each line provides information about a slightly different vertical layer within the disk (Gorti et al., 2011; Zhang et al., 2017; Woitke et al., 2019). As the CO observations were spatially resolved, the quality of model was assessed by a comparison of the radial integrated intensity profiles. We additionally seek to match the HD flux and the SED.

As a first step we set up a grid of models to explore the full parameter space. The parameter space and initial model parameters from Zhang et al. (2019) are shown in Table 2.3. Initially, we

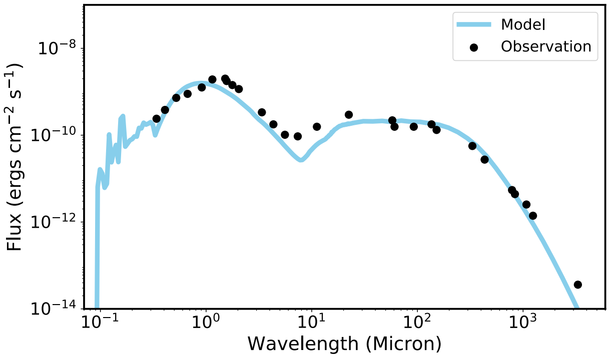

Figure 2.5 *A comparison of the photometry data that comprises TW Hya's SED and the modeled SED from RADMC3D based off of the gaseous and dust density and temperature structures from RAC2D.*

explored gas mass, small dust mass, Ψ, γ, and radii and height values within ranges supported by previous observation and modeling work. Each parameter is explored using values above and below the initial value. For the gas mass, our upper limit was 0.06 $M_\odot$ which is the upper limit quoted in Bergin et al. (2013) and the lower limit was 0.01 $M_\odot$, which is similar to some earlier estimates of TW Hya's gas mass (Weintraub et al., 1989b; Thi et al., 2010). The small dust mass range was motivated by the SED, limiting the range from factors of 2× greater than our initial value to ~3× less. Both extremes produce SEDs that do not match the observations, but values in between provide a reasonable match to the SED. The Ψ values explored vary from 0.8 to 1.3; both extremes affect the integrated CO emission profiles quite strongly. γ has an upper limit of 2 (see Equation 2.1), however, we explore smaller variations on gamma around an initial value of 0.85, thus using limits of 0.5 - 1.1. We did not explore values nearing the upper limit of two as past observational constraints on γ suggest the value for TW Hya is not much larger than 1.0 (Kama et al., 2016b; van Boekel et al., 2017; Zhang et al., 2017). While this is a narrow range, it did provide enough information to understand the trends that come from changes in γ. For $r_{exp_{\rm out}}$, h_c, and r_c, the smallest value explored was that of the large dust value, and the largest value explored was double the initial model value. We did not explore the inner nor outer edge values of r_s (see Section 2.2.1) nor the inner exponential radial cutoff $r_{\rm exp_{in}}$ as these values cannot be constrained with our CO observations. For each model we compare the model output CO isotopologue emission profiles as shown in Figure 2.4 in search of the best fit.

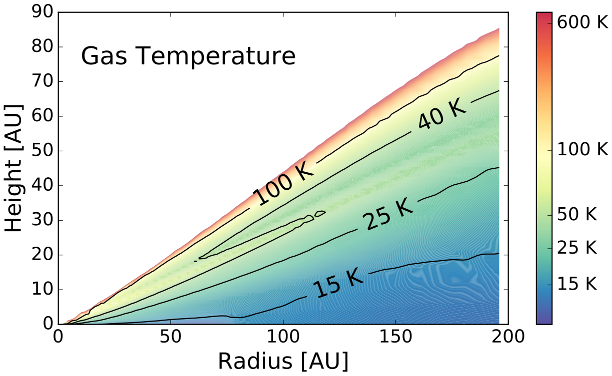

Figure 2.6 *The final 2D thermal structure of the gas that reproduces seven resolved ALMA CO lines, HD flux, and the SED. The final temperature profile is supported up to scale heights from which* ^{12}*CO 2-1 emits from, since this transition has the highest optical depth*

2.3 Results

2.3.1 Description of Best-Fit Model

We show the results of our best-fit model in Figure 2.4, 2.5, and 2.6. The model agrees well with all seven resolved CO lines available along with the HD J=1-0 flux, and the SED profile (Figure 2.5). The parameter values of the best-fit model are given in Table 3.3.

Our beginning thermal structure was from the TW Hydra disk model of Zhang et al. (2019) (see Section 2.2.3). This initial model under-represents the CO flux in the inner ∼25 au while over-representing the CO flux between 25 and 75 au particularly in the ^{13}CO J=3-2 and C^{18}O J=2-1 lines (see Figure A.1). The initial model HD line flux is 4.6×10^{-18} W m^{-2}, which is 73% of the observed value, falling outside of the quoted error of that flux measurement from Bergin et al. (2013) $6.3(\pm0.7) \times 10^{-18}$ W m^{-2}. To solve these initial discrepancies, we explore the parameter space extensively (see more details in the Appendix). We find that in order to match both CO and HD observations the Ψ values of the gas and small dust need to be slightly different (1.1 and 1.2, respectively). This difference creates a thin layer at the surface of the disk which is depleted of dust. The difference between the scale height of the gas and dust is 1.2% of the radial location (represented in Figure 2.2).

This thin layer depleted of dust is a crude way to represent the impact of coagulation and settling on the small dust population end of the assumed MRN (Dullemond & Dominik, 2004). The changing values of Ψ and thus scale heights can be seen as a way of representing a modified MRN distribution. Although the grain size distribution is not directly explored in this study, we find that the distribution of small grains strongly influences the final thermal structure. This relative change in scale height between dust and gas appears to be the best method to significantly increase the intensity of the CO emission in the inner 25 au. Gas in this thin upper layer is more effectively heated as UV radiation penetrates more easily when the dust component is reduced. This heats CO gas in slightly denser regions and increases the CO emissivity.

Summing all these effects together, our best-fit model has a total gas mass that is only half of that in Zhang et al. (2019) model. This model predicts an HD flux of 5.9×10^{-18} W m^{-2}, which is well within the uncertainty of the observed flux.

2.3.2 Best-fit SED

The simulated SED as derived by our final TW Hya model was calculated using RADMC3D (Dullemond et al., 2012a). After the temperature and physical distribution of the gas and dust were determined by RAC2D, we feed in those results including the stellar spectrum and dust opacities into RADMC3D.

Our model assumes a mass of small dust grains equal to 10^{-4} M$_\odot$ and a mass of the large dust grains to be 4×10^{-4} M$_\odot$. Using these dust components, our model SED agrees reasonably well with the observed SED, see Figure 2.5. TW Hydra also exhibits a strong silicate feature near 10 which our dust model under predicts. Previous studies that have successfully modeled this feature by utilizing a special type of silicate within 4 au (Calvet et al., 2002; Zhang et al., 2013). This is a scale much smaller than we aim to constrain, and is a small effect in comparison to the total dust opacity in this region. The SED beyond $\sim$8 tests if we are correctly representing the dust population, as the long-wavelength portion of the SED is mostly affected by dust mass, size distribution, spatial distribution, and composition (a mixture of silicates and graphite). Overall, our dust model provides a good match to the observed SED. Since the small dust population has an effect on the thermal balance, the SED provides one of the key factors to constrain the HD emission and overall disk mass.

2.3.3 ^{13}C^{18}O Flux

Using our final model, we seek to compare the observed ^{13}C^{18}O flux towards TW Hya as presented in Zhang et al. (2017). We use line information for ^{13}C^{18}O derived by HITRAN (Rothman et al., 2005), formatted to be identical to line data from the Leiden Atomic and Molecular Database. We also use an abundance ratio ^{12}CO/^{13}CO = 40, as measured by Zhang et al. (2017) for this specific observation.[2] The resultant flux is shown in Appendix Figure A.14. Overall, our model provides a good fit to the observations, underpredicting the ^{13}C^{18}O flux by at most by 12 mJy km s^{-1}

---

[2] We note that this is different than the assumed isotope ratio for the surface layers. However, it is a direct measurement and is suggested by Zhang et al. (2017) to be the result of carbon fractionation in the dense colder layers of the photodissociation region (see discussion and results in Röllig & Ossenkopf, 2013).

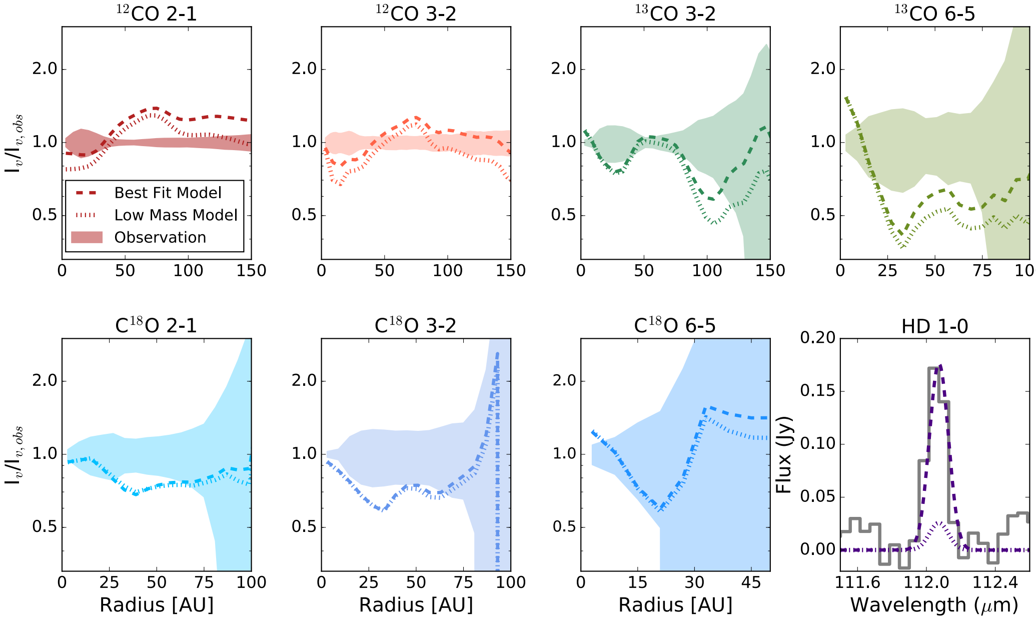

Figure 2.7 *The radial intensity profiles of the observations, best fit model, and low mass model all normalized to the observations, along with the HD flux observations compared to the simulated HD flux in the low mass model. The observations are thus located at 1, and are the solid line while the models are dashed lines with the thick dashed line representing the best fit model (see Figure 2.4) and the low mass model (with high CO abundance) represented with the thinner dashed line. Errors of the integrated intensity line profile is shown in the shaded region, and is also normalized by the observed intensity. From this comparison, we can see that both the model with a gas mass of 0.023* $M_\odot$ *and 0.0023* $M_\odot$ *have nearly identical profiles. This also shows how close our model represents the observations. The majority of the time, the modeled flux is within a factor of two of the observed, with the only exceptions being when the observations drop quickly to receive zero flux and the model does not reach zero as quickly, however the model still is within the error. This happens especially with* $C^{18}O$ *6-5. While in the low mass model, the CO remains relatively similar, the HD flux drops significantly.*

beam^{-1}, or about a factor of two across the modeled flux emitting area. As the $^{13}C^{18}O$ emission is highly centrally concentrated the location of largest discrepancy is in the central regions and also towards the observed asymmetry. This residual value is similar to the background noise flux. The asymmetry can be accounted for by simply the low signal/noise ratio for this observation.

2.3.4 CO Mass/Abundance Degeneracy

Our exploration of the parameter space shows that the CO line intensity is a degenerate result of the total gas mass and CO abundance. If the line is optically thin, the CO emission scales directly with its number density, n_{CO}, where n_{CO} is $x_{\mathrm{CO}}\times\, n_{\mathrm{H_2}}$. Even in the case of optically thick lines, as the gas density increases, CO emission becomes optically thick at a higher location of the disk atmosphere; thereby tracing temperature of a warmer region. Thus there is a degeneracy between the abundance of CO and the density of H_2 and hence the gas mass. One way to break this degeneracy is with an observed HD flux, as it is independent of CO abundance.

To explore this, we create a low-mass model based on the parameters of our best-fit model, however in this model we decrease the total gas mass by one order of magnitude while subsequently increasing in the CO abundance by the same factor. As shown in Fig. 2.7 this low mass model produces indistinguishable CO radial profiles compared to these of our best-fit model. However, the line flux of HD (1-0) transition of the lower mass model goes down by more than a factor of five (see bottom right panel in Figure 2.7). This degeneracy between CO abundance and gas mass has been reported in previous studies with less well-constrained temperature structures. (Bergin et al., 2013; Favre et al., 2013; McClure et al., 2016; Kama et al., 2016b; Trapman et al., 2017). Here we prove that the degeneracy cannot be broken even the thermal structure of the disk is well constrained. In short, CO lines alone are not sufficient to constrain the total disk mass and another independent mass tracer must be introduced, such as HD.

2.4 Analysis & Discussion

2.4.1 CO Emitting Regions

RAC2D calculates the emitting regions for each isotopologue; examples of ^{12}CO 2-1 and $C^{18}O$ 2-1 are shown in Figure 2.8. To allow for inter-molecular comparison, we then calculated the heights at which the majority of the emission originates. This is presented in Figure 2.9 where we show a visualization of the average vertical cross-section of the disk from which each line is emitting based on our final model. For comparison, a non-CO depleted model is also shown. A dashed line representing the $\tau = 1$ surface of the small dust at the frequency of the HD J=1-0 transition

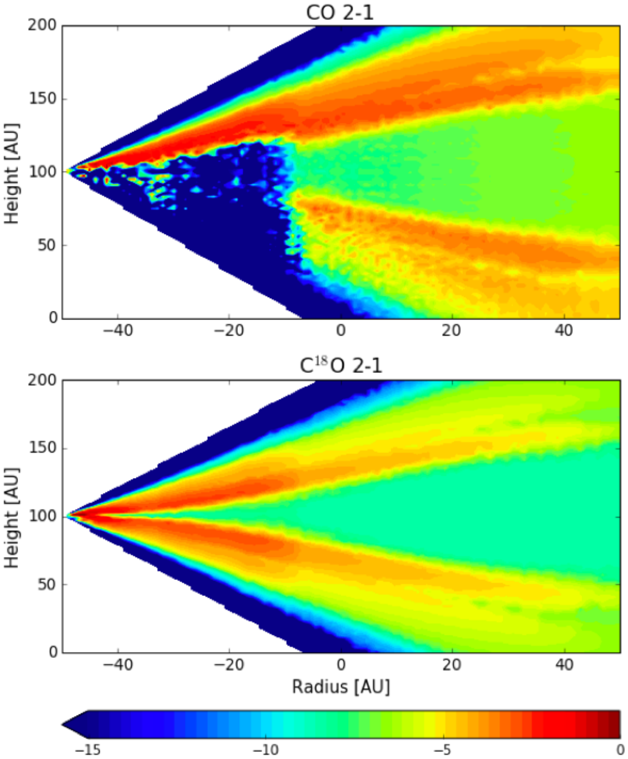

Figure 2.8 *The emitting regions of* ^{12}*CO and C*^{18}*O 2-1 in our final model. Emitting regions for each molecule were calculated based on the final model, and were used to create Figure 2.9, which encapsulates the regions in which most of each molecule is emitting from.*

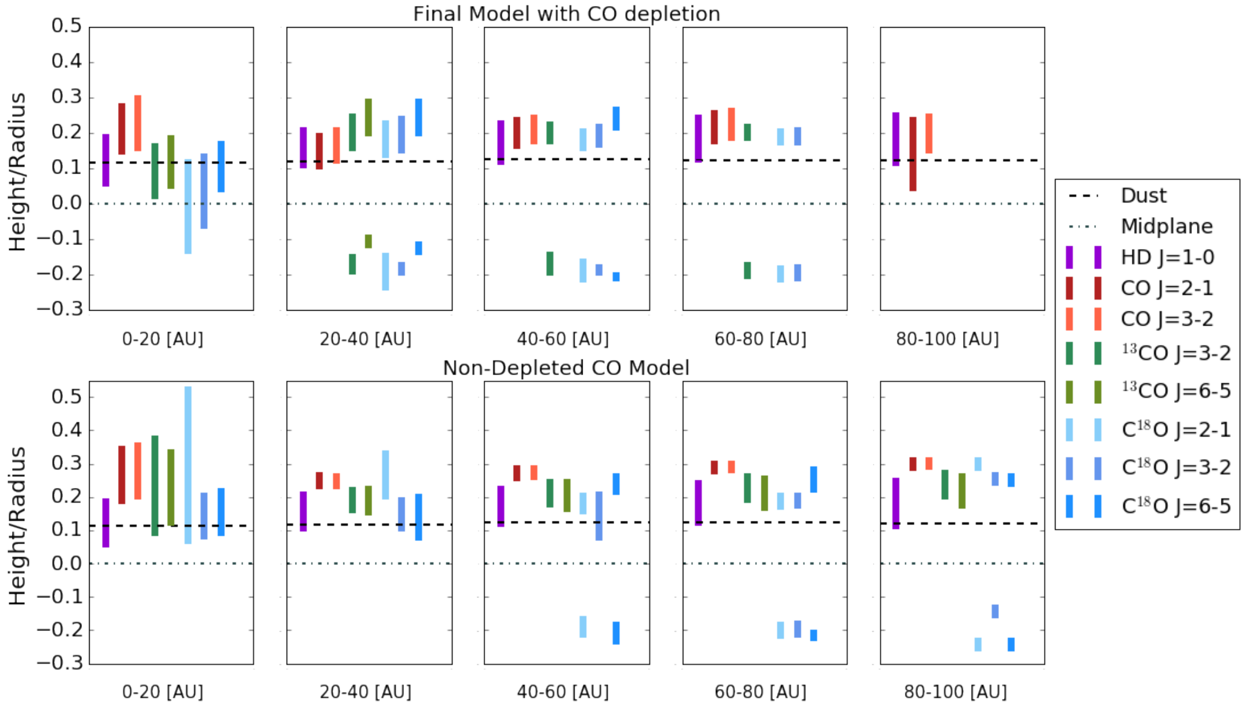

Figure 2.9 *The average vertical emitting region of each line used in this study for our final model (top) and a version of that model without assuming CO depletion (bottom). For every 20 au the average vertical emitting height was calculated. The top of each bar corresponds to the average surface which consists of 90% of the flux. The bottom of the bar and below is 10% of the total flux. Lines that have two emitting regions, one above the disk and below, are optically thin, thus observations of these molecules come from both the front and back of the disk. There is no emission in the midplane outside the CO snowline, thus for an optically thin emitter, their emitting regions were calculated twice. Once for above the midplane, then again but only from the back. The continuous* $\tau = 1$ *surface of the dust at the frequency of HD J=1-0 is shown via the dashed line. Examples of 2D contribution plots used to create this figure of* ^{12}*CO 2-1 and C*^{18}*O 2-1 are shown in Figure 2.8.*

($\lambda \simeq 112$) is plotted as a reference. These two models represent two extremes of T Tauri disks, a high CO abundance (which corresponds to a CO/H_2 ratio equal to that of the ISM) and a low CO abundance, using the relatively high CO depletion factors found in TW Hya.

In the non-depleted case, ^{12}CO emits from a higher layer than all other isotopologues, while HD and ^{13}CO and in some cases C^{18}O, probe similar depths. C^{18}O appears to be optically thin, especially past 60 au; the C^{18}O surface brightness is therefore not a sufficient temperature tracer across a disk with similar properties as TW Hya. In this instance C^{18}O probes the total column density. TW Hya is, however, is thought to exhibit severe CO depletions, thus CO and its isotopologues emission will have reduced optical depth (in comparison to the non-depleted model). In our final model, ^{12}CO 2-1, 3-2, and ^{13}CO 3-2 emit from roughly an equivalent vertical depth as HD, showing that in this disk, observations of ^{12}CO 2-1, 3-2 and ^{13}CO 3-2 best trace the layers where HD emission arises. Within radii ranging from 0 - 40 au, ^{13}CO 3-2 emission is optically thick, overlapping with the lower bound of the HD emitting layer. The C^{18}O and ^{13}CO 6-5 become optically thin beyond radii of 20-40au, thus their brightness temperature no longer constrains the disk surface temperature. Based on this result, the disk mass for TW Hya could have been accomplished using only the resolved observations of ^{12}CO 2-1, 3-2, and supplemented with ^{13}CO 3-2 alongside HD. For future observations, multiple observations of CO are still required, at least down to the 3-2 levels, as CO depletion and gas mass are not known a priori.

2.4.2 Scattered Light Effects

TW Hya has been observed in scattered light, which traces out the small dust population of the disk. These observations are reported in van Boekel et al. (2017), and using the scattered light observations they find that radial depressions in the small dust surface density are necessary to reproduce the observed surface brightness. The two largest depressions in the surface density have depths 80% and 45% at approximately 5 au and 90 au, respectively (see Figure 11 in van Boekel et al., 2017). We applied this depletion factor to the small dust population to the initial model and found that it did not strongly effect the radial profiles as shown in Figure 2.10. The depletion does increase the HD J = 1-0 flux by 30%. However, the effect on ^{12}CO and C^{18}O is much less (below 15%), and these changes do not significantly alter the fit to the CO radial profiles. Future modeling efforts may want to include information from the mm-continuum and scattered light observations as an additional constraint on the physical state of surface layers.

2.4.3 Comparison to Other Models

There are at least two other attempts to model TW Hydra with thermo-chemical codes: Kama et al. (2016a) with the DALI 2D physical-chemical code, and Woitke et al. (2019) with the ProDiMo

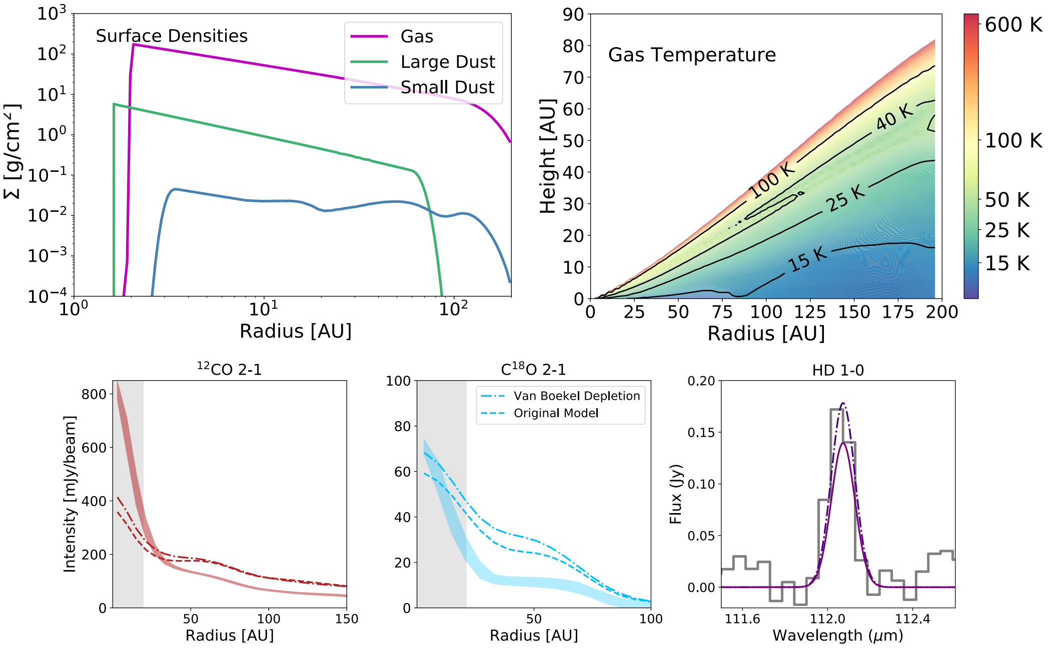

Figure 2.10 *At the upper left are the surface densities for the gas and dust populations while taking a depletion of small dust as measured by van Boekel et al. (2017) from scattered light observations. Using the new small dust population, we calculate the gas temperature (top right), the radial profiles of* ^{12}*CO and C*^{18}*O 2-1 (bottom middle, left), and HD flux. The dashed lines in the radial profile and HD flux plot show our initial model, compared to a model with a non-smooth small dust surface density as motivated by the scattered light observations.*

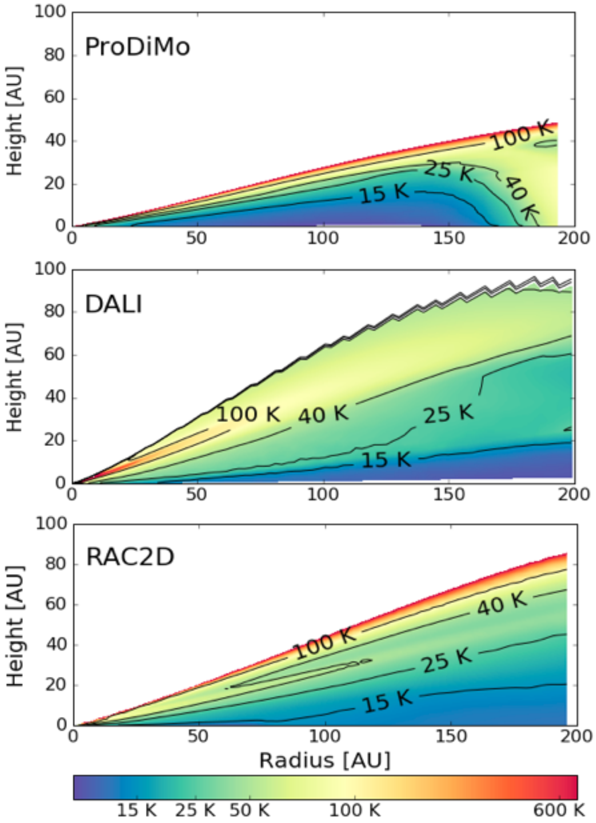

Figure 2.11 *A comparison of the gas thermal structure of TW Hya from Woitke et al. (2019), Kama et al. (2016a), and this study.*

code.

Kama et al. (2016a) focused on tracing volatile carbon in TW Hya. To do so, they modeled an underlying thermal structure of both the gas and dust population using DALI (Bruderer et al., 2009, 2012; Bruderer, 2013) which is designed and operated in a very similar way to RAC2D. This study utilized spatially unresolved observations of the CO ladder (upper limits of J=36-35, 33-32, 29-28, and line fluxes of J=18-17, 10-9, 6-5, ALMA observation of J=3-2, and SMA observation of J=2-1). Their observation of CO J 3-2 was spatially resolved. Additionally, they utilized other carbon carrier molecules (C[I], C[II], C_2H, HCO^+) to motivate their models along with HD both J=1-0 and J=2-1. Kama et al. (2016a) produced a model that reproduces their CO observations and the HD flux. DALI has since been updated to include deuterium chemistry and isotoplogue selective chemistry following work by Miotello et al. (2014). This subsequent updated model is presented in Trapman et al. (2017) and shown in Figure 2.11, alongside our RAC2D results. The main difference between Kama et al. (2016b) model and ours is that we reproduce multiple spatially resolved CO transitions. Our ∼15 - 100 K isotherms match up relatively well, which are the temperature ranges that our CO lines trace. Our solutions do diverge from each other at

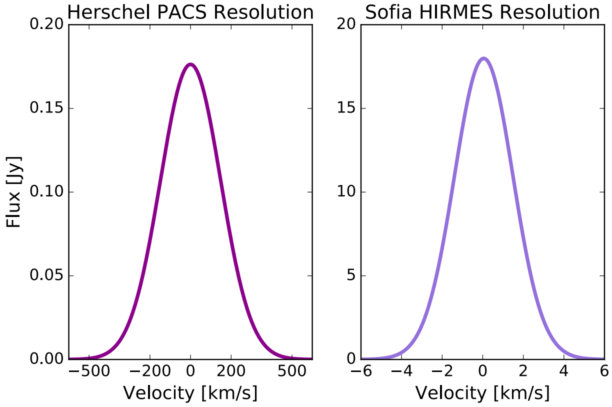

Figure 2.12 *A predicted HD spectra based on the resolution of the proposed HIRMES instrument on Sofia (right) compared to the modeled spectra of HD J=1-0 from this study using the spectral resolution of the PACS instrument.*

high temperatures (> 100K). Using the HD emission, Kama et al. (2016a) derived gas mass, and determined the same value that this study independently arrived at: 0.023 $M_\odot$.

Woitke et al. (2019) describes the DIANA project, which modeled a number of protoplanetary disks in a homogeneous way using SED-matching and the thermo-chemical code ProDiMo. Their model outputs for each disk are publicly available. Figure 2.11 shows a comparison of their results with our RAC2D model. The most noticeable difference is that our model appears to have a higher gas scale height compared to that determined by the DIANA project. Further, the DIANA model finds higher gas temperatures at the disk surface, along with a comparatively cooler midplane (e.g. compare 15 K isotherms). Woitke et al. (2019) matched many volatile lines such as CO and H_2O to within a factor of two. However they under predicted the HD emission by a factor of 13 with a total gas mass of 0.045 $M_\odot$.

Cleeves et al. (2015) also produced a TW Hya model with the primary goal of fitting molecular ion observations. In the process, this paper used SMA observations of $C^{18}O$ and ^{13}CO J=2-1 and the Herschel HD observation to constrain the physical structure. The chemical model employed was not a self consistent thermo-chemical model, however, the gas temperature structure was derived via a DALI-based fitting function to account for the gas and dust thermal decoupling in the upper layers. In the Cleeves et al. (2015) model, the derived gas mass of $0.04 \pm 0.02\,M_\odot$ is also in good agreement with our best fit model, as is the overall temperature profile.

2.4.4 Future Observations of Spatially Resolved CO Line Emission in Inclined Disks

This study serves as a proof of concept that observation and subsequent modeling of resolved CO lines and HD line flux in combination with the SED is a powerful method to uncover thermal structure and disk mass. TW Hya is an ideal disk to test out this new method, as it is has been extensively observed with ALMA and other observatories, and is one of only three disks with an HD emission detection (McClure et al., 2016). One disk parameter not explored in this particular study is disk inclination. An inclined disk will allow for direct constraints to be set on the vertical emitting layer and the subsequent temperature inferred within the layer (Pinte et al., 2018a; Teague et al., 2019a). Disk inclination will broaden the spectral line, and the degree at which that might complicate extraction of a 2D thermal structure using thermo-chemical models is worth investigation. It is also worth applying these techniques towards brighter Herbig Ae/Be disks. The CO snowline in these systems lies at greater distances from the star (Qi et al., 2015; Zhang et al., 2020a) and hence some transitions might probe layers closer to the midplane than sampled in T Tauri systems.

In our model we do not take CO fractionation chemistry into account. However, this would not effect the derived temperature structure very strongly. ^{12}CO would be unaffected and selective photodissociation has a marginal effect for ^{13}CO. There would be a larger effect for C^{18}O; however its emission is optically thin for much of the disk and thus does not provide sufficient temperature information. We also did not include rarer isotopologues of CO such as ^{13}C^{18}O (Zhang et al., 2017), which would provide additional insight into column density inside the CO snowline.

2.4.5 Future HD observations

At present, the sample of disks in which HD has been targeted is limited to a few deep observations (McClure et al., 2016) and those with full *Herschel* PACS scans, such as the upper limits on HD emission in Herbig disks by Kama et al. (2020b). More observations are necessary to further our understanding of protoplanetary disks. There are future instruments and observatories potentially on the horizon that will observe the frequency range in which HD resides, and with a much higher resolution and sensitivity than *Herschel*. These observatories will have the ability to drastically improve our understanding of early planet formation environments. The HIRMES instrument was proposed to be added to the SOFIA observatory offering a spectral resolution of 3 km s^{-1} at 112 . If built and deployed, HIRMES was projected to have a sensitivity similar to PACS (Richards et al., 2018) and could perform deep surveys for HD emission, opening up the ability to provide a robust diagnostic of gas mass. The planned spectral resolution on HIRMES is enough to fully resolve the HD emission line for inclined disks, which will provide unique constraints on the radial distribution of disk gas. A simulated HIRMES observation of TW Hya based on this model is shown in Figure 2.12.

Looking onward, National Aeronautics and Space Administration's (NASA) *Origins Space Telescope*, if funded and launched, provides a sensitivity improvement at 112 of over three orders of magnitude compared to *Herschel*, enabling deep surveys of over a thousand disks. Origins could provide sensitivities towards the HD line corresponding to gas disk masses down to 10^{-5} $M_{\odot}$(Trapman et al., 2017). These future or potential observatories in combination with future resolved suites of CO lines via ALMA will be incredibly insightful towards out understanding of planet formation enabling the ability to track the 2D temperature structure and the gas mass, thereby revealing the key physical conditions under which planets form.

2.5 Conclusions

Using the thermo-chemical code *RAC2D*, and observations from the TW Hya Rosetta Project taken with ALMA of ^{12}CO J= 2-1, C^{18}O J= 2-1, archival ALMA data of ^{12}CO 3-2, C^{18}O 3-2, 6-5, and ^{13}CO 3-2, 6-5, HD J 1-0, and the system's SED, we find the following:

1. We derive a thermal structure of the TW Hya disk that fits radial brightness profiles of seven spatially resolved CO line transitions, a spatially unresolved HD line flux, and the SED. This study is the first to reproduce multiple spatially resolved observations of CO using a thermo-chemical model. We compare our results to thermal structures derived by other methods.

2. Using the derived thermal structure and the HD (1-0) line flux, we constrain the total gas mass of the TW Hya disk to be $\approx$ 0.025 $M_{\odot}$ within our model framework.

3. We directly demonstrate that CO line brightness distributions are degenerate results of the CO abundance and the total gas mass of the disk. Therefore CO alone cannot be used as a robust tracer of the total gas mass, for any protoplanetary disk system. We find that using observations of HD is one solution that breaks this degeneracy.

CHAPTER 3

Molecules with ALMA at Planet-forming Scales (MAPS) XVII: Determining the 2D Thermal Structure of the HD 163296 Disk

This chapter published in the Astrophysical Journal Supplemental Series (Calahan et al., 2021b) and was completed in collaboration with Edwin Bergin, Ke Zhang, Kamber R. Schwarz, Karin I. Öberg, Viviana V. Guzmán, Catherine Walsh, Yuri Aikawa, Felipe Alarcón, Sean M. Andrews, Jaehan Bae, Jennifer B. Bergner, Alice S. Booth, Arthur D. Bosman, Gianni Cataldi, Ian Czekala, Jane Huang, John D. Ilee, Charles J. Law, Romane Le Gal, Feng Long, Ryan A. Loomis, François Ménard, Hideko Nomura, Chunhua Qi, Richard Teague, Merel L.R. van 't Hoff, David J. Wilner, and Yoshihide Yamato. The paper is reproduced here under the non-exclusive rights of republication granted by the American Astronomical Society to the authors of the paper

Abstract

Understanding the temperature structure of protoplanetary disks is key to interpreting observations, predicting the physical and chemical evolution of the disk, and modeling planet formation processes. In this study, we constrain the two-dimensional thermal structure of the disk around Herbig Ae star HD 163296. Using the thermo-chemical code RAC2D, we derive a thermal structure that reproduces spatially resolved ALMA observations ($\sim$0.12 (13 au) - 0.25 (26 au)) of ^{12}CO J = 2-1, ^{13}CO J = 1-0, 2-1, C^{18}O J = 1-0, 2-1, and C^{17}O J = 1-0, the HD J = 1-0 flux upper limit, the spectral energy distribution (SED), and continuum morphology. The final model incorporates both a radial depletion of CO motivated by a time scale shorter than typical CO gas-phase chemistry (0.01 Myr) and an enhanced temperature near the surface layer of the the inner disk (z/r $\geq$ 0.21). This model agrees with the majority of the empirically derived temperatures and observed emitting surfaces derived from the J = 2-1 CO observations. We find an upper limit for the disk mass of 0.35 M$_{\odot}$, using the upper limit of the HD J = 1-0 and J = 2-1 flux. With our final thermal

structure, we explore the impact that gaps have on the temperature structure constrained by observations of the resolved gaps. Adding a large gap in the gas and small dust additionally increases gas temperature in the gap by only 5-10%.

3.1 Introduction

The two-dimensional (radial + vertical) thermal structure of protoplanetary disks has been a long sought after property due to its importance in interpreting of observations and its importance on disk evolution. Disk temperature sets the physical and chemical evolution of disk material, with subsequent implications for planet formation. The translation of observations into fundamental disk properties, namely gas mass, strongly depends on the assumed underlying disk temperature at which the observed molecule emits. The mass tracer HD (Bergin et al., 2013; McClure et al., 2016; Bergin & Williams, 2017; Trapman et al., 2017; Kama et al., 2020b) especially requires a well defined disk thermal structure as its J=1-0 transition has an E_{up} of 128.5 K. This approaches typical temperatures within the warm molecular layer of protoplanetary disks. The temperature throughout the disk regulates physical evolution by setting local sound speeds (Bergin & Williams, 2017), turbulent viscosity (Shakura & Sunyaev, 1973; Penna et al., 2013), and vertical flaring of the disk (Kenyon & Hartmann, 1987), which can in turn set the angle of incidence of stellar irradiation, further changing the thermal structure. From a chemical perspective, gas temperature controls the rate of gas-phase exothermic reactions. Temperature also dictates the rates of gas-phase deposition and thermal sublimation, effectively prescribing the relative radial chemical composition of ices in the midplane. These sublimation fronts, or snowlines, have been theorized to be favorable sites for planet formation (Hayashi, 1981; Stevenson & Lunine, 1988; Zhang et al., 2015; Schoonenberg & Ormel, 2017), and may affect the chemical composition of a planetary embryo or accreting atmosphere (e.g. C/O Öberg et al., 2011b; Öberg & Bergin, 2016; Cridland et al., 2020)

The most robust attempts to uncover the temperature profile of protoplanetary disks involve a convergence of observations of multiple gas emission lines and thermo-chemical modeling (e.g Kama et al., 2016b; Woitke et al., 2019; Rab et al., 2020; Calahan et al., 2021a). With the advent of the Atacama Large (sub-)Millimeter Array (ALMA), spatially resolved observations of disks became feasible, providing the first empirical measurements of the radial distribution of dust and gas at high-angular resolution. This gave much needed constraints for protoplanetary disk models. The commonly observed ^{12}CO J = 2-1 is optically thick in most gas-rich disks due to it being the second most abundant molecule in the gas phase after H_2. Lower energy transitions and less abundant isotopologues emit from lower vertical layers, resulting in intensity profiles that are affected by temperature and CO surface density/abundance at which that species is emitting. Thus, joint modeling of multiple spatially resolved CO isotopologues provides radial and vertical constraints

Table 3.1. ALMA Observations Summary

Transition	Frequency (GHz)	$E_{\rm up}$ (K)	Beam (×)	PA (°)	rms (mJy beam^{-1})
^{12}CO J=2-1	230.538	16.6	0.14×0.10	-76.3	0.561
^{13}CO J=1-0	110.201	5.3	0.28×0.22	-89.1	0.434
^{13}CO J=2-1	220.399	15.8	0.14×0.11	-76.6	0.541
C^{18}O J=1-0	109.782	5.3	0.28×0.22	-88.8	0.449
C^{18}O J=2-1	219.560	15.8	0.14×0.11	-76.5	0.385
C^{17}O J=1-0	112.359	5.4	0.28×0.21	-89.5	0.528

Note. — These data were taken from values in Oberg et al. (2021) and Czekala et al. (2021), where details regarding the data reduction can also be found.

on the temperature and CO chemistry.

This study determines the 2D temperature structure of the disk around HD 163296, as part of the ALMA-MAPS project, which observed five protoplanetary disks at high resolution. Each disk is detailed in Oberg et al. (2021). HD 163296 is a Herbig Ae star with a stellar mass of 2.0 $M_\odot$(Andrews et al., 2018; Wichittanakom et al., 2020) surrounded by a massive disk (8×10^{-3} - 5.8×10^{-1} $M_\odot$) (Kama et al., 2020b, and references therein) 101 pc away (Gaia Collaboration et al., 2018; Bailer-Jones et al., 2018). Both millimeter continuum and scattered light observations show significant substructure (Grady et al., 2000; Wisniewski et al., 2008; Benisty et al., 2010; Garufi et al., 2014; Monnier et al., 2017; Muro-Arena et al., 2018; Isella et al., 2018; Dent et al., 2019; Rich et al., 2020) including three gaps in millimeter continuum observations at 10, 48, and 86 au. These gaps have been prime targets to test planet formation theories; planets ranging in mass 0.07-4.45 M_J have been theorized to exist within the gaps in HD 163296 (Zhang et al., 2018). The temperature, both of the gas and dust populations in the gaps can be used to directly inform planet formation models. Kinematic studies of HD 163296 suggest the existence of a ~ 2 M_J planet at 260 au (Pinte et al., 2018a, 2020). Further analysis of the velocity structure by Teague et al. (2019a) mapped out the 3D gradient of velocity using ^{12}CO J=2-1 from the DSHARP project (Andrews et al., 2018), and in Teague et al. (2021). Meridional flows are found at the location of the continuum gaps, indicative of ongoing planet formation. The protoplanetary disk around HD 163296 presents an excellent case for determining the 2D thermal profile using some of the highest resolution data available for a disk in which planets are believed to be actively forming.

Two-dimensional temperature structures for HD 163296 have been modeled previously using a combination of spatially unresolved observations of the CO rotational ladder, and other higher energy molecular and atomic transitions (Qi et al., 2011; Rosenfeld et al., 2013; de Gregorio-Monsalvo et al., 2013) with a few studies utilizing thermo-chemical modeling to match numerous observations (Tilling et al., 2012; Fedele et al., 2016; Woitke et al., 2019). These studies found that HD 163296 is a relatively cooler disk compared to other disks surrounding Herbig stars. Resolved observations of ^{12}CO J=2-1 have also revealed insight into the temperature within the disk gaps (Rab et al., 2020).

The observations from the ALMA-MAPS program consists of highly resolved ($\sim$ 0.12 - 0.25), and high S/N observations of ^{12}CO J = 2-1, ^{13}CO J = 2-1, 1-0, C^{18}O J = 2-1, 1-0, and C^{17}O J = 1-0. These observations show structure in the radial intensity profiles (Law et al., 2021c) and CO column density (Zhang et al., 2021a) (hereafter Z21) and allow for a new derivation of the 2D thermal structure.

This paper is organized as follows: We detail our modeling procedure and describe the observations in Section 5.2. In Section 5.3, we present our best fit thermal model and the necessary alterations needed to fit each observed line. In Section 5.4, comparisons of the final model to the empirically derived temperature structure and emitting surfaces are discussed along our derivation of an upper mass limit for the HD 163296 disk and explore CO/H$_2$ degeneracy and temperature effects within the two largest gaps of the HD 163296 disk. We summarize our findings in Section 5.5.

3.2 Methods and Observations

3.2.1 Observations

We use observations of ^{12}CO J=2-1, C^{18}O J=2-1, 1-0, ^{13}CO J=2-1, 1-0, and C^{17}O J=1-0 towards the HD 163296 disk. For this study, we use images which have an average spatial resolution of 26 au for the 1-0 transitions (0.25) and 13 au for the 2-1 (0.12) transitions (Oberg et al. (2021), and Table 3.1). The final image cubes used for this study had a spectral resolution of 200 m s^{-1}, and used a robust = 0.5 weighting. The robust = 0.5 images were used as they provided the highest absolute resolution. These images were "JvM-corrected" (Jorsater & van Moorsel, 1995), which refers to the method of scaling the residuals in the image cube to have identical units as the CLEAN model. This ensures that the final image used for moment zero maps, and subsequent radial profiles, have the correct units (Jy $\mathrm{CLEAN\,beam}^{-1}$); see Czekala et al. (2021) for a detailed explanation. The MAPS program summary, along with data reduction and calibration specifics can be found in Oberg et al. (2021), and the methods of the imaging process are throughly described in Czekala et al. (2021). Radial intensity profiles are created for each CO line for comparison to our model results. Radial profile derivations are presented in Law et al. (2021c). The package BETTERMOMENTS[1] (Teague & Foreman-Mackey, 2018) is used to extract the moment zero map which is then used to calculate the radial intensity profile using GOFISH[2] (Teague, 2019). We follow the same methods in creating our simulated radial intensity profiles.

In addition to ALMA observations of CO, we also compared our model to the *Herschel Space Observatory* observation of HD J= 1-0 and 2-1 towards HD 163296. The HD observations were made using the PACS instrument and were spatially and spectral unresolved. Kama et al. (2020b) used archival data from the DIGIT program (PI N.J. Evans) to determine the upper flux limits for 15 Herbig Ae/Be disks, including HD 163296. They find an upper limit for the flux of the J= 1-0 line of $\leq 0.9 \times 10^{-17}$ $\mathrm{W/m^2}$ and for the J= 2-1 they determine a flux of $\leq 2.4 \times 10^{-17}$ $\mathrm{W/m^2}$.

3.2.2 RAC2D Physical Structure

In this study, we use the time-dependent thermo-chemical code RAC2D[3] (Du & Bergin, 2014) to model the thermal structure of the HD 163296 disk, and create simulated observations to compare to the ALMA data. A brief description of the physical code of RAC2D is given below; a detailed description of the code can be found in the aforementioned paper.

RAC2D takes into account both the disk gas and dust structure while simultaneously computing the temperature and chemical structure over time. Our model consists of three mass components: gas, small dust ($\leq$), and large dust grains ($\leq$ mm). The distribution of each component is described by a global surface density distribution (Lynden-Bell & Pringle, 1974), which is widely used in modeling of protoplanetary disks and corresponds to the self-similar solution of a viscously evolved disk.

$$\Sigma(r) = \Sigma_c \left(\frac{r}{r_c}\right)^{-\gamma} \exp\left[-\left(\frac{r}{r_c}\right)^{2-\gamma}\right], \tag{3.1}$$

r_c is the characteristic radius at which the surface density is Σ_c/e and γ is the power-law index that describes the radial behavior of the surface density.

A density profile for the gas and dust components can be derived from the surface density profile and a scale height:

---

[1] https://github.com/richteague/bettermoments

[2] https://github.com/richteague/gofish

[3] https://github.com/fjdu/rac-2d

$$\rho(r,z) = \frac{\Sigma(r)}{\sqrt{2\pi}h(r)} \exp\left[-\frac{1}{2}\left(\frac{z}{h(r)}\right)^2\right], \tag{3.2}$$

$$h = h_c \left(\frac{r}{r_c}\right)^{\Psi}, \tag{3.3}$$

where h_c is the scale height at the characteristic radius, and Ψ is a power index that characterizes the flaring of the disk structure.

Both dust populations follow an MRN grain distribution $n(a) \propto a^{-3.5}$ (Mathis et al., 1977). The small dust grains have radii between 5×10^{-3} - 1μm, and the large grains have radii between 5×10^{-3} - $10^3\mu$m. The following description of the dust grain population used in this study is adopted from Z21, which used both the HD 163296 SED and mm continuum observations to constrain the dust population. The gas and small dust grains are spatially coupled and extend to 600 au. The large dust population is settled in the midplane with a smaller vertical extent (h = 1.69 au) and radial extent (240 au). This settled large grain population is the result of dust evolution, namely vertical settling to the midplane and radial drift. The large grain population has a unique, non-smooth, surface density profile that reproduces the millimeter continuum observations of the HD 163296 disk (Z21). The dust composition adopted is consistent across the MAPS collaboration, and opacity values are calculated based on Birnstiel et al. (2018). Large dust grains consist of water ice (Warren & Brandt, 2008), silicates (Draine, 2003), troilites and refractory organics (Henning & Stognienko, 1996). Small dust grains consist of 50% silicates and 50% refractory organics.

3.2.3 RAC2D Dust and Gas Temperature

The code computes a dust and gas temperature after initializing RAC2D with a model density structure for each population, a stellar spectrum, and external UV radiation field (G_0=1). The stellar spectrum we use is a composite of multiple UV and X-ray observations, and is further detailed in Z21. The determination of dust and gas temperature is an iterative process, allowed to change over time due to the evolving chemical composition. The dust thermal structure is calculated first using a Monte Carlo method to simulate photo absorption and scattering events. This also results in a radiation field spanning cm to X-ray wavelengths.

We adopt the reaction rates from the UMIST 2006 database (Woodall et al., 2007) for the gas-phase chemistry with additional rates considering the self-shielding of CO, H_2, H_2O, and OH, dust grain surface chemistry driven by temperature, UV, cosmic rays, and two-body chemical reactions on dust grain surfaces (see references given by Du & Bergin, 2014). Chemical processes also provide heating or cooling to the surrounding gas. These mechanisms along with stellar and interstellar radiation drive the thermal gas structure. Our study explores models that account for 0.01 Myr of chemical evolution. This is a relatively short period of time compared to disk lifetimes and is motivated by an average CO processing timescale, which is found to be on the order of 1 Myr (Bergin et al., 2014; Bosman et al., 2018b; Schwarz et al., 2018). The calculated depletion profile of CO is motivated by observations, and thus accounts for any long time-scale chemical effects that have taken place in the disk's history; we did not want to further process CO by running the disk model for longer than 0.01 Myr. It is also worth noting that the exact time scale will not affect our final temperature structure nor CO column density distribution; it will only affect the CO depletion profile. CO will be created or destroyed in our chemical network over time, and the CO depletion profile acts to counter any over or under-abundance of CO being produced. While localized variations in the CO abundance may affect the gas temperature, the global temperature structure is not strongly affected by the CO abundance.Finally, at the end of a given run, we extracted the dust and gas thermal profiles.

Simulated line images for CO, ^{13}CO, C^{18}O, C^{17}O and HD are necessary for our comparison to observations. We did not model isotopologue fractionation in this chemical network, as fractionation of CO is not significant in a massive disk like HD 163296 (Miotello et al., 2014). Thus, we computed ^{13}CO and C^{18}O abundances based on ISM ratios of ^{12}CO/^{13}CO = 69, ^{12}CO/C^{18}O = 557, C^{18}O/C^{17}O = 3.6 (Wilson, 1999). Given these abundances and the local gas temperature, RAC2D computes synthetic channel maps using a ray-tracing technique. We then convolved these simulated observations with the corresponding ALMA CLEAN beam to make direct comparisons to data. To directly compare to observations, we created simulated integrated radial intensity profiles of each of the CO lines, following the methods from Law et al. (2021c). Our simulated observations have the same beam sizes, spectral resolution, and pixel size as what is reported in Oberg et al. (2021). To recreate the unresolved integrated flux measurements for HD, we convolved our model HD lines with a Gaussian profile corresponding to the velocity resolution of the *Herschel* PACS instrument: $\sim$300 $\mathrm{km\,s^{-1}}$ at $\sim$112 μm and $\sim$100 $\mathrm{km\,s^{-1}}$ at $\sim$51 μm (Poglitsch et al., 2010)

We began with a model of the HD 163296 disk from Z21, which starts with an initial set of disk parameters taken from the literature (see references within Zhang et al., 2021a) and applied the observed UV, X-ray and photosphere stellar spectra. These authors then determined a gas and dust density and dust temperature structure by matching the SED and ALMA continuum image using RADMC3D (Dullemond et al., 2012b). Given this initial density and dust temperature distribution, RAC2D is then used to compute the gas temperature and disk chemistry. Z21 found that in order for the simulated radial profiles to match what is observed, they must modify the CO abundance relative to H_2 as a function of radius. They use the difference between C^{18}O J=2-1 as observed and as simulated to predict a CO depletion profile. That depletion profile is shown in Figure 3.1. The initial chemical abundances used in Z21 are shown in Table 3.2 and final model parameters are

Table 3.2. Initial Chemical Abundances for Final Model

	Abundance Relative to Total Hydrogen Nuclei
H_2	5×10^{-1}
HD	2×10^{-5}
He	0.09
CO[a]	see Figure 3.1
N	7.5×10^{-5}
H_2O (ice)	1.8×10^{-4}
S	8×10^{-8}
Si^+	8×10^{-9}
Na^+	2×10^{-8}
Mg^+	7×10^{-9}
Fe^+	3×10^{-9}
P	3×10^{-9}
F	2×10^{-8}
Cl	4×10^{-9}

Note. — [a]CO starts with an abundance of 1.4×10^{-4} with an imposed radial depletion profile as shown in Figure 3.1

Table 3.3. Gas and Dust Population Parameters: Best-fit Model Values

	Gas	Small Dust	Large Dust
Mass ($M_\odot$)	0.14	2.6×10^{-4}	2.4×10^{-3}
Ψ	1.08	1.08	1.08
γ	0.8	0.8	0.1
h_c [au]	14.5	14.5	–
r_c [au]	165	165	–
r_{in} [au]	0.45	0.45	0.45
r_{out} [au]	600	600	240

Note. — Final values of the HD 163296 model that reproduces the CO, HD, and SED observations. Small dust grain sizes range from 5×10^{-3} - 1, large dust grain sizes range from 5×10^{-3} - 1×10^{3}. The large dust population does not have associated h_c nor r_c because the surface density is set by continuum observations, thus is non-smooth and not dictated by Equation 4.1-4.3

summarized in Table 3.3. In the study described here, we use the Z21 model as a starting point to derive a 2D temperature map incorporating additional constraints from CO isotopologues, multiple higher-level CO transitions and HD flux. We note that while any revisions made were important to constrain the disk temperature structure, they do not affect the results reported in Z21, and the final CO column densities from this model agree well with what is found in Z21.

3.3 Results

3.3.1 CO depletion

In Z21, depletion of CO was calculated based on a model of the disk based on previous determinations of disk parameters and the $C^{18}O$ J = 2-1 radial intensity profile. The CO was depleted throughout the disk at the start of the raytracing method which creates the simulated observations, i.e. after the temperature and chemical evolution of the disk. This depletion means the CO abundance is reduced from its expected value ($\sim 10^{-4}$ relative to H_2) in layers where the dust temperature is above the CO sublimation point and the gas is self-shielded from radiation. Since CO

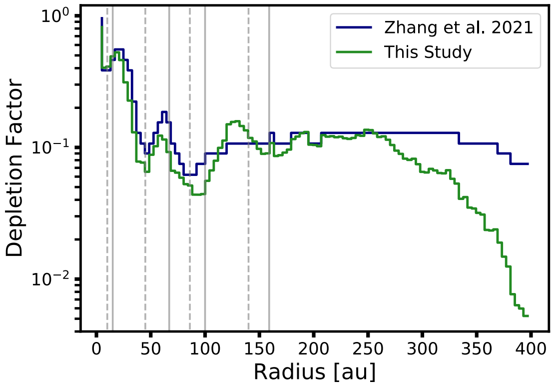

Figure 3.1 *Multiplicative depletion factor for the initial CO abundance (CO/H=*1.4×10^{-4}*) as shown in Table 3.2. Light gray lines indicate the location of the dust rings (solid) and gaps (dashed). The line in blue shows the CO depletion as derived by Z21 and is determined after an initial thermo-chemical model of the HD 163296 disk and is based on the* $C^{18}O$ *J=2-1 observation, and acts as a starting point for our CO depletion determination. The green represents the final CO depletion, also motivated by the* $C^{18}O$ *J=2-1 flux but is taken into account at the beginning of the chemical and thermal calculations.*

is a significant coolant in the disk surface layers where the dust and gas are thermally decoupled, any depletion of CO may affect the thermal structure. Thus, for this study, we recalculated the CO depletion factors. We started by applying the Z21 CO depletion to the initial CO abundance. After running the model for 0.01 Myr, there were small inconsistencies between the simulated and observed $C^{18}O$ J=2-1 radial emission profiles (see Figure B.1). We then calculated a new CO depletion profile by determining what factor of increase or decrease in CO flux would be needed to reproduce the observation at each radii (using the same radial resolution as Z21). That factor was the applied to the original CO depletion profile at the corresponding radius. The model was then run again with the new CO depletion profile. We needed to iterate this process three times, and stopped iterating once the χ^2 value (using `stat.chisquare` function from the `scipy` package) comparing the simulated and observed $C^{18}O$ J=2-1 radial profile intensity values had dropped well below that of the first attempts. The first three attempts had χ^2 value of 8.06-9.72, and the final model χ^2 = 2.47. The final depletion profile is shown in Figure 3.1, and on average the newly calculated CO depletion is 33% more depleted than that derived in Z21. Most of the difference is at large radii where the profiles vary by only 16% within 200 au.

There is a strong decrease in CO abundance beyond ∼250 au, which is not seen in the CO depletion profile calculated by Z21. The CO depletion profile from Z21 accounts for an initial CO depletion in HD 163296 plus 1 Myr of CO processing accounted for in the RAC2D chemical evolution. In our model, we include only 0.01 Myr of additional chemical processing, thus we do

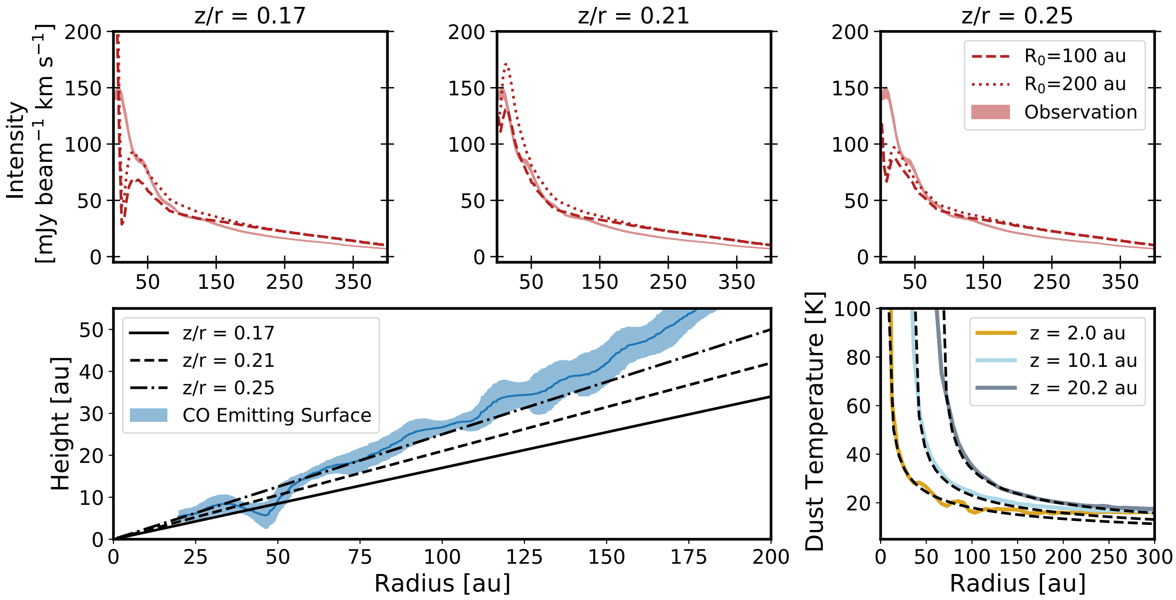

Figure 3.2 *These figures represent the effect of excess heating on the* ^{12}*CO J=2-1 line profile given different height over radius (z/r) limits (0.17, 0.21, 0.25, columns) and R values (100 and 200 au, dashed line and dotted line) using* $(r/R_0)^{-0.4}$ *to calculate the excess factor of heat in the regions above a certain z/r. We sought to find a z/r and* R_0 *value that would reproduce the observed* ^{12}*CO J = 2-1 radial profile (solid red lines). The above is just a sample of the z/r and* R_0 *values explored, with our final model using z/r limit of 0.21 and* R_0 *= 100 au. The bottom left plot shows the observed emitting surface of* ^{12}*CO J = 2-1 (blue) and the z/r values explored. The bottom right plot shows the dust temperature over radius at different heights in the disk, which follow an inverse power-law function, and each dashed black line is a power-law following* $r^{-0.4}$*, which is what we use to determine the excess heat factor.*

not attempt to model the full evolution of CO. In the Z21 model, their derived CO depletion profile takes into account chemical processing that occurs over the course of 1 Myr. The difference in CO abundance for our HD 163296 disk model as compared to the Zhang model is then attributed to chemical CO depletion mechanisms that occur over 1 Myr. In the Zhang model, fully self-shielded CO becomes frozen out and interacts with OH frozen out onto grains and creates CO_2. In our model, we treat past CO chemistry as an initial condition. We find it necessary to additionally deplete CO beyond $\sim$240 au in the model that runs for only 0.01 Myr, since the pathway to convert CO and CO_2 is unavailable within that time.

3.3.2 Additional Heating

While our initial model with the updated CO depletion profile reproduced most of the observed CO lines, ^{12}CO J=2-1 was under-predicted on average by a factor of 1.6 within 100 au, and a factor of 2.2 within 35 au. We completed a thorough exploration of the parameter space including gas mass, small dust mass, surface density power-law index (γ), flaring index (Ψ), scale height (h_c), critical radius (r_c), and outer radius (see Appendix Section B.1). However, we found no combination of parameters that could improve the ^{12}CO J=2-1 flux agreement while leaving the other lines consistent with observations. This result together with the high optical depth of the ^{12}CO J = 2-1 transition suggests that the discrepancy is due to a higher temperature in the CO emitting layer. This has also been seen in de Gregorio-Monsalvo et al. (2013); ^{12}CO J = 3-2 was observed to be brighter than their model which matches the outer disk. To solve this issue they increased the gas temperature beyond the dust temperature within 80 au in their HD 163296 disk model.

This higher gas temperature requires additional heating, beyond the level generated by the UV and X-ray field in our model. We began by isolating the layers in which the gas and dust thermal structure are decoupled. Within those regions, with the goal of representing excess heating due to radiation from the star, we artificially increased the gas temperature after the thermo-chemical calculation, and simulated new CO observations. We increased the temperature in this region following a power-law dependent on radius, and by a constant amount vertically (see equation below). There was no realistic amount of heating within the decoupled layer that would increase the intensity of the ^{12}CO J=2-1 line to match what is observed, any excess heating only affected emission from the inner few au. This then suggests that the ^{12}CO J=2-1 primarily emits from the region lower in the disk, in which the dust and gas temperatures are coupled, and the necessary excess heating would decouple the gas and dust temperatures.

We increase the gas temperature radially following the dust thermal profile. Increasing the gas temperature as function of radius following a power-law,

$$T_{\mathrm{new}} = T_{\mathrm{original}} \times (\frac{\mathrm{r}}{100\mathrm{au}})^{-0.4}$$

above a constant ratio of height over radius (z/r) = 0.21 reproduces the observed ^{12}CO J=2-1 radial profile. Outside of this region, the gas and dust temperatures remain coupled. Various z/r limits were explored, and z/r = 0.21 produced a result that appeared to significantly affect the ^{12}CO J=2-1 line while not altering any other lines (see Figure 3.2 for a sample of the parameter exploration results). It can then be presumed that the emitting surface of ^{12}CO J=2-1 exists at or above z/r=0.21 within 100 au, and all other lines emit from below these heights (this is supported by further analysis probing the emitting surfaces of each 2-1 transition, see Section 3.4.1, and Law et al. (2021a)). Higher transitions of CO, up to ^{12}CO J = 23-22 have been observed using the SPIRE instrument on *Herschel* and are compiled in Fedele et al. (2016). These transitions will primarily emit from the very inner regions of the disk, and would be affected by the increase in temperature. Our final model reproduces all of the observed fluxes of the 19 higher-level transitions of CO, most within 1σ uncertainly, and five of the transitions fit within 2 or 3σ uncertainty (see Table B.2). While the flux predictions from the model all fall within 3σ, all are on the fainter end of the observed flux. Additionally, the HD J=2-1 flux does not change significantly, increasing only by 7%, remaining well below the observed upper limit. A model without the additional heat produces a CO flux from the J=11-10 transition that is over two times less than our final model. On average, for the transitions between J=11-10 and J=23-22, a model without the additional heat produces a CO flux over four times lower than our current model.

The majority of the excess heat is added within 25 au where gas temperatures are beyond twice the original output from our thermo-chemical model. A likely source of this excess heat is mechanical heating from processes such as stellar winds or dissipation of gravitational energy from accretion through the disk onto the star (e.g. Glassgold et al., 2004; Najita & Ádámkovics, 2017). Mechanical heating from such phenomena is expected to be prominent in the inner disk ($<$ 10 au), and are not accounted for in RAC2D. Another possible heating source originates from PAHs, as photoelectric heating of small grains (Draine & Li, 2001; Li & Draine, 2001) is one of the main heating mechanisms in this region after direct UV heating from the star. The PAH abundance might be enhanced in the inner disk if dust sintering is taken into account (Okuzumi et al., 2016). As dust grains pass the sublimation front of their constituent material, PAHs can be released, enhancing the effect of photoelectric heating near which ^{12}CO 2-1 emits. PAH emission towards HD 163296 has been observed as a part of the *ISO*/SWS atlas (Sloan et al., 2003) and modeled by Seok & Li (2017). Their best fit model uses a PAH abundance of 8×10^{-7} M, which is 1.5× the abundance used in our RAC2D model. In our model and assumed physical set-up, the excess heat is necessary in a region where the gas and dust are thermally coupled. Any increase in PAH abundance in our model will not change the temperature at which the majority of ^{12}CO J=2-1

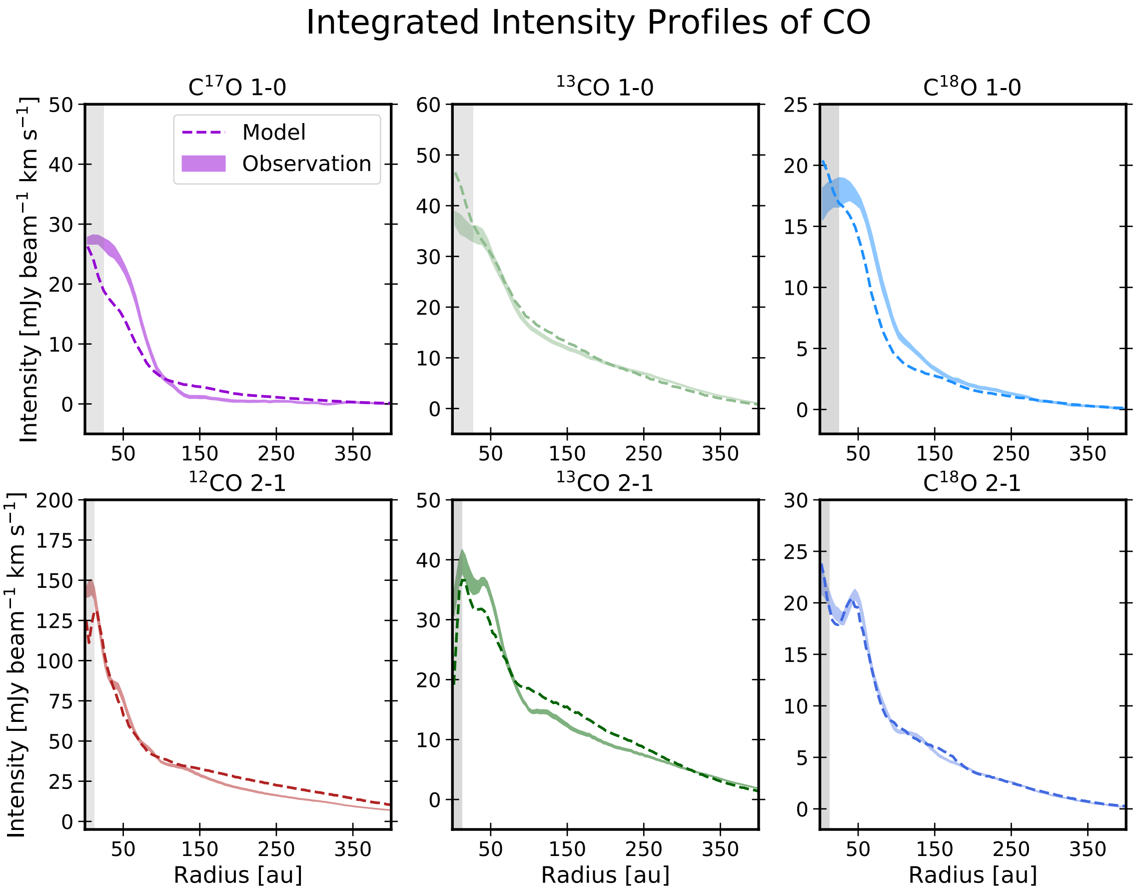

Figure 3.3 *Integrated radial intensity profiles of* ^{12}*CO and its isotopologues* ^{13}*CO, C*^{18}*O, and C*^{17}*O as observed (solid line) and as simulated by the thermo-chemcial code RAC2D (dashed line). The gray shaded regions correspond to the FWHM of the corresponding beam for each observed line. This presents our best-fit model to the observations of the HD 163296 disk and represents the thermal structure shown in Figure 3.4.*

emits. It only affects the temperature in thermally-decoupled layers where dust densities are low and gas and dust collisions do not occur often. However, it remains a possibility given an alternate setup of HD 163296 in which ^{12}CO J=2-1 emits in the thermally decoupled layers.

3.3.3 Final Model

The model that best reproduces the CO radial profiles observed towards HD 163296 was achieved by altering the CO depletion profile derived by Z21, and increasing the gas temperature above a z/r = 0.21 within the inner 100 au of the disk. The CO radial profiles derived from the final model are shown in Figure 3.3 together with the observed profiles. The final gas and dust thermal structures

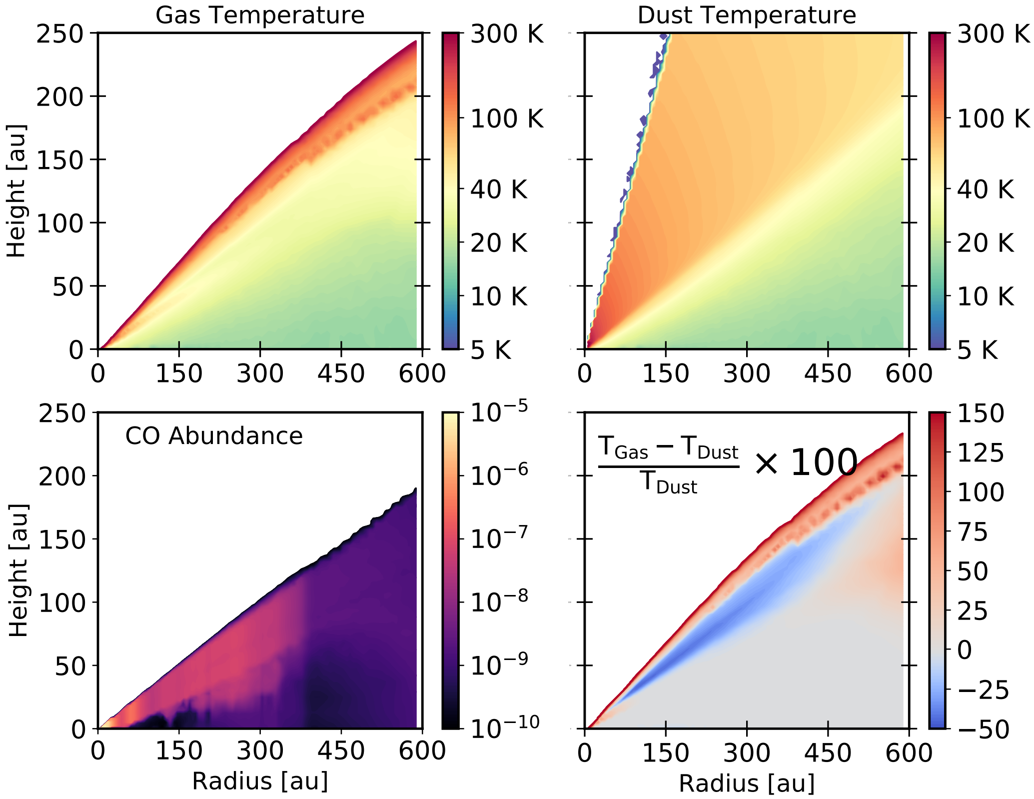

Figure 3.4 *The two-dimensional profile of gas temperature, dust temperature, percentage difference between the two, and CO abundance. The dashed black or white line in each plots shows where z/r=0.21 which corresponds with the* ^{12}*CO J = 2-1 surface within 100 au. This represents the model that best-represents the observed radial profile, SED, and an HD flux that agrees with the currently derived upper limit. In the percentage difference plot, one can see where the dust and gas temperatures are coupled (grey), the 'undershoot' region (Kamp & Dullemond, 2004), where dust is warmer than the gas (blue), and where gas is warmer high up in the atmosphere (red).*

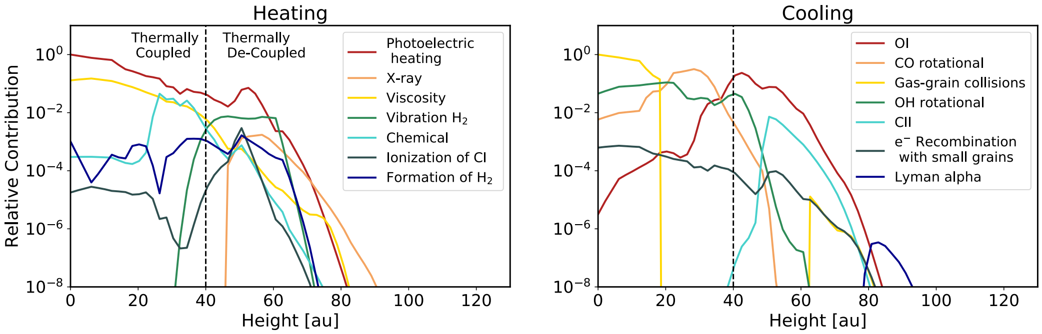

Figure 3.5 *The seven most significant heating (right) and cooling (left) mechanisms in our final model at a disk radius of 150 au, as a function of disk height, normalized according to the highest heating/cooling value at this radius. The black dashed line corresponds to the height (40 au) at which the dust and gas temperatures become decoupled.*

are shown in Figure 3.4. Comparing the gas and dust temperatures, we find that below a z/r $\simeq$ 0.25 the dust and gas are thermally coupled (with the exception of the increased gas temperature added artificially). Right above z/r $\simeq$ 0.25 the dust is hotter than the gas by factors of 25%-50%. This region has been referred to as the 'undershoot' region (Kamp & Dullemond, 2004) and occurs in disks where the gas density increases sufficiently for line cooling to become very efficient, and occurs around the $\tau = 1$ surface. In our model, atomic oxygen dominates cooling in this region, and cooling via gas-grain collisions are particularly inefficient (see Figure 3.5). At the very surface of the disk, the gas temperature then increases drastically, overtaking the dust temperature significantly, which tends to plateau above the undershoot region. Directly above the undershoot region, photoelectric heating and the vibrational transitions of H_2 are the most significant heating processes, with direct heating of the gas via X-ray radiation overtaking beyond z/r $\simeq$ 0.45-0.5. This gas/dust temperature decoupling has been predicted (Kamp & Dullemond, 2004; D'Alessio et al., 2005) and seen in models before (Tilling et al., 2012; Woitke et al., 2019; Rab et al., 2020).

It is worth noting that the $C^{17}O$ and $C^{18}O$ 1-0 lines are the least well fit to the observations. We also find that these transitions originate from deep within the disk, only slightly above the midplane, and CO snowsurface. In Z21 it was noted that the $C^{17}O$ column densities appear to be higher than those estimated from $C^{18}O$ (correcting for optical depth). This is also the case for an earlier $^{13}C^{18}O$ detection, which appears to require higher CO column than inferred from $C^{18}O$ J = 2-1 (Z21). A similar analysis is preformed for the MAPS data in Z21. It is suggested that the CO abundance might be higher in the midplane as the icy pebbles drift inwards and sublimate CO inside the snowline. Booth et al. (2019) estimates a disk mass of 0.21 $M_\odot$ using $^{13}C^{17}O$ J=3-2, a value 50% more massive than our final model. However, if CO is enhanced near the midplane, a larger mass may not be necessary. Such an effect is not accounted for in our analysis, but, at face value, would be consistent with our results in that a locally higher abundance of CO in the midplane, perhaps inside the CO snowline, would increase the emission of optically thin tracers (such as $C^{17}O$) while having a reduced effect on the emission of the more abundant isotopologues. This process has negligible effect on the thermal structure as the dust and gas are strongly coupled in these layers.

3.3.3.1 CO and CO_2 Snowline

To determine the location of the CO snowline in our model, we determine the radial location at which there are equal parts CO frozen onto the dust and in the gas phase. RAC2D includes adsorption of CO (and other species) onto dust grains as well as desorption from the dust surface either thermally, or via UV photons or cosmic rays (see Du & Bergin, 2014). Using this metric, our CO snowline is located at 60 au at a temperature of 18 K. This falls between the largest gaps in the continuum, and is consistent with Z21. Qi et al. (2015) used observations of N_2H^+ towards HD 163296 to determine the CO snowline as N_2H^+ formation is inhibited in the presence of gas-phase CO. When CO is frozen-out N_2H^+ can exist, emitting as a ring with the inner most edge corresponding to the CO snowline. Using this method, and a model of the HD 163296 disk, they found a CO snowline at 74^{+7}_{-5} au (corrected for pre-Gaia distance). Our midplane snowline location is in good agreement with the N_2H^+ derived snowline location, especially when considering findings from van 't Hoff et al. (2017) that show the N_2H^+ column density peaks 5 au or more beyond the midplane CO snowline. Additionally we can predict the CO_2 snowline to be at 4 au, at a temperature of 65 K. These freeze-out temperatures depend on the given desorption energy. RAC2D uses values from Garrod et al. (2008) which assumed an amorphous ice surface. Assuming a different desorption energy will alter the derived snowline locations. It is important to note also, that these snowlines are based on a thermo-chemical model influenced by observations that do not directly probe the midplane.

3.4 Discussion & Analysis

3.4.1 Emitting Surface

An additional observational constraint on our model is the resolved emission heights of ^{12}CO, ^{13}CO, and $C^{18}O$ J = 2-1 as measured in Law et al. (2021a). We calculate the emitting surfaces of ^{12}CO, ^{13}CO, and $C^{18}O$ using simulated image cubes and the same methods as applied to the observations by Law et al. (2021a). This method depends on the ability to resolve the front and back side of a given disk over multiple channels of an image cube, and assumes azimuthal symmetry and gas rotating in circular orbits (Pinte et al., 2018a). The emitting height extraction tools are

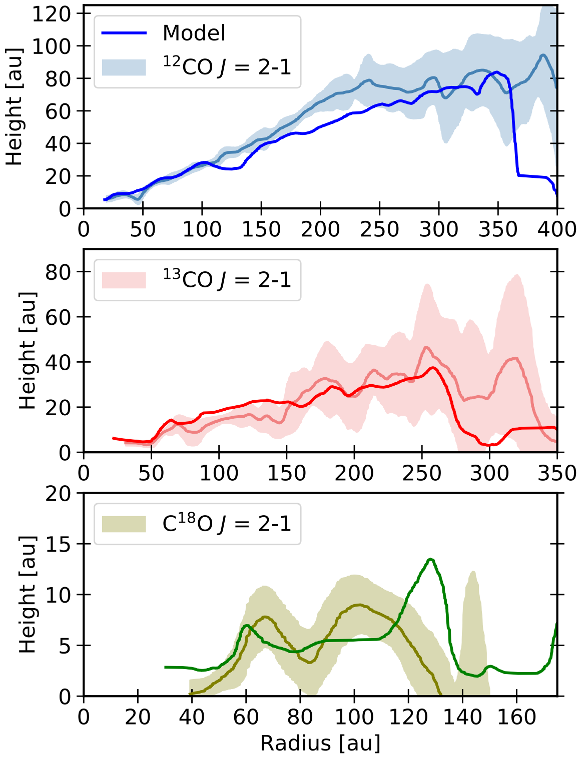

Figure 3.6 *Derived emitting surfaces and calculated uncertainties of the 2-1 transitions of ^{12}CO, ^{13}CO , and C^{18}O. Observed emitting surfaces with calculated error is shown in blue, red, and green from Law et al. (2021a) while the model emitting surfaces are in the brighter blue, red, and green without accompanied error.*

found in the Python package `disksurf`[4]. A comparison of the emitting layers of our model and observations are shown in Figure 3.6.

The calculated emitting layers for both simulated and observed data from Law et al. (2021a) exist at similar heights, and agree within 1σ at most radii. No additional changes to the model were necessary to arrive at this agreement between model and observation. Our modeled emission height for ^{12}CO J=2-1 reproduces what was derived using the ALMA observations up until ∼125 au; beyond this radius and up to 250 au, the model's ^{12}CO emits on average 11 au lower in the disk. Looking at ^{13}CO emitting height, beyond ∼125 au the model reproduces the observed heights. This suggests that our model does not completely represent the CO vertical distribution, as it systematically produces a lower ^{12}CO J=2-1 emission height beyond ∼100au. However, this fit is quite good considering the detailed physics and chemistry included in the model. The C^{18}O emitting heights agree well with what is observed, especially within ∼100 au, where both our model and the observations pick up on some substructure, a bump at 70 au and subsequent dip at 85 au. Our model shows another increase in the C^{18}O emission height at 110 au, not present in

---

[4] https://github.com/richteague/disksurf

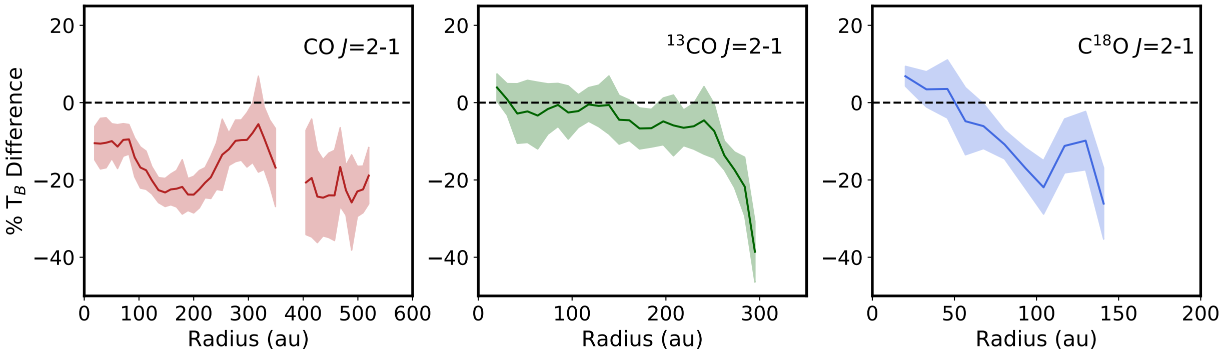

Figure 3.7 *A comparison of the derived brightness temperature from the HD 163296 disk model and ALMA observations (Law et al., 2021a). The y-axis shows the percentage difference between derived brightness temperature from the model and the ALMA results (*$\frac{T_{\rm rac2d}-T_{\rm obs}}{T_{\rm obs}} \times 100$*). The error is plotted as the shaded region and is motivated by the 1*σ *uncertainty in the observed brightness temperature (*$\frac{T_{\rm rac2d}-T_{\rm obs}\pm\Delta T_{obs}}{T_{\rm obs}} \times 100$*).*

the ALMA observations, a feature created due to relative CO abundance based on our depletion profile (see Figure 3.1).

3.4.2 Comparison to Empirical Temperature Structure

In Law et al. (2021a), radial brightness temperatures ($T_{\rm B}$) are calculated for each of the CO J= 2-1 isotopologue lines, with a resolution of a quarter of the beam size. Here, we derive the brightness temperature of our model using an identical procedure to enable a consistent comparison. We compare the empirically derived temperatures for each of the J= 2-1 lines in Figure 3.7. At most radii, the model's derived brightness temperature agrees within 10% of the observed brightness temperature. Regions where the brightness model temperature is less than ∼20% of the observed $T_{\rm B}$ corresponds to regions where the emitting heights diverge. For example, in the ^{12}CO comparison, the brightness temperature derived from the model is 20% less than the observed value starting at $\sim$ 125 au, precisely where the ^{12}CO emitting heights diverge and the model ^{12}CO emitting height is 11 au deeper in the disk, where temperatures are cooler. Brightness temperatures measured from ^{13}CO are in good agreement, up until ∼250 au. Beyond ∼250 au the model's emitting height sharply decreases while the observed emitting heights stay relatively constant (although with large uncertainty), which explains the large disconnect between the model and observed brightness temperatures. The average brightness temperature derived from ALMA observations of C^{18}O is 24 K, thus at radii where the model differs from the observed brightness temperature the most (∼20% less than observed), it is by just 4-5 K. Based on these comparisons, we show that this temperature structure based on a model derived by matching radial intensity profiles of CO, the disk SED, and unresolved fluxes of HD and upper transitions of CO, reproduces the observed brightness temperatures relatively well.

3.4.3 Implications for Disk Mass

This model uses a disk mass of 0.14 $M_\odot$. However, there is a degeneracy between the CO and H_2 surface densities. Increasing one parameter while decreasing the other by the same factor produces a model that reproduces nearly identical radial profiles in CO as the original model (Calahan et al., 2021a). Any change in heating based on the H_2 or CO mass (heating via H_2 formation, H_2 and CO self-shielding) will not significantly affect the regions where the dust and gas temperatures are coupled. This applies to the vast majority of the disk, and where the bulk of the HD flux originates. Observing the flux of the molecule HD is a way to break this degeneracy and directly probe mass, as its ratio to H_2 is well understood (Linsky, 1998). Unfortunately, there was a non-detection of HD towards HD 163296 when observed with the PACS instrument on *Herschel* (Poglitsch et al., 2010; Pilbratt et al., 2010). Kama et al. (2020b) provides 3σ line flux upper limits for the HD 1-0 and 2-1 lines, 6.0×10^{-18} W/m^2 and 3.0×10^{-18} W/m^2 respectively. Our model predicts an HD 1-0 flux of 3.3×10^{-18} W/m^2 and a 2-1 flux of 8.26 $\times 10^{-19}$ W/m^2. While it remains below the flux upper limit, this results in considerable uncertainty in the mass.

To determine an upper mass limit, we use our final model and increase the disk gas mass while decreasing the CO abundance by the same factor. Due to the degeneracy between H_2 and CO, we can continue to reproduce the observed CO radial profiles while increasing the mass of the disk. An HD 163296 disk model with a mass of 0.35 $M_\odot$ produces a predicted HD 1-0 flux of 5.9 $\times 10^{-18}$ W/m^2 and 2-1 flux of 2.0 $\times 10^{-18}$ W/m^2. This is our upper mass limit, as constrained by the HD flux. This upper mass limit is higher than the majority of mass estimates for HD 163296, and lower than the largest estimate for HD 163296 which is 0.58 $M_\odot$ from Woitke et al. (2019). A more recent estimation for HD 163296 is presented in Booth et al. (2019) using the optically thin CO isotopologue, $^{13}C^{17}O$, and predict a mass of 0.21 $M_\odot$. This is a higher mass than we use in our model, but is also consistent with the HD flux limits and our thermo-chemical model. Using their derived HD flux limits, Kama et al. (2020b) determined an mass limit for the disk of $\leq$ 0.067 $M_\odot$. They created a disk model that reproduced dust observations and a number of unresolved rotational transitions of ^{12}CO as well as a resolved observation of ^{12}CO J = 3-2. There are two significant differences between our physical models that could explain the disparity between our calculated upper mass limits. Their HD 163296 model uses a star with a luminosity of 31 $L_\odot$ (Folsom et al., 2012) while this model uses a much lower luminosity of 17 $L_\odot$ (Fairlamb et al., 2015). Additionally, they do not deplete CO which acts as a gas coolant, namely in the

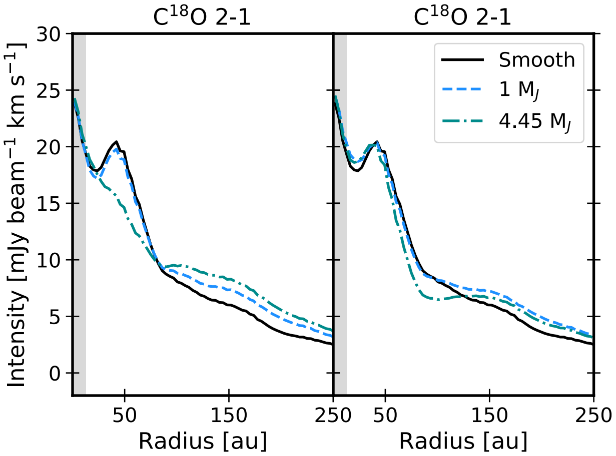

Figure 3.8 *$C^{18}O$ J = 2-1 radial profiles for a smooth model (black), a model with a gap in the small dust and gas population that corresponds to a 1 M_J planet (blue dashed), and 4.45 M_J planet (teal dashed). The left plot shows the results for a gap centered at 48 au, and the right a gap at 86 au.*

decoupled thermal regions, leading to a slightly cooler disk than ours. The contrast between our two models using the same HD flux observation to derive different disk mass estimates highlights the importance of a well-defined temperature structure.

3.4.4 Implications for Gap Thermo-Chemistry

The temperature of gas in potentially planet-carved gaps can provide insight into planet formation models directly linking protoplanetary disk environments to planet formation theories. The effects of disk geometry on temperature have been studied previously and it has been shown that the properties of local perturbations in the disk, including gap size and depth, radial location from the star, and disk inclination, will have an effect on the temperature structure (Jang-Condell, 2008). Gaps have been found to be either cooler or warmer than the surrounding medium, dependent on disk geometry and other model assumptions. A decrease in the gas and small dust surface density exposes material in and near the midplane to more UV flux, allowing for an increase in the temperature of both the gas and dust (van der Marel et al., 2018; Alarcón et al., 2020), however puffed up walls can produce shadows cooling the disk midplane (Nealon et al., 2019) or the gas-to-dust ratio can be low enough to decouple gas and dust temperatures heating only the dust (Facchini et al., 2018). Using our final model, we explored the effect that corresponding gaps in the gas and small dust in HD 163296 may have on the presumed CO depletion, and subsequent gap temperature effects.

The gaps observed in the continuum emission in the HD 163296 disk are accounted for in the surface density of the large grains in our model. Meanwhile, the gas and small dust surface

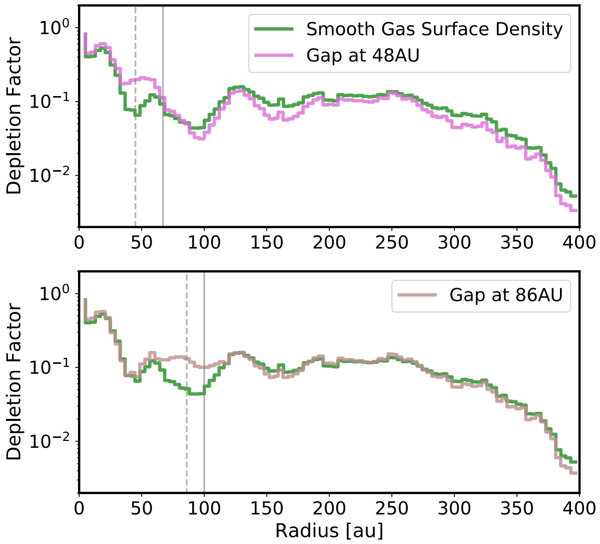

Figure 3.9 *The calculated CO depletion for a smooth surface density model (green), and for a models with a gap at 48 au (top, pink) and 86 au (bottom, dark pink). The dashed grey lines correspond to the center of a gap, and the solid grey link corresponds to a ring. When imposing a gap in the total surface density, the CO depletion is flat or enhanced as opposed to being a local minimum at the location of the gap.*

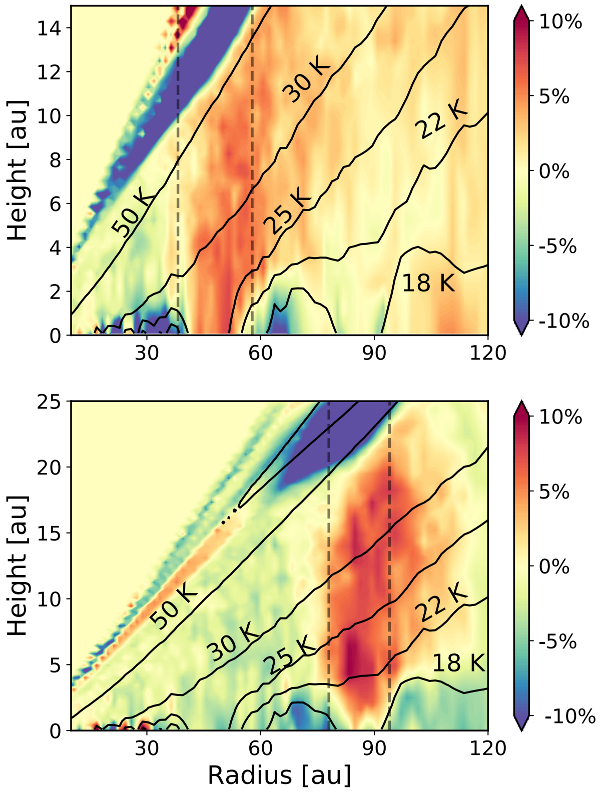

Figure 3.10 *A comparison of gas temperatures between a model with a smooth gas surface density, and a model that has a gap in the gas at 48 au or 86 au. Both models have gaps in the large dust population and both models match observed radial profiles of CO, and follow a CO depletion profiles seen in Figure 3.9. Contour lines show gas temperatures of the smooth gas surface density model. The background corresponds to percentage difference from the smooth surface density model. Positive values imply a hotter temperature in the gas gap models, negative values indicate hotter temperature in the smooth model. The dashed black lines correspond to the gap width.*

densities are smooth, and do not account for these gaps. This is a deliberate decision, as a primary goal of this study is to constrain the global thermal properties of the gas disk in general. We find that even with a smooth H_2 gas distribution, the location of the gaps in the large dust population are warmer than outside of the gap by on order of a few Kelvin. This is supported by previous studies of the HD 163296 disk (van der Marel et al., 2018; Rab et al., 2020) which also find an increased temperature at gap locations using thermo-chemical models and observations of the gas and dust.

Gaps are often attributed to on-going planet formation. To determine the gas and small dust depletion level within the gap, we created four models representing two of the gaps and two possible planet masses. The most prevalent gaps in the continuum (the widest, and highest contrast gaps) are located at 48 au and 86 au. The location, depth, and width of the gas and small dust gap used in our model is motivated by the measured gap widths in continuum from Isella et al. (2018) and the predicted planet masses from Zhang et al. (2018) dependent on dust size distribution and viscosity. We set gap depths, parameterized by a depletion of H_2 gas within the gap, using two assumed planet masses, 1 M_J, which represents a typical planet mass estimate for the HD 163296 disk (Pinte et al., 2018b; Teague et al., 2021), and 4.45 M_J, which represents the highest mass planet predicted within HD 163296 (Zhang et al., 2018). We used Equation 5 in Kanagawa et al. (2015) to determine gap depth using our model's density distribution, viscosity ($\alpha = 10^{-2}$), and planet mass. A 1 M_J planet at 48 au leads to a gas depletion depth of 23%, and at 86 au, 19%. A 4.45 M_J planet at 48 au leads to a gas depletion depth of 85%, and at 86 au, 82%.

We use our final HD 163296 disk model and re-run it with the new gas surface density dependent on gap location and planet mass. The two models with a gap from a 1 M_J planet produces a negligible change in the observed radial intensity profile while a model with gap depths corresponding to 4.45 M_J planet shows a significant decrease in flux, see Figure 3.8. We then calculate a new CO depletion profile in order for the models with a 4.45 M_J planet induced gap to match the observed radial emission profile. Those profiles are show in Figure 3.9. Previously, with a smooth gas distribution, the CO depletion profile had local minima at the location of the gaps. In the case of a gas and small dust surface density with deep gaps, the CO abundance increases at the location of the gaps bringing it to a level on par with the depletion factors just outside of the gaps. Our method of CO depletion makes it difficult to disentangle chemical/gap effects on the CO abundance, so it is impossible to decern if this relative increase in CO in the gaps is an enhancement or a leveling off to a more constant CO depletion across radius. Studies such as Alarcón et al. (2020) and van der Marel et al. (2016) have predicted that CO enhancement in the gaps is needed to match observations. One possible mechanism to enhance the CO abundance is the presence of meridional flows found at the gaps in HD 163296 by Teague et al. (2019a), which can transport gas and small grains from upper atmosphere, bringing CO sublimating from grains and a rich chemistry to an otherwise chemically inert midplane. Whether or not CO is enhanced locally, is dependent on the depth of the gas gap. At present, the best method to determine gas depletion in gaps is to use kinematics to constrain the H_2 pressure gradients (Teague & Foreman-Mackey, 2018) and thus the amount of CO chemical processing that might be happening (Alarcón et al., 2021)

Using the new CO depletion profiles for our deep gas gap models, we find that the gap temperature increases by upwards of 10% compared to a model with a smooth gas surface density. Figure 3.10 shows the difference in temperature between our smooth gas model, and our gapped models, both of which match the observed CO radial profiles. The increase in temperature in the gap arises due to the decreased UV opacity from the depletion of small grains, allowing more flux to enter the region. There is a region in the atmosphere above the heated layer that is cooler than a smooth gas surface density model by over 10%. This occurs at the undershoot region where the gas temperature is lower than the dust temperature due to atomic lines becoming major coolants. In the gas gap models, this cooler, optically thick layer is at a slightly lower height.

We also compare the observed emitting surface of the CO J = 2-1 line to the model with a deep gap at 86 au in Figure 3.11. There is limited emitting surface information for $C^{18}O$ J = 2-1 at the location of the 48 au gap, thus we focus on the gap farthest out. The models with 1 M_J planet gaps showed very little variation compared to the smooth model. The 4.45 M_J model provides the best insight into how a significant deviation in the gas surface density could affect the emitting surface and the degeneracy between the H_2 surface density and CO abundance. At the location of the gap, each CO isotopologue 2-1 transition emits from a lower layer, with ^{13}CO and $C^{18}O$ showing the strongest change in height ($<$ 6 au). This suggests that in highly gas-depleted gaps the degeneracy between the H_2 surface density and CO abundance can be broken. An even more significant difference between the two models is highlighted in the $C^{18}O$ J = 2-1 emitting surface. Just beyond the gap at 86 au, the model with a deep gap in the surface density follows the observed emitting surface more so than the model with a smooth surface density and structured CO depletion profile. Exploring the limits of the degeneracy between CO and H_2 is beyond the scope of this study, however extracting and comparing observed and simulated emitting surfaces may be an interesting tool to use in the future.

3.5 Conclusion

Using high spatial resolution observations of ^{12}CO J=2-1, ^{13}CO J=2-1, 1-0, $C^{18}O$ J=2-1, 1-0, and $C^{17}O$ 1-0 from the ALMA MAPS large program in concert with the thermo-chemical code RAC2D, we derive a 2D thermal structure for the disk around Herbig Ae star HD 163296. Our conclusions are the following:

1. We derived a 2D thermal structure for the disk around Herbig Ae star HD 163296 that reproduces six spatially resolved rotational transition lines of CO and its isotopologues, in

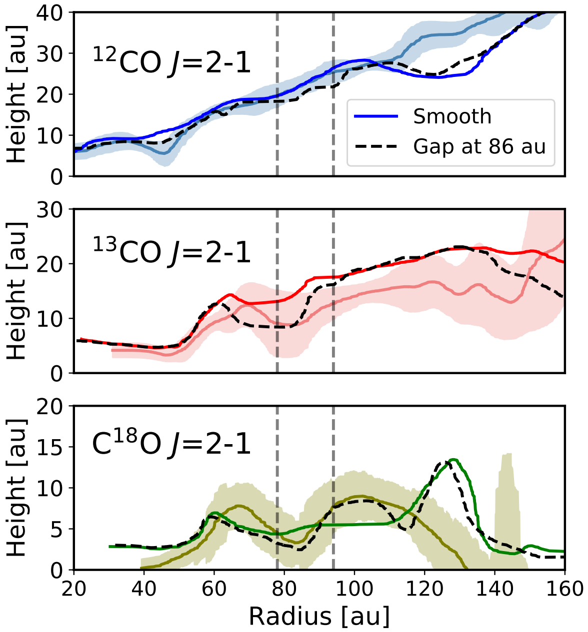

Figure 3.11 *Emitting surface of* ^{12}*CO,* ^{13}*CO, and C*^{18}*O J=2-1 in a model that uses a depletion of CO (solid line), and a model that has a gap in the gas surface density at 86 au (dashed black line) as compared to observations (thick line).*

addition to the observed SED, structures observed in the continuum, the predicted HD flux remains below the observed upper limit, and we reproduce observed fluxes of 19 higher J level transitions of ^{12}CO.

2. The derived temperature agrees well with empirically derived temperatures and calculated emitting heights. This temperature structure represents the full 2D thermal structure, filling in temperature information at spatial locations which observations do not directly probe.
3. We calculate a CO depletion profile which shows a relative enhancement of CO within the CO snowline, a slightly lower depletion value between the CO snowline and 250 au, and then a significant drop of that can be explained via CO chemical processing.
4. Using the derived thermal structure, we predict a midplane snowline location for CO of 60 au which corresponds to a freeze out temperature of 18 K. We also find an upper mass limit of 0.35 $M_{\odot}$.
5. The temperature is locally enhanced in the mm continuum gaps at 48 and 86 au. This is true both for gaps consisting of only large grain depletion, and those with large, small grain and gas depletion. The temperature within the gap increases slightly when gas and small dust are depleted in addition to large grains, by at most 10% in the case of significant depletion.

CHAPTER 4

UV-driven Chemistry as a Signpost for Late-stage Planet Formation

This chapter published in the Nature Astronomy Journal (Calahan et al., 2023) and was completed in collaboration with Edwin Bergin, Arthur D. Bosman, Evan A. Rich, Jennifer B. Bergner, L. Ilsedore Cleeves, Viviana V. Guzmán, Jane Huang, John D. Ilee, Charles J. Law, Romane Le Gal, Karin I. Öberg, Richard Teague, Catherine Walsh, David J. Wilner, and Ke Zhang. The paper is reproduced here under the non-exclusive rights of republication granted by the Nature Editorial board to the authors of the paper.

Abstract

The chemical reservoir within protoplanetary disks has a direct impact on planetary compositions and the potential for life. A long-lived carbon-and nitrogen-rich chemistry at cold temperatures (≤ 50 K) is observed within cold and evolved planet-forming disks. This is evidenced by bright emission from small organic radicals in 1–10 Myr aged systems that would otherwise have frozen out onto grains within 1 Myr. We explain how the chemistry of a planet-forming disk evolves from a cosmic-ray/X-ray-dominated regime to a ultraviolet-dominated chemical equilibrium. This,in turn, will bring about a temporal transition in the chemical reservoir from which planets will accrete. This photochemical dominated gas phase chemistry develops as dust evolves via growth, settling and drift, and the small grain population is depleted from the disk atmosphere. A higher gas-to-dust mass ratio allows for deeper penetration of ultraviolet photons is coupled with a carbon-rich gas (C/O $>$ 1) to form carbon-bearing radicals and ions. This further results in gas phase formation of organic molecules, which then would be accreted by any actively forming planets present in the evolved disk.

Main

Protoplanetary disks are the natal environments for planets. Disks have three main components: a pebble-rich dusty midplane (dust grain radius $>\sim$ 1mm), a gaseous atmosphere extending well above(Miotello et al., 2022) and radially beyond (by a factor of $\sim$2(Ansdell et al., 2018)) the pebble-rich midplane, and a small dust population (radius $<$ 10 μm) that is coupled to the gas. Each component of the protoplanetary disk has an impact on shaping the chemistry of actively forming planets. The solid cores of giant planets must form over a short timescale ($\sim$1 Myr) for the eventual planet to obtain its full mass over the course of a typical lifetime of gas in a disk (3-10 Myr(Haisch et al., 2001)) and to explain the widely observed gap and ring structures that are thought to be indicative of planet formation(Andrews et al., 2018). The compositions of pebbles and their icy mantles directly influence the final composition of a solid planetary core (Öberg et al., 2011a; Johansen & Lambrechts, 2017). After a core becomes sufficiently massive, planets start to accrete material from the gaseous reservoir surrounding the pebble-rich midplane of a protoplanetary disk to form their atmospheres (Lambrechts et al., 2014). It remains difficult to directly probe the gas within the planet-forming midplane due to the high dust densities leading to elevated dust optical depths that mask line emission, as well as cold temperatures which leads to the freezing out common gas tracers such as CO onto dust grains. However, constraining the chemical environment of the planet-forming midplane is essential to connect sub-mm observations probing the warm intermediate regions above the disk midplane to the composition of actively forming planets.

The molecules CH_3CN and HC_3N are two of many complex organic molecules (loosely defined as a molecules with at least four atoms, including multiple carbon atoms) that could act as basic precursors to prebiotic molecules(Powner et al., 2009; Ritson & Sutherland, 2012; Sutherland, 2015). CH_3CN and HC_3N have been observed and spatially resolved towards the protoplanetary disks around six young stars: GM Aur, AS 209, HD 163296, MWC 480, LkCa 15, and V4046 Sgr (Bergner et al., 2018; Ilee et al., 2021; Kastner et al., 2018; Öberg et al., 2015). CH_3CN has also been spatially resolved observed toward the TW Hya disk(Loomis et al., 2018), and a couple of small ($\approx$4 source) surveys have detected unresolved CH_3CN or HC_3N emission from other young stellar objects(Chapillon et al., 2012). These molecules exhibit bright emission signifying high gas phase abundances and column densities (N_{Total}=10^{12}-$10^{13}\mathrm{cm}^{-2}$ (Bergner et al., 2018; Ilee et al., 2021)). CH_3CN is an excellent probe of gas temperature due to multiple transitions tracing a range of energy states [lowest energy state $E_L \approx$5 K, spanning lower energy states over ΔE_L=$\sim$100 K] that can be observed simultaneously. Each *J*-transition (where *J* is the rotational quanum number) has a series of *K*-ladder transitions (where *K* is the quantum number of angular momentum along the molecular axis) which are only sensitive to collisions, thus the ratio between *K*-transitions depends only on the gas density and temperature. The *K*-transitions span a large range of temperatures and are sufficiently close in frequency to observe in one spectral setting with the *Atacama Large Millimeter/submillimeter Array (ALMA)*. Analyses of rotational diagrams(Goldsmith & Langer, 1999) made from CH_3CN observations demonstrate an origin in gas with a temperature between 25-50 K(Ilee et al., 2021), well below the expected desorption temperature (100-124 K(Corazzi et al., 2021)). Thus, the brightly observed flux from this species and similar nitriles and organics like HC_3N, and CH_2CN(Canta et al., 2021) present a chemical conundrum as they should not be present in the gaseous state; rather, they should be frozen on cold grain surfaces. Where CH_3CN and other carbon-rich molecules reside and how they are replenished in the gas phase has a substantial impact on our understanding of prebiotic enrichment into gaseous planet atmospheres. The traditional solution to this apparent discrepancy has been to turn to grain-surface chemistry. Simple carbon- and nitrogen-bearing molecules can undergo hydrogenation or other reactions to form complex organics on the surface of a grain that then non-thermally desorb the grain intact. This solution has been used to explain the organic inventories locked onto pebbles and icy grains (Öberg et al., 2011a; Bergner & Ciesla, 2021). This dust chemistry path requires both an intact photodesorption rate of CH_3CN from the grains of 10^{-3} mols/photon(Walsh et al., 2014; Loomis et al., 2018) and a reactive desorption efficiency(Vasyunin & Herbst, 2013) of 1%. Laboratory experiments find an intact photodesorption efficiency of CH_3CN to be orders of magnitude less efficient (10^{-5} mols/photon(Basalgète et al., 2021)) and reactive desorption has not been well studied in laboratory experiments for these species. We posit here that there is a simpler alternative based solely on disk evolution processes that have been previously theorized and observed which link the disk gas chemistry to planet formation. This involves two ingredients: (1) an elevated C-to-O ratio in the gas and (2) greater penetration of UV photons due to a reduction in the total surface area of small grain population due to pebble formation. These combine to power a state of photo-chemistry equilibrium.

There has been mounting evidence for an elevated C-to-O gas phase ratio at large radial distances in evolved and cool gas-rich protoplanetary disks. Brighter than expected emission from small hydrocarbons such as C_2H (Miotello et al., 2019; Bosman et al., 2021b) and complex organics such as c-C_3H_2 (Cleeves et al., 2021) in disks and HC_3N and CH_3CN in photon-dominated regions(Le Gal et al., 2019) have independently suggested a C-to-O ratio well above the solar abundance ratio (C-to-O$\approx$0.55) (Asplund et al., 2021). As a radical, C_2H has a short lifetime ($<$1000 years), but it is found to be abundant in the gas. Bosman et al. 2021(Bosman et al., 2021b) find that the only way to reproduce the high column densities observed was to increase the C-to-O ratio throughout the full disk to between 1-2. They found that it was also necessary for C_2H to exist in high density gas while remaining above the disk midplane (height/radius$\approx$0.1-0.2) where UV photons dominate the high-energy photon budget. Together, this produces a long-lived carbon-rich gas phase cycle in photochemical equilibrium(Bosman et al., 2021b). One critical factor is that C_2H is predicted and is observed to exist above the disk midplane(Law et al., 2021d). In contrast, CH_3CN has been observed to emit closer to the midplane(Ilee et al., 2021). Extending the carbon-rich chemical environment that is used to explain C_2H observations to the midplane could allow for gas phase formation of complex molecules in the planet-forming zone. Elevated C-to-O ratios would be necessary to supply the materials to create hydrocarbons and nitriles. However, this alone would not alleviate the issue of CH_3CN and HC_3N existing in the gas at temperatures at which they should be frozen and locked onto grains.

A non-thermal desorption mechanism is needed to increase the number of molecules that are being desorbed from the grains, either intact or as fragments of larger molecules. If the disk atmosphere is small-dust rich, with a gas-to-dust ratio close to the typical interstellar medium (ISM) mass ratio (gas-to-dust = 100) then UV radiation cannot penetrate deep into the disk. In this case, only high energy radiation (X-rays and cosmic rays) can penetrate the dust and gas and drive the chemistry within and near the midplane. Small dust grains are the main opacity source for UV photons which are readily produced by the young and active star. As the protoplanetary disk evolves, small dust grains agglomerate and eventually settle downwards and drift inward radially as they grow in size(Andrews & Birnstiel, 2018; Birnstiel et al., 2012), decreasing the total surface area of the small grain population. As the main opacity source begins to deplete, UV photons can penetrate deeper into the disk. Here, complete desorption of CH_3CN or HC_3N is inhibited due to the dense and cold environment(Le Gal et al., 2019). This mechanism would have an effect on all molecules residing on grains, and a brief discussion regarding this can be found in the Supplemental Materials, in the section 'Implications on other molecules'.

The combined effect of a high C-to-O ratio and excess UV flux allows for complex molecules to exist within the gas phase at cold, midplane temperatures. Thus bright hydrocarbon and nitrile (i.e. C_2H, CH_3CN) emission from the cold midplane acts as a signpost for an evolved dust population, coincident with an advanced stage of planet formation including the accumulation of gas-giant atmospheres. The chemical scenario we put forward, comparing early and late-stage disk environments is shown in Figure 4.1. The disks observed in the Molecules with ALMA at Planet-forming Scales (MAPS) large program(Öberg et al., 2021) provide plausible support for this theory. The youngest disks in the MAPS sample reside around IM Lup and AS 209 which are on the order of 1-2 Myr old(Öberg et al., 2021). Towards the youngest source, IM Lup, there is no detection of CH_3CN nor HC_3N. AS 209 has detections of CH_3CN and HC_3N which suggest both molecules emit from $z/r>0.1$. The disk systems surrounding stars >6 Myr have CH_3CN detected at $z/r<0.1$ as determined by the modeled thermal structure and detected rotational temperature from the K-ladder transitions. This complex organic-rich midplane will influence the atmospheres of planetary companions. It is worth noting that the oldest disk systems in the MAPS program exist around Herbig stars while the youngest systems are T Tauri stars. The UV-bright spectrum innate to Herbig stars may additionally influence the push of complex molecules towards the planet-forming midplane. Currently, the MAPS sample contains the bulk of the resolved CH_3CN and HC_3N data towards protoplanetary disks. To explore the effect of the stellar spectrum on CH_3CN and HC_3N

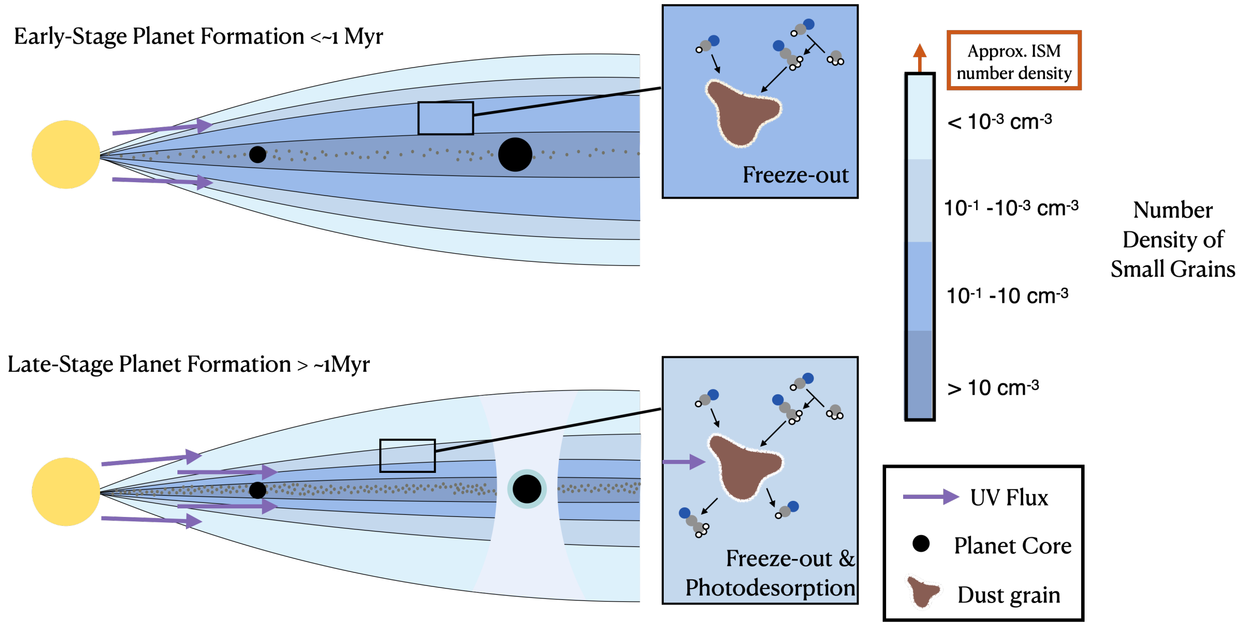

Figure 4.1 *A schematic highlighting the physical evolution of a disk and how that physical environment can affect the chemistry.* At the top, we show a disk with a large amount of small dust that acts to block UV photons. As the small dust settles, UV photons make their way deeper into the disk, allowing for photodesorption of complex species off grains. Now, there is a cycle of carbon chemistry that can be observed in the gas phase.

emission more disks with a wide range of stellar host masses would need to be observed.

To test the validity of this proposed end-stage chemistry, we first explored single point models representative of the disk midplane with corresponding cold temperatures and high gas densities (approximately 35 K, 5×10^{11} mol/cm^{-3}). We varied the gas-to-dust mass ratio and initial carbon abundance among other physical and chemical variables including the nitrogen abundance, dust extinction, and ionization rate. We found that the gas phase CH_3CN abundance was the most sensitive to the gas-to-dust ratio and initial gas phase carbon abundance. We then produced a thermo-chemical model representing the disk around the Herbig Ae star HD 163296. This disk is old (approx. 7.6 Myr)(Bergner et al., 2019) and is nearby at 101 pc(Gaia Collaboration et al., 2018) and has observed jets and winds (Booth et al., 2021; Xie et al., 2021). The HD 163296 disk has been widely observed in multiple gas and dust tracers with high spatial resolution ($\sim$10 au) with clear gap and ring structures typically assumed to be associated with active planet formation(Andrews et al., 2018; Öberg et al., 2021). There is bright CH_3CN emission coming from $\sim$35 K gas as well as bright emission from HC_3N and HCN(Ilee et al., 2021; Bergner et al., 2021). Our modeling efforts follow that of Zhang et al. 2021(Zhang et al., 2021b), and Calahan et al. 2021b(Calahan et al., 2021b) which set up a thermo-chemical model of the HD 163296 disk by reproducing the mm dust-continuum observations, the spectral-energy distribution (SED), the full

Table 4.1. Modeling Parameters: TW Hya & HD 163296

Parameters	**TW Hya**			**HD 163296**		
	Gas	Small Dust	Large Dust	Gas	Small Dust	Large Dust^a
Mass ($M_\odot$)	0.025	1.0×10^{-4}	4.0×10^{-4}	0.14	2.6×10^{-5}	0.024
Ψ	1.1	1.2	1.2	1.08	1.08	1.08
γ	0.75	0.75	1.0	0.8	0.8	0.1
h_c (au)	42	42	8.4	8.44	8.44	n/a
r_c (au)	400	400	400	165	165	n/a
r_{in} (au)	0.1	0.5	1	0.45	0.45	0.45
r_{out} (au)	200	200	200	600	600	240

Note. — Final values of the TW Hya and HD 163296 models that reproduce CO, HD, CH_3CN, HCN, and HC_3N observations when available. r_{in} and r_{out} are the radial inner and outer limits of the disk, beyond these limits there is assumed to be no gas nor dust. ^{a} The surface density of the large dust distribution in HD 163296 is empirically set by continuum observations, thus it is not smooth and it is not dictated by the parametric equations.

line intensity and morphology of six CO isotopologue transitions, and the vertical distribution of the optically thick lines. The model of HD 163296 started with a gas-to-small dust ratio of the disk equal to 500(Zhang et al., 2021b) which was needed to reproduce the disk's SED.

Results

To produce this end-stage chemical environment, we deplete the small dust mass by a factor of 10 throughout the disk of HD 163296 making the new gas-to-dust mass ratio above the pebble disk midplane equal to 5,000. We then enhanced the initial gas phase carbon abundance in the system in the form of C, CH_4, or C_2H, increasing the overall gas phase carbon-to-oxygen ratio in both disks to above unity. There are two possible sources for excess carbon in protoplanetary disks, either through the destruction of refractory carbon grains(Bosman et al., 2021a) or CO depletion through mechanisms such as reactions with ionized molecules and atoms such as He^+ or H_3^+(Schwarz et al., 2018) and a series of chemical and freeze-out processes. We note that while signatures of CO depletion are found in the HD 163296 disk(Zhang et al., 2021b; Calahan et al., 2021b), CO destruction likely only occurs in environments with a high cosmic-ray flux [$2\times10^{-17}s^{-1}$](Schwarz et al., 2018). Additionally, CO destruction would supply equal amounts of carbon and oxygen, while we seek to enhance carbon over oxygen. Our thermo-chemical model is run for a full megayear (Myr), after which the chemistry reaches an equilibrium. Notable chemical feedback due to dust evolution is predicted to occur over scales of $\sim$1 Myr(Krijt et al., 2018; Van Clepper et al., 2022), thus we use $\sim$1 Myr as an approximate length of time for the chemical environment to transition from ‘early-stage’ to ‘late-stage’ dust evolution and subsequently exist in a state of photochemical equilibrium. Gas phase chemical reactions and rates were taken from the chemical network derived in Bosman et al. 2018(Bosman et al., 2018b) which in turn relies on the UMIST Database for Astrochemistry Rate12 version(McElroy et al., 2013) (see Methods section for more details). We found that regardless of the carrier of carbon, using a C/O = 1-2 and a factor of 10 depletion of small dust roughly reproduces line ratios and fluxes of the radial intensity profiles of CH_3CN, HC_3N, and HCN (see Figure 6.2). In this proposed scenario, $\sim$96% of the total mass of CH_3CN continues to reside frozen out onto grains, but the increase in UV flux allows for sufficient CH_3CN to exist and be formed in the gas to reproduce observed radial intensity profiles and column densities.

Figure 4.3 shows the two-dimensional number densities of CH_3CN and HC_3N. The inner $\sim$20 au exhibited brighter or more centrally peaked emission than was seen in observations if the C-to-O ratio = 2 throughout the full disk. To counteract this, we set the C-to-O ratio = 0.47, or the ISM ratio, inside of ($\sim$20 au) where Zhang et al. 2021(Zhang et al., 2021b) found an ISM ratio of H_2/CO (See Supplementary Figure 2). The inner disk emission remains slightly brighter than observed in HCN and CH_3CN (see Figure 6.2) with this alteration. This could be accounted for via a depletion in the nitrogen abundance within the N_2 ice line, a strong buildup of pebbles around the water ice line ($\sim$5au), a lower HCN desorption energy, or a combination of these effects. Additionally, the observations may also be affected by processes such as beam smearing and a higher dust opacity than modeled. A comparison model without a depletion in small dust mass is shown in Supplementary Figure 5.

Discussion

HC_3N and CH_3CN are built up in the gas from simple carbon and nitrogen-based volatiles (see Methods section “Chemical Reactions" for details). A reservoir of these more simple molecules is maintained in the gas phase due to photodesorption from dust grain surfaces by an enhanced UV-field. The main destruction products from CH_3CN and HC_3N are simple volatiles that can cycle back to create larger nitrile molecules including their original parent molecule. While there are enough complex organic molecules in the gas phase to observe bright emission, the majority of the CH_3CN, HC_3N, and HCN near the midplane still remains frozen out onto grains. The carbon-rich gas reservoir and UV-dominated disk together allow for a cycle of carbon chemistry to remain

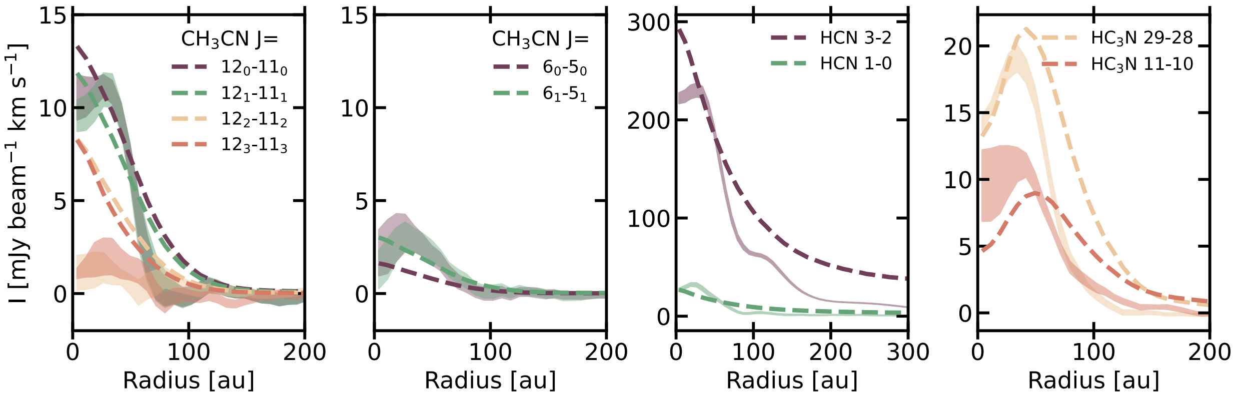

Figure 4.2 *Radial intensity profiles of the observed complex organic molecules and HCN towards the disk around HD 163296.* The molecules shown are CH_3CN, HCN, and HC_3N (left to right with two J transition of CH_3CN shown in the first two panels). Solid thick lines in the background correspond to the observations derived from Ilee et al 2021(Ilee et al., 2021) and Guzmán et al. 2021(Guzmán et al., 2021) (which utilized Law et al. 2021(Law et al., 2021b)) while dashed lines correspond to modeled radial profiles. Our final model includes an increase in C/O ratio beyond 20 au and a depletion of small dust and represents 1 Myr of chemistry. This model can simultaneously fit the flux, line ratios, and general morphology of the observed radial profiles of these complex organic molecules.

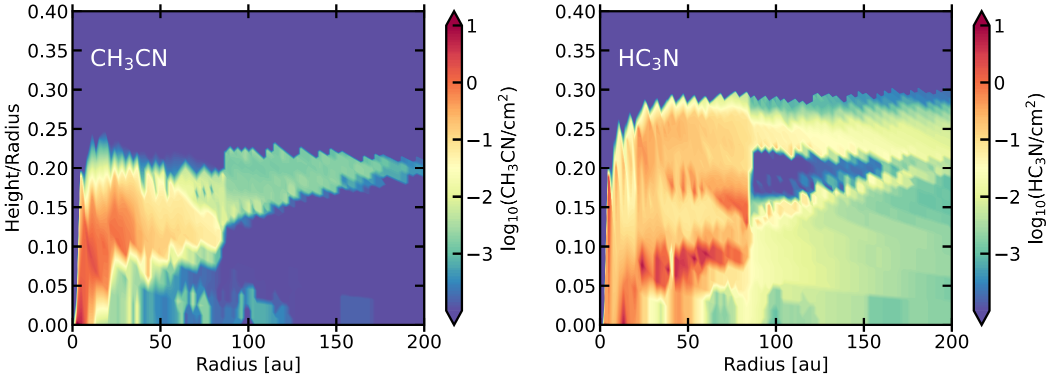

Figure 4.3 *The radial and vertical number density distributions of CH_3CN and HC_3N* The density distributions were determined by our final HD 163296 model with an increase in C/O ratio beyond 20 au and a depletion of small dust. This distribution produced the radial profiles shown in Figure 6.2. A $z/r<0.1$ is good approximation for the midplane of the disk, and both CH_3CN and HC_3N emit partially from the midplane. A comparison can be made with Figure C.6 which lacks the inclusion of small dust depletion.

active in the gas phase. This implies that actively accreting gas giants will build their atmosphere out of this complex nitrile-enhanced material. Gas giant planets with atmospheres containing a chemical make-up with a C-to-O ratio >1 can be explained by the natural evolution of dust and the observed high C-to-O ratios within protoplanetary disks. This environment could be extended to the inner disk in some cases, as studies such as Najita et al. 2011(Najita et al., 2011) and Anderson et al. 2021(Anderson et al., 2021) posit a higher than solar C-to-O ratio within the inner disk to account for Spitzer observations of HCN and C_2H_2 around T Tauri stars.

The implications of this end-stage chemistry are far-reaching. Primarily, we put forward a new chemically and physically coupled picture of planet formation and its direct impact on the chemistry of forming planet atmospheres. Within the early stages of planet formation, pebble growth and accretion into solid planet cores has begun, and chemistry onto these cores are influenced primarily by the chemical make-up of large pebbles and their icy mantles. The chemistry active in the midplane during this stage of formation is dominated by X-rays and cosmic rays(Woitke et al., 2009). After timescales of order 1 Myr, at the end-stage of pebble formation, small grains have grown and settled towards the midplane, allowing for UV photons to penetrate deeper in the disk than previously assumed. This excess UV flux in concert with an above solar C-to-O ratio produces a carbon-rich gas phase cycle of production and destruction in the gas surrounding actively forming planets. Bright emission from CH_3CN, HC_3N and other carbon-rich molecules emitting at cold temperatures are a sign-post of this evolved chemical environment. These forming gas giants may accrete this surrounding gas and its chemical signature into their atmosphere, and may be responsible for high C-to-O measurements that have been observed in exo-planetary atmospheres as compared to their host star(Brewer et al., 2017). Secondly, the deeper penetration of UV photons pushes the CO and H_2 self-shielding layers deeper into the disk. Due to this, there are more ions such as C^+ and H^+ throughout the disk than would have been present with a regular (ISM) level of small dust surface area. As the ion-fraction increases so does the area of the disk that is subject to magneto-rotational instability (MRI). In our final model, the UV field increases by a factor of 3-5 in the atmosphere and between 1-2 near the midplane, and thirteen times more gas mass is MRI-active, most notably the gas midplane within 10 au, and then at a z/r=0.1-0.2 within 30 au (see Figure 4). This could be a source of accretion(Gammie & Ostriker, 1996) for older disks. Our proposed UV-dominated carbon-rich gas phase chemistry is a major shift in our understanding of the astrochemistry of planet formation. This transition will have a strong effect on the composition of actively forming planets, disk MRI-activity, and subsequent disk accretion.

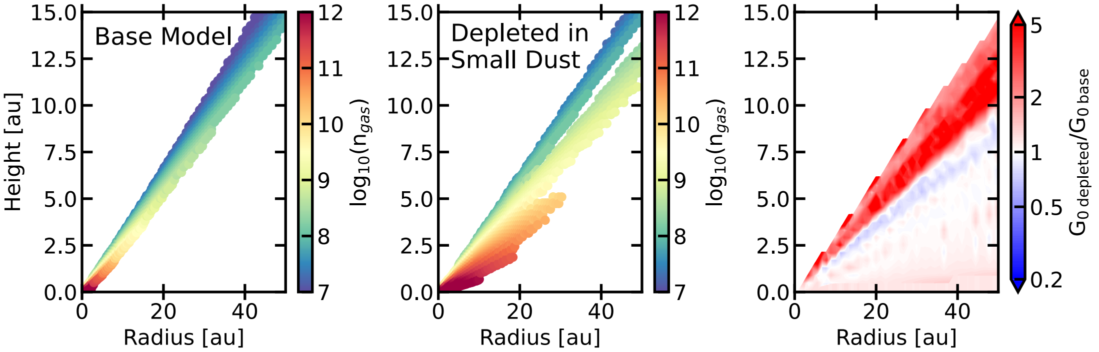

Figure 4.4 *A comparison of the MRI active region within a non-elevated UV environment and an elevated UV environment.* The two left-most plots show regions within the HD 163296 disk which are MRI activated in an environment where small dust is depleted by a factor of 10 in total mass (gas/dust = 5,000 middle plot) and where small dust is not depleted (gas/dust=500 left). The color corresponds to the gas density in mol/cm^3, highlighting the substantial increase in mass that is MRI-active. The right-most plot shows a comparison of the UV field strength through a 'regular' disk and a dust depleted disk. The UV field increases upwards of a factor of 3-5 in the atmosphere of the disk and 1-2 below a z/r=0.2. This has a notable effects on the chemistry of the midplane.

Methods

Observations

For a thorough description of the observations and the techniques used to obtain the CLEAN-ed images and radial profiles of CH_3CN, HCN, and HC_3N towards HD 163296 see Czekala et al. 2021(Czekala et al., 2021), Law et al. 2021(Law et al., 2021b), and Öberg et al. 2021(Öberg et al., 2021). A description of the observations of CH_3CN towards TW Hya can be found in Loomis et al. 2018a(Loomis et al., 2018). A brief summary of these observations are as follows.

- HD 163296 -

The data for HD 163296 is from the MAPS large program (Project ID 2018.1.01055.L)(Öberg et al., 2021). The image cubes were produced using the `tclean` task in the Common Astronomy Software Applications (CASA) package, version 6.1.0(McMullin et al., 2007). Keplerian masks based on the disk geometric parameters were used in the CLEANing process and the final images were then corrected for the Jorsater & van Moorsel effect to ensure that the image residuals are in units consistent with that of the CLEAN model. For all lines, we used the beam-circularized and uv-tapered images, which had synthesised beam sizes of 0."3. All radial intensity profiles were generated by deprojecting and azimuthally-averaging zeroth moment maps using the GoFish python package.

-TW Hya-

CH_3CN was observed towards TW Hya as a part of ALMA project 2016.1.01046.S. Each emission line was individually imaged using `CLEAN` and the synthesised beam for each transition were matched using small uv-tapers to $1\farcs05$ x $0\farcs83$. A Keplerian mask was used to extract the flux for each transition. See Loomis et al. 2018a(Loomis et al., 2018) for more details.

Modeling

Simple single point models of the disk environment were utilized to quickly and efficiently understand the chemical impacts of different physical and initial chemical conditions. Our chemical network is derived from Bosman et al. 2018(Bosman et al., 2018b) which in turn is derived from the UMIST "RATE12" network(McElroy et al., 2013), and for this study we disregarded most grain-surface chemical reactions in order to isolate gas-phase formation of CH_3CN. After our results from the modeling suggested a higher gas/dust ratio and carbon content, we turned to more comprehensive thermo-chemical codes which model the thermal physics and chemical evolution throughout the whole disk. The code RAC2D (https://github.com/fjdu/rac-2d)(Du & Bergin, 2014), was used to create models of the disks around TW Hya and HD 163296. The 2D temperature, density, and molecular abundance results were used to simulate observations of each disk with a raytracing code: RADMC-3D(Dullemond et al., 2012b). A brief description of the physical code of RAC2D is given below; a detailed description of the code can be found in Calahan et al 2021a(Calahan et al., 2021c).

RAC2D takes into account a gas and dust structure and stellar radiation field and computes the gas and dust temperature and chemical structure over time. Our model consists of three mass components: gas, small dust, and large dust grains. The spatial extent of each component is given by a global surface density distribution (Lynden-Bell & Pringle, 1974), which is widely used in protoplanetary disk modeling and corresponds to the self-similar solution of a viscously evolved disk.

$$\Sigma(r) = \Sigma_c \left(\frac{r}{r_c}\right)^{-\gamma} \exp\left[-\left(\frac{r}{r_c}\right)^{2-\gamma}\right], \tag{4.1}$$

r_c is the characteristic radius at which the surface density is Σ_c/e where Σ_c is the characteristic surface density, and γ is the power-law index that describes the radial behavior of the surface density.

A 2D density profile for the gas and dust populations can be derived from the surface density profile and a scale height:

$$\rho(r,z) = \frac{\Sigma(r)}{\sqrt{2\pi}h(r)} \exp\left[-\frac{1}{2}\left(\frac{z}{h(r)}\right)^2\right], \tag{4.2}$$

$$h = h_c \left(\frac{r}{r_c}\right)^{\Psi}, \tag{4.3}$$

where h_c is the scale height at the characteristic radius, and Ψ is a power index that characterizes the flaring of the disk structure. The modeling parameters used for TW Hya and HD 163296 are shown in Table 1.

For both TW Hya and HD 163296 models, each dust population follows an Mathis, Rumpl, and Nordsieck (MRN) grain distribution $n(a) \propto a^{-3.5}$ (Mathis et al., 1977), where 'a' indicates the size of the grain. The small dust grains have radii between 5×10^{-3} - 1μm, and the large grains have radii between 5×10^{-3} - $10^3\mu$m. The large dust population is settled in the midplane with a smaller vertical extent and radial extent (gas extends ∼5 and 2.5 times above and beyond, respectively). This settled large grain population is the result of dust evolution, namely growth in concert with vertical settling to the midplane and radial drift. For the HD 163296 model, the large grain population has a unique, non-smooth, surface density profile that reproduces the millimeter continuum observations of the HD 163296 disk(Isella et al., 2018; Zhang et al., 2021b). Opacity values for the dust are calculated based on Birnstiel et al. 2018(Birnstiel et al., 2018). Large dust grains consist of water ice(Warren & Brandt, 2008), silicates(Draine, 2003), troilites and refractory organics(Henning & Stognienko, 1996). Small dust grains consist of 50% silicates and 50% refractory organics. Further discussion on the modeling efforts for TW Hya can be found in Calahan et al. 2021a(Calahan et al., 2021c) and for HD 163296 in Calahan et al. 2021b(Calahan et al., 2021b).

The thermo-chemical model resulted in 2D distributions of the gas and dust temperature, density, and molecular abundances. These were used as inputs for the raytracing code RADMC-3D(Dullemond et al., 2012b). The molecular properties of CH_3CN, HC_3N, and HCN were taken from the Leiden Atomic and Molecular Database (LAMDA(Schöier et al., 2005)), with some molecular parameters updated according to data from the Cologne Database for Molecular Spectroscopy (CDMS(Müller et al., 2001, 2005)). The result from RADMC-3D was a 3D image cube of the molecular emission across velocity space. We utilized `GoFish`(**?**) to compress these 3D images into zeroth moment maps and radial profiles which were then directly compared to the azimuthally-averaged observations.

Chemical Reactions

The chemical reaction network utilized in this work comes from Bosman et al. 2018(Bosman et al., 2018b) which in turn relies on the Rate12 version of the UMIST Database for Astrochemistry(McElroy et al., 2013): a network that is widely used across astrochemical modeling efforts. In our network there are 6,302 gas phase reactions and we have limited the grain-surface reactions to twelve. We kept grain-surface reactions that involved the formation of H_2, CH_2OH, CH_3OH, CO_2, H_2O and NH_3 due to each of these species being well-studied in the laboratory and come with strong evidence for active two-body chemistry on dust grains(Allen & Robinson, 1977; Hasegawa et al., 1992; Goumans et al., 2008; Ioppolo et al., 2008, 2010; Fuchs et al., 2009; Oba et al., 2012; Ruffle & Herbst, 2001) (see Table 2). Both thermal adsorption and desorption are taken into account for every molecule in the network. Our network contains molecules with at most eleven carbon atoms, and at most twelve total atoms. We run our thermo-chemical model for 1 Myr as the CH_3CN and HC_3N chemistry reaches an equilibrium after this time period (see Supplementary Figure 3). In our evolved disk model, the main formation pathways for CH_3CN once the chemistry has reached equilibrium is as follows:

$$\mathrm{CH_3^+ + HCN \rightarrow CH_3CNH^+ + e^- \rightarrow CH_3CN + H}$$

This reaction in the gas phase is the primary formation pathway for CH_3CN, thus there is a strong reliance on HCN existing in the gas phase even at cold temperatures below its measured sublimation temperature (∼8

5-103 K(Bergner et al., 2022)) and an ionization source (UV photons) to produce CH_3^+. HC_3N can be readily produced by a number of different ways including:

$$\mathrm{N + CH_2CCH \rightarrow HC_3N + H_2}$$

$$\mathrm{CN + C_2H_2 \rightarrow HC_3N + H}$$

$$\mathrm{H + C_3N^- \rightarrow HC_3N + e^-}$$

The formation of HC_3N strongly relies on the existence of carbon-rich molecules including radicals (CN) and ions (C_3N^-).

Table 4.2. Dust Surface Reactions

Reaction	Reference
$gH + gH \rightarrow gH_2$	Hasegawa, Herbst, & Leung 1992(Hasegawa et al., 1992)
$gH + gOH \rightarrow gH_2O$	Ioppolo et al. 2010(Ioppolo et al., 2010)
$gH + gH_2O_2 \rightarrow gH_2O + gOH$	Ioppolo et al. 2008(Ioppolo et al., 2008)
$gH + gCH_3OH \rightarrow gH_2 + gCH_2OH$	Extrapolated from Fuchs et al. 2009(Fuchs et al., 2009)
$gH + gCH_2OH \rightarrow gCH_3OH$	Extrapolated from Fuchs et al. 2009(Fuchs et al., 2009)
$gH_2 + gOH \rightarrow gH_2O + gH$	Oba et al 2012(Oba et al., 2012)
$gOH + gCO \rightarrow gCO_2 + gH$ [a]	Ruffle & Herbst 2001(Ruffle & Herbst, 2001)
$gO + gCO \rightarrow gCO_2$ [a]	Goumans & Brown 2008(Goumans et al., 2008)
$gO + gHCO \rightarrow gCO_2 + gH$	Goumans & Brown 2008(Goumans et al., 2008)
$gH + gNH_2 \rightarrow gNH_3$	Allen & Robinson 1977(Allen & Robinson, 1977)

Note. — The complete list dust surface reactions accounted for in this study. [a]Have additional special treatment for three body reactions

CHAPTER 5

Water UV-shielding in the terrestrial planet-forming zone: Implications for Oxygen-18 Isotope Anomalies in $H_2^{18}O$ Infrared Emission and Meteorites

This chapter published in the Astrophysical Journal Letters Series (Calahan et al., 2022) and was completed in collaboration with Edwin Bergin and Arthur D. Bosman. The paper is reproduced here under the non-exclusive rights of republication granted by the American Astronomical Society to the authors of the paper.

Abstract

An understanding of the abundance and distribution of water vapor in the innermost region of protoplanetary disks is key to understanding the origin of habitable worlds and planetary systems. Past observations have shown H_2O to be abundant and a major carrier of elemental oxygen in disk surface layers that lie within the inner few au of the disk. The combination of high abundance and strong radiative transitions leads to emission lines that are optically thick across the infrared spectral range. Its rarer isotopologue $H_2^{18}O$ traces deeper into this layer and will trace the full content of the planet forming zone. In this work, we explore the relative distribution of $H_2^{16}O$ and $H_2^{18}O$ within a model that includes water self-shielding from the destructive effects of ultraviolet radiation. In this Letter we show that there is an enhancement in the relative $H_2^{18}O$ abundance high up in the warm molecular layer within 0.1-10 au due to self-shielding of CO, $C^{18}O$, and H_2O. Most transitions of $H_2^{18}O$ that can be observed with *JWST* will partially emit from this layer, making it essential to take into account how H_2O self-shielding may effect the H_2O to $H_2^{18}O$ ratio. Additionally, this reservoir of $H_2^{18}O$-enriched gas in combination with the vertical "cold finger" effect might provide a natural mechanism to account for oxygen isotopic anomalies found in meteoritic material in the solar system.

5.1 Introduction

It is expected that the vast majority of solar-type stars host an exoplanet within 1 au (Johnson et al., 2010; Mulders et al., 2018). As a result, it can be assumed that the inner gaseous region of protoplanetary disks must be a hospitable environment for active planet formation. Typical temperatures place nearly all primary volatile carriers of carbon, nitrogen, and oxygen into the gas within surface layers providing a rich environment for astronomical observations and constraint (Pontoppidan et al., 2014). Volatiles (i.e. CO, H_2O, CO_2) are potential starting points for the creation of complex molecules and the ice-coatings of pre-planetary pebbles (Wang et al., 2005; Gundlach & Blum, 2015). These simple pre-cursors have been widely observed towards gas-rich disks within the 0.1-10 au region around young stars using the *Spitzer* space telescope (i.e. Carr & Najita, 2008; Pontoppidan et al., 2010; Salyk et al., 2011a). Mapping the spatial extent and abundance of volatile molecules within the inner disk is essential knowledge used to piece together the connection between the chemical reservoir of a gas-rich disk and the resulting planets.

The *JWST* mission will provide improved spectral resolution access to the inner disk region (JWST-MIRI: $\lambda/\Delta\lambda = 2000 - 3000$; Rieke et al., 2015), as compared to *Spitzer*'s InfraRed Spectrograph ($\lambda/\Delta\lambda = 600$; Houck et al., 2004). Nearly fifty disks will be targeted in the first set of *JWST* observations and will be used to enhance the study of emissions from volatiles in the terrestrial planet-forming zone. One molecule of high scientific impact is H_2O. Based on previous observations and theoretical work, it is expected that H_2O will be in high enough abundance such that its emission is optically thick (Carr & Najita, 2008). The lesser abundant isotopologue $H_2^{18}O$ is also observable with JWST instruments, and, with reduced optical depth for its emission lines, will be used to infer the abundance and distribution of H_2O using the ratio between ^{16}O and ^{18}O.

The most frequently used value for $^{16}O/^{18}O$ is 550. This value comes from Wilson (1999), and is the average observed ratio for five local ISM sources. This ratio has been seen to vary across the Galaxy following

$$(^{16}\text{O}/^{18}\text{O}) = (58.8 \pm 11.8)\text{D}_{\text{GC}} + (37.1 \pm 82.6) \tag{5.1}$$

where D_{GC} is the distance of a source from the Galactic center (Wilson & Rood, 1994). Within the environment of a protoplanetary disk, however, there are chemical processes that can alter this ratio.

One such process is molecular self-shielding. Self-shielding is a process via which molecules, such as CO, N_2, and H_2, can protect themselves further from the source of radiation from the destructive effects of photodissociation from ultraviolet photons (van Dishoeck & Black, 1988). These molecules are dissociated via a line process, as opposed to molecules with photodissociation cross-sections that are continuous at UV wavelengths (Heays et al., 2017). Thus, molecules closer to the radiation source can absorb UV photons allowing for the lines to become optically thick and, hence, self-shield molecules downstream from the source of UV photons. CO self-shielding can occur in gas-rich disks leading to a relative overabundance of $^{12}C^{16}O$ compared to $^{12}C^{18}O$ and $^{12}C^{17}O$ in the warm disk region (Miotello et al., 2014) because the absorbing lines of the lesser abundant isotopologues have reduced opacity. This process can help explain relatively high $C^{16}O/C^{18}O$ ratios that have been observed in a handful of protoplanetary disks (i.e. Brittain et al., 2005; Smith et al., 2009) and potentially might contribute to isotopic anomalies detected in asteroids and comets as compared to our Sun (Lyons & Young, 2005; Nittler & Gaidos, 2012; Altwegg et al., 2020).

Bethell & Bergin (2009) demonstrated that, because of fast formation rates in hot ($>$400 K) gas, water can also self-shield. Further, this shielding is unique in that it not only shields itself, but shields over a wide range of wavelength space, similar to ozone in the Earth's atmosphere. Thus, water might also operate as a shield for other molecules, a process we call water UV-shielding. The combination of CO self-shielding and H_2O UV-shielding could produce an environment where the H_2O, $H_2^{18}O$, and CO are protected while $C^{18}O$ continues to photodissociate. In this ^{18}O-rich environment, $H_2^{18}O$ will form and continue to be protected, raising the relative abundance of $H_2^{18}O$ with respect to H_2O in specific surface layers. This could have a strong impact on both the $CO/C^{18}O$ and $H_2O/H_2^{18}O$ values, altering them drastically from what is expected within the average ISM. These ratios will be commonly used in future *JWST* observations due to the expected high optical depth of CO and H_2O within the inner disk. Additionally, the spatial extent of any ^{18}O-rich environment relative to where observed $H_2^{18}O$ and H_2O lines emit from will have a strong effect on the determination of H_2O abundance within protoplanetary disks. Having accurate isotopic conversation factors could be critical as it is possible that the inner disk could betray evidence of volatile enhancements due to pebble drift (Ciesla & Cuzzi, 2006; Banzatti et al., 2020).

One final consideration to the chemical make-up of the inner disk is Lyman-α (Ly-α) radiation. The Ly-α transition often contains the vast majority of the energy within the FUV range if present in a stellar spectrum of T Tauri stars (Herczeg et al., 2002; Schindhelm et al., 2012). It is readily observed towards young stars that are actively accreting and posses a gas-rich disk. The Ly-α transition occurs at 1216 Å and can photodissociate water (van Dishoeck et al., 2006). Ly-α is not often taken into account in radiation transfer codes, due to its added complexity of not only scattering off of dust but also atomic Hydrogen, causing the Ly-α photons to scatter isotropically below the hot atomic layer of the disk (Bethell & Bergin, 2011). To explore the strength that both water and CO self-shielding will have on the oxygen isotopic ratio, Ly-α needs to be accounted for.

This paper is a companion to Bosman et al. (2022a), Bosman et al. (2022b), and Duval et al. (2022, in prep.) Bosman et al. (2022a) sets up protoplanetary disk models focused on the innermost region which take into account water UV-shielding and efficient chemical heating processes. These two processes are required in order for a thermo-chemical calculation to reproduce water line emission and observed excitation temperatures from *Spitzer*. Using the same modeling setup, Bosman et al. (2022b) shows that CO_2-to-H_2O ratios can also be achieved, strengthened by additional depletion of excess oxygen beyond the water snowline. Duval et al. (in prep) will focus on the impact of water UV-shielding on the chemical composition of the terrestrial planet forming region.

In this paper we will explore the abundances of both H_2O and $H_2^{18}O$ in the inner most few au of protoplanetary disks where the excitation conditions are favorable for detection of rotational and vibrational emissions at mid-infrared wavelengths. This exploration will use the *Spitzer* observational legacy as a constraint (Pontoppidan et al., 2010; Salyk et al., 2011a), but look forward to JWST observations which will be observing systems where both Ly-α radiation and water UV-shielding will be present.

5.2 Methods

5.2.1 Thermo-chemcial modeling: *DALI*

DALI (Dust And LInes) is a physical-chemical code that accounts for radiation transfer, thermal and chemical calculations throughout a disk (Bruderer et al., 2012; Bruderer, 2013). It contains an isotope chemical network (Miotello et al., 2014) and accounts for molecular self-shielding. For this project, H_2O UV-shielding has been additionally accounted for, see Bosman et al. (2022a) for detail. We utilize a model derived from the AS 209 and corresponding stellar spectrum from Zhang et al. (2021b), and explore the effect of H_2O UV-shielding and Ly-α radiation in flat vs. thick model and two levels of dust settling. We include the ^{18}O isotopologue of every oxygen carrying species in our chemical network.

After an initial radiative transfer calculation, thermal balance, and chemical abundance distribution determination, we account for Ly-α radiation using another code, detailed in the following section. The results from the separate Ly-α radiative transfer calculation are combined with the initial disk radiation field as calculated by DALI. We then calculate a new thermal balance and chemical environment, containing the final distribution of H_2O and $H_2^{18}O$.

Excitation data for both ortho- and para-$H_2^{18}O$ was compiled into a file identical to the format from the Leiden LAMDA database (Schöier et al., 2005).[1] Line excitation data was obtained via the HITRAN database (Gordon et al., 2022)[2] and collisional data from the $H_2^{16}O$ LAMDA file (Faure

---

[1] `https://home.strw.leidenuniv.nl/~moldata/`

[2] `https://hitran.org/`

& Josselin, 2008). This was used for ray-tracing calculations with DALI to determine which lines may be observable and from where in the disk they emit.

5.2.2 Inclusion of Lyman Alpha

The inclusion of the Ly-α is derived from a radiation transfer code described by Bethell & Bergin (2011). Briefly, this code calculates the transport of both FUV-continuum and Ly-α photons. FUV photons are solely affected by the dust distribution, while Ly-α is additionally affected by resonance line scattering. An initial distribution of H and H_2 is derived using the thermo-chemical calculation from DALI, and Ly-α propagates throughout the distribution of gas and dust, scattered by atomic H in the H-rich layer, and eventually scattered and absorbed by dust.

After this calculation, the Ly-α-affected radiation field is combined with the DALI radiation field. The effects of a separate stellar input spectrum are normalized out of the Ly-α radiative transfer results, and a depletion or enhancement factor across wavelengths covered by the Ly-α line and its line wings is calculated. The original DALI radiation field contains Ly-α emission as it would exist if Ly-α-photons scattered normally off of small dust grains only, identically to continuum-UV photons.

5.3 Results

5.3.1 $H_2^{18}O$-Enhanced Region

We find an $H_2^{18}O$-rich environment high up in the molecular region of the disk. Enhanced $H_2^{18}O$ exists in models that range in flaring angle and dust settling parameters. Four models were explored with two different values for scale height and dust settling, and these individual models are detailed in the Appendix of Bosman et al. (2022a). The following figures and discussion are based on the flattest and most highly settled model, which reproduce H_2O and CO_2 spectra simultaneously (see Bosman et al., 2022b). In this model, a region where $H_2O/H_2^{18}O$ dips to approximately 45% of the initial ISM ratio exists at a z/r of 0.16-0.2 at r=0.1-1 AU, as seen in Figure 5.1. The upper boundary of this layer corresponds to where CO becomes optically thick enough to self-shield, producing an environment were $C^{18}O$ continues to photodissociate while $C^{16}O$ does not, releasing free ^{18}O. Much of the free ^{18}O finds its way into water molecules, enhancing the $H_2^{18}O$ abundance, thus providing a lower ratio between H_2O and $H_2^{18}O$ (≈ 300). The most common ^{18}O destruction mechanisms come in the form of interactions with H_2 to form ^{18}OH and an extra H atom. ^{18}OH can then interact with an H_2 atom to form $H_2^{18}O$. The main cycle of ^{18}O once the chemistry has reached equilibrium is shown in Figure 5.2. The ratio returns to an ISM level at z/r$\approx$0.16 when

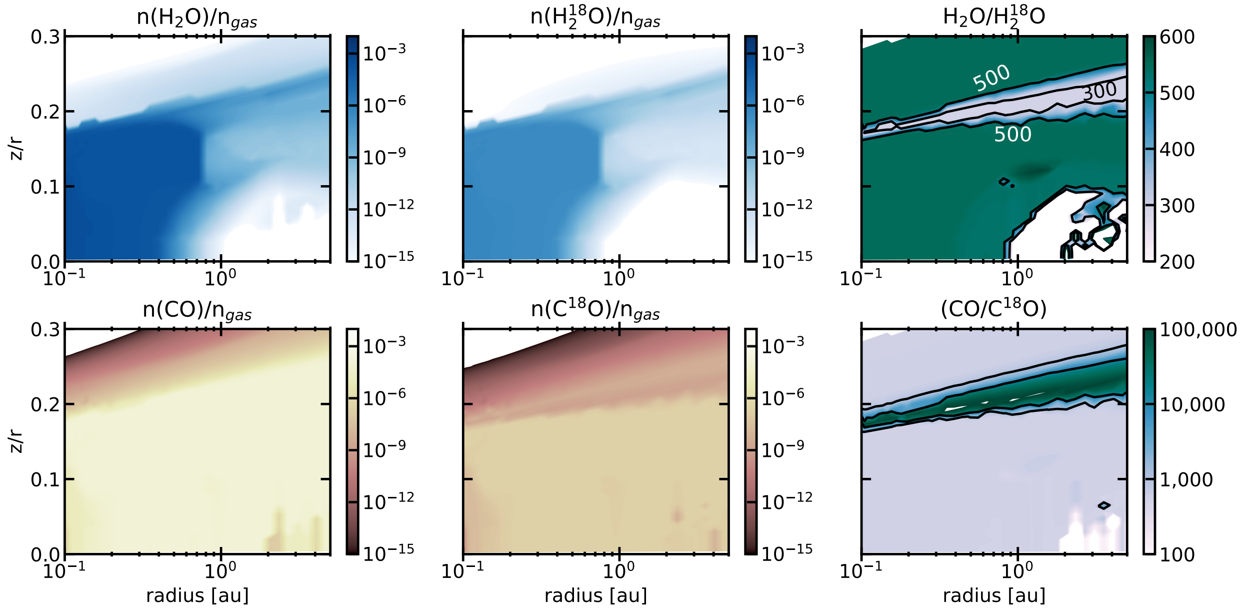

Figure 5.1 *The H_2O, $H_2^{18}O$, CO, and $C^{18}O$ abundance in units of (mol/cm^{-3})/n_{gas} throughout the inner disk (left and center plots), and the ratio between H_2O, $H_2^{18}O$ (top right) and CO and $C^{18}O$ (bottom right). At z/r$\approx$ 0.2 a unique region exits where $H_2^{18}O$ is enhanced and $C^{18}O$ is greatly depleted.*

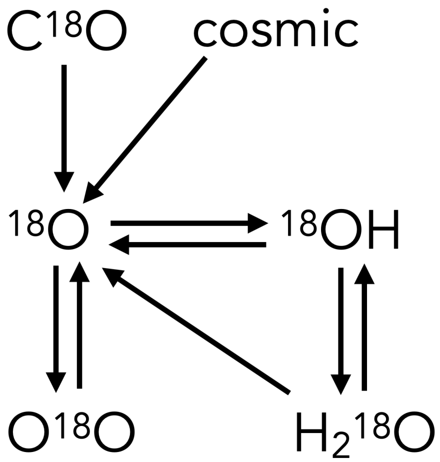

Figure 5.2 *The evolution of* ^{18}O *in equilibrium chemistry in the $H_2^{18}O$-enhanced region. Most of the oxygen comes from the dark cloud material originating from molecules like H_2O, CO_2, organics and silicates. In this region photodissociation of $C^{18}O$ provides and elevated abundance of* ^{18}O *which reacts with H and H_2 to quickly form ^{18}OH and $H_2^{18}O$. Because $C^{16}O$ is shielded, very little extra ^{16}O is included in this oxygen cycle, thus the relative increase in $H_2^{18}O$ production.*

$C^{18}O$ starts to be shielded, cutting of the supply of free ^{18}O. Near the same z/r, within 1 au, H_2O UV-shielding aids in shielding $C^{18}O$ to a point where its photodissociation rate is extremely low, many orders of magnitude lower than an environment where H_2O UV-shielding would be ignored.

Beyond $\sim$1 AU, the water abundance drops, yet a non-ISM ratio still exists. CO self-shielding continues to dominate, continuing to produce a ^{18}O enhanced environment, thus a continued low ratio of H_2O to $H_2^{18}O$, however there exists very little water vapor in the gas phase beyond r=1 au. The $H_2^{18}O$-enhanced region exists between a top-down vertical CO column of 10^{17} and $10^{19}\mathrm{cm}^{-2}$, an H_2 column of 10^{19} and $10^{22}\mathrm{cm}^{-2}$, and below an H column of $10^{21}\mathrm{cm}^{-2}$. This $H_2^{18}O$-enhanced region co-exists with large temperature gradients. Within 1 au, the thermal range from the bottom of this layer to the top is 500-2,000 K. Beyond 1 au the gradient is larger, ranging from 100-4,000 K.

We find that most Ly-α photons do not reach the H_2-dominated zone of the disk, including where the $H_2^{18}O$-rich region exits. The Ly-α emission feature is 25 times less bright in the radiation field of the disk at the location of the $H_2^{18}O$-rich region than it would be if the transfer of Ly-α photons was disregarded. Despite the decrease in overall UV flux, the $H_2^{18}O$-rich region exits over the same spatial extent of the disk compared to a model that does not account for Ly-α scattering off of hydrogen atoms. The limit at which scattered Ly-α photons have a decreasing contribution to the radiation field corresponds to a z/r≈0.25, or where the H-to-H_2 ratio is $\approx 10^{-5}$. While in this disk model Ly-α did not reach into the molecular disk, Bethell & Bergin (2011) found that the molecular disk can be enhanced with Ly-α relative to FUV photons using the detailed disk physical models by D'Alessio et al. (2006). In this study, we use the thermo-chemical calculation within DALI and a chemical network to determine the H-fraction throughout the disk, while Bethell & Bergin (2011) used an analytical expression taking into account photodissociation and self-shielding processes while leaving out chemical destruction or creation pathways for H_2 and H. This results in a H-to-H_2 transition within the work that exists higher in the disk as compared to Bethell & Bergin (2011). Additionally, in Bethell & Bergin (2011) the H-fraction drops to near zero while H_2 is dominate while in DALI there exists a population of free H atoms in the H_2-dominated region of the disk due to destructive chemical reactions. Thus, in the DALI disk, there are scattering events deep in the disk where in Bethell & Bergin (2011) there were none. The additional scattering events greatly increases the chance for Ly-α photons to be absorbed by dust.

5.3.2 $H_2^{18}O$ Emission Spectrum

The bulk of the water content exists within a radius of 1 au. We use DALI to calculate the flux contribution per cell for each emitted line. In order to determine which water lines will be of high interest, we run a quick non-LTE ray tracing program (Bosman et al., 2017, Append. B) that

Table 5.1. Transitions of $H_2^{18}O$ Observable with JWST

Transition	**Wavelength** (m)	$\mathbf{E_{up}}$ **(K)**	**A** **(s^{-1})**	**Weighted** **^{16}O/^{18}O** **Average**
$10_{(3,8)}$ - $9_{(0,9)}$	19.08	2072.3	0.83	520
$13_{(5,8)}$ - $12_{(4,9)}$	19.78	3772.5	8.9	500
$10_{(4,7)}$ - $9_{(1,8)}$	20.01	2265.3	1.9	510
$11_{(4,7)}$ - $10_{(3,8)}$	22.03	2725.3	4.4	490
$9_{(7,2)}$ - $9_{(4,5)}$	22.77	2581.7	0.031	540
$9_{(9,0)}$ - $8_{(8,1)}$	23.17	3165.9	41.	420
$9_{(6,3)}$ - $8_{(5,4)}$	26.83	2329.5	15.	410
$8_{(7,2)}$ - $7_{(6,1)}$	26.99	2265.6	21.	400

Note. — We quote each weighted average of the ^{16}O-to-^{18}O ratio with two significant figures following the level of certainty around the ISM value (assumed to be 550).

estimates the flux of water lines over the full extent of the MIRI wavelength range. We find that IR bright H_2O lines emit high up in the disk, proving to be optically thick across all IR wavelengths (see Bosman et al. 2022 in prep for detail). Isolated and bright $H_2^{18}O$ emission lines are rare, but a handful of lines will be accessible and distinguishable from H_2O with the MIRI instrument. We find eight distinct lines listed in Table 5.3.2 and highlighted in Figure 5.3. These lines exist between 19-27 µm; notably a region in MIRI with a lower sensitivity compared to shorter wavelength ranges.

Each $H_2^{18}O$ line emits from distinct heights within the disk, and may partially emit from the $H_2^{18}O$-enhanced region, thus when converting from $H_2^{18}O$-emission to a H_2O abundance, a ratio below that of the ISM should be used. One of the brightest and most isolated lines is the $H_2^{18}O$ $8_{(7,2)} - 7_{(6,1)}$ (27 µm) transition. We find that this transition starts to become optically thick and emits primarily in the enriched ^{18}O region. We find this to be true for seven out of the eight identified lines. The $H_2^{18}O$ $9_{(7,2)} - 9_{(4,5)}$ transition (22.77 µm) appears to primarily emit below the $H_2^{18}O$-enriched region, thus if using this line to determine a H_2O abundance, the conversion factor will be closer to ISM value of 550.

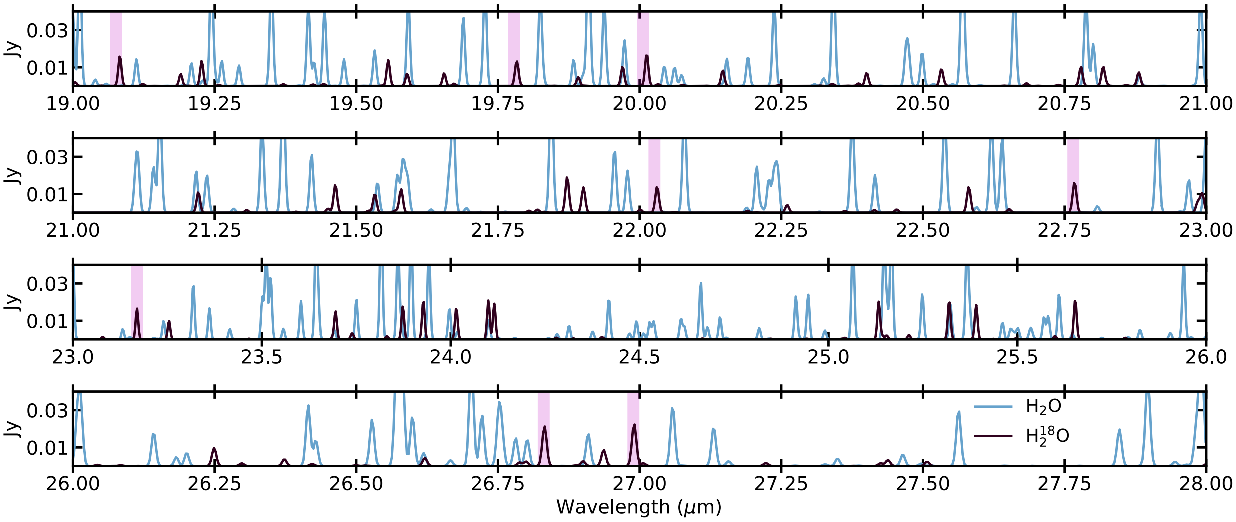

Figure 5.3 *The H_2O and $H_2^{18}O$ spectra as predicted from an AS 209 model including water UV-shielding and Ly-α contributions with 0.1 km s^{-1} velocity bins. Blue lines correspond to H_2O and dark purple with $H_2^{18}O$. $H_2^{18}O$ lines that are relatively bright and isolated from H_2O lines are highlighted.*

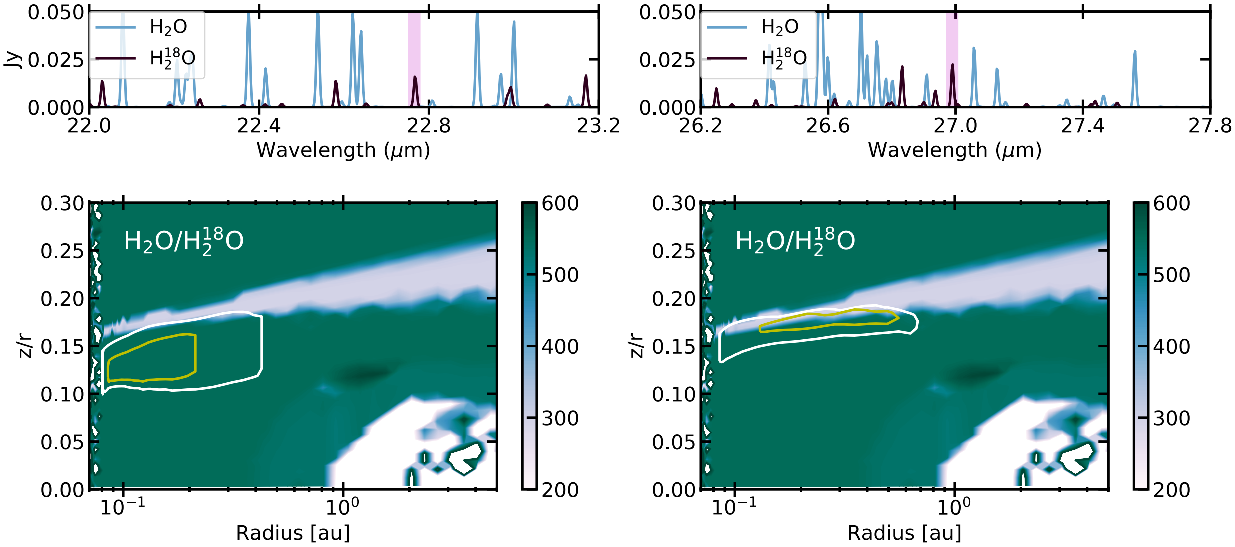

Figure 5.4 *Top: The overlapping spectra from H_2O and $H_2^{18}O$ focusing on a narrow wavelength regions within the MIRI instrument on JWST, focused on the $H_2^{18}O$ 27 μm line (left) and 22.77 μm (right) lines. The bottom plots show the 50% (yellow contour) and 90% (white contour) contribution regions for each line plotted over the H_2O-to-$H_2^{18}O$ ratio.*

5.4 Discussion & Analysis

5.4.1 Measuring H_2O abundance using $H_2^{18}O$ observations

A weighted ratio between H_2O and $H_2^{18}O$ must be used in order to extrapolate to an H_2O abundance and distribution using $H_2^{18}O$ observations. We have identified eight transitions of $H_2^{18}O$ that are observable with JWST, and calculate the weighted ratio of H_2O to $H_2^{18}O$ that should be assumed based on our AS 209 model, and the vertical layers where we predict the emission arises. We compute weighted averages of H_2O/ $H_2^{18}O$ using the relative spatial contribution from where each line is emitting from, as calculated by DALI.

Our first example comes from the $H_2^{18}O$ $8_{(7,2)} - 7_{(6,1)}$ transition at 27 µm. As seen in Figure 5.4, much of the emission from this line originates from the $H_2^{18}O$ enhanced region. We use the following equation to calculated a weighted $H_2O/H_2^{18}O$ value:

$$W = \frac{\sum_{i=1}^{n} w_i \chi_i}{\sum_{i=1}^{n} w_i} \tag{5.2}$$

where n is the number of cells in our model, w_i is the relative emission contribution in a cell, and χ_i is the $H_2O/H_2^{18}O$ value in a cell. Using this formalism, we find the average $H_2O/H_2^{18}O$ coming from this transition is ∼400. The $H_2^{18}O$ at 22.77 µm appears to emit from a drastically different region in the disk, thus its average $H_2O/H_2^{18}O$ is 540, nearly identical within the margin of error to the typically used ISM estimate. We list the calculated weighted averaged determined for the eight identified bright and isolated $H_2^{18}O$ transitions in Table 5.3.2. There is a general trend that transitions from smaller wavelengths trend towards a weighted average of 550. This trend arises from the Einstein A-coefficient associated with each transition. Transitions with lower A values are more likely to emit from deeper within the disk at higher gas densities, thus farther away from the $H_2^{18}O$-enhanced region. To reduce the uncertainty in the $H_2O/H_2^{18}O$ ratio, transitions associated with low Einstein A-coefficients could be preferentially used. These differences are small and up to a factor of two. However, chemical studies will be looking for enhanced abundances of water vapor in this region, perhaps supplied by pebble drift (Banzatti et al., 2020). To isolate these chemical changes we need to correct for effects that can be understood; water UV-shielding is one of these effects.

5.4.2 Corresponding CO Infrared Observations

In the $H_2^{18}O$-enhanced region, $C^{18}O$ abundance drops and the ^{12}CO-to-$C^{18}O$ ratio increases by upwards of four orders of magnitude. Measuring the ^{12}CO-to-$C^{18}O$ ratio using lines of CO that emit from this region could help confirm the presence of this ^{18}O-rich region and even calibrate uncertainties in the true ratio between H_2O-to-$H_2^{18}O$. The R and P branches for multiple vibrational transitions of CO and its isotopologues peak at $\sim$5 μm and are observable from the ground using high spectral resolution instruments such as *Keck* NIRSPEC and *VLT*'s CRIRES. The $C^{18}O$ column densities in the $H_2^{18}O$-rich region range from 10^{12}-10^{15} cm^{-12} and are predicted to produce optically thin $C^{18}O$ emission in the infrared. As summarized and expanded upon in Banzatti et al. (2022), over 100 T Tauri and Herbig disks have been observed with high-spectral resolution in the wavelength range of CO's vibrational lines which emit from $\sim$1000 K, corresponding to the temperature of the $H_2^{18}O$-enhanced region. In these studies only CO and ^{13}CO observations were reported, making it currently impossible to use these observations to corroborate our predicted ^{18}O-rich region within 1 au. The only work that set out to measure $^{12}CO/C^{18}O$ and $^{12}CO/C^{17}O$ is found in Smith et al. (2015). This study observed nine YSO systems, three of which were optically thick disks. These three disks show tentative increase in the $^{12}CO/C^{18}O$ well above the ISM-measured value, however it was noted at significant systematic uncertainties are associated with these measurements. A future study dedicated to deep observations of multiple disk systems could aid in upcoming MIRI observations of these regions, and put constraints on the ^{18}O-enhancement within the radial extent of planet-formation.

5.4.3 Impact of a different $^{16}O/^{18}O$ Ratio

Mass-independent fractionation of oxygen isotopes, with enrichment of the heavy isotopes, has been isolated within meteoritic material (Clayton et al., 1973; Thiemens & Heidenreich, 1983). The origin of these isotopic anomalies requires a specific mechanism that creates an ^{18}O (and ^{17}O)-rich environment as compared to the natal stellar nebula and envelope (Clayton, 1993). This fractionation must originate in the solar nebular disk or within the natal molecular cloud (Yurimoto & Kuramoto, 2004; Lyons & Young, 2005; Lee et al., 2008). CO self-shielding presents a mechanism to enrich gas in heavy isotopes, particularly on surfaces exposed to ultraviolet, as it selectively photodissociates $C^{18}O$ and $C^{17}O$ relative to CO producing gas enriched in ^{18}O and ^{17}O (Lyons & Young, 2005; Miotello et al., 2014). In this work, we find that the addition of H_2O UV-shielding not only continues the ^{18}O enrichment within the inner disk, but enhances it compared to results solely based on CO self-shielding. We find a depletion of $C^{18}O$ approaching a factor of 10^3 high up in the disk between 0.1-30 au at a $\sim$z/r=0.2-0.3. This is a reservoir rich with ^{18}O, enhancing the ^{18}O isotopologues for many different volatile species, including water vapor and ice.

Vertical mixing may act as a mechanism to deliver the ^{18}O-enhanced molecules to the planet-forming midplane. The "cold finger" effect (Stevenson & Lunine, 1988; Meijerink et al., 2009) has been proposed a mechanism that will transport water and other organics efficiently from the atmosphere of the disk to the midplane. Due to vertical mixing, water from the gaseous atmosphere can transport down to the midplane where it locked onto grains as ice. The cold finger effect has been used to reconcile models in which high water abundances are predicted, yet corresponding sub-mm observations exhibit non-detections (Du et al., 2015; Salyk et al., 2011b; Carr et al., 2018; Bosman & Bergin, 2021; Bosman et al., 2022b). Thus, while the $H_2^{18}O$-rich regions resides high up in the disk atmosphere, vertical mixing can bring a portion of this reservoir down to the midplane and enrich meteoritic precursors.

Lyons & Young (2005) explored a solution in the outer tens of au that suggested that meteoritic ^{18}O enrichment could be the result of CO self-shielding. In this model, oxygen atoms (enriched with heavy isotopes) produced via isotopic-selective CO self-shielding, are mixed downwards forming water ice via grain surface chemistry. These ices will need to be transported to the inner few au, perhaps by drift (Ciesla & Cuzzi, 2006). However, current meteoritic evidence suggests the inner solar system is chemically separated from the outer ($\gtrsim$ 5 au) parts of the disk between 1 Myr and 3-4 Myr, potentially due to early formation of Jupiter's core (Kruijer et al., 2017). Our model shows that this vertical layer of enhanced ^{18}O is placed directly into water in surface layers above the inner disk spatially closer to the region where meteoritic progenitors originate.

5.5 Conclusion

In this Letter, we implement H_2O UV-shielding and chemical heating in addition to CO self-shielding within a gas-rich disk environment. Focusing on the innermost region of the disk, a water vapor-rich reservoir exits within 1 au, and a $H_2^{18}O$ enhanced region exists where many water IR lines approach a $\tau = 1$. In this region, the H_2O-to-$H_2^{18}O$ ratio approaches 300, a significantly lower value than the assume ISM ratio of 550. We then seek use this context to provide insight into future JWST observations of $H_2^{18}O$ as it will act as a tracer for the abundance and distribution of gaseous H_2O in the main planet formation zone.

1. In our disk model, the H_2O-to-$H_2^{18}O$ ratio approaches 300 between a z/r$\approx$0.16-0.2 and inside 1 au due to CO self-shielding.

2. We identify eight bright and isolated $H_2^{18}O$ lines that can be used to access the abundance and distribution of H_2O. Transitions associated with higher Einstein A-coefficients, such as $H_2^{18}O$ $8_{(7,2)} - 7_{(6,1)}$ at 27 µm emit, primarily in the $H_2^{18}O$-rich region, thus the ratio between H_2O and $H_2^{18}O$ are less than the local ISM value of 550. Seven out of the eight identified transitions emit predominately from the $H_2^{18}O$-enhanced region, thus most observable $H_2^{18}O$ transitions with *JWST* will have an additional factor of uncertainty when converting $H_2^{18}O$ abundance to H_2O.

3. In this model Ly-α radiation does not penetrate down to the molecular-rich region of the disk in the case of our relatively thin and 0.0045 $M_\odot$ disk.
4. Vertical diffusive mixing, or the “cold finger” effect, could transport a significant amount of ^{18}O-rich molecules to the planet-forming midplane to be incorporated into pre-planetary materials that reside in the terrestrial planet-forming zone.

CHAPTER 6

Accounting for the Full Chemical Reservoir: A Look at FU Ori Objects with NOEMA

Abstract

FU Ori objects are young stellar objects which have undergone a recent ($<$100 yr) sudden accretion event, increasing the temperature of the surrounding disk and medium. This allows for molecules to exist in the gas that would otherwise be frozen out as ice on dust grains. Thus, probing the chemistry of these objects provides an incredibly unique opportunity to account for the full chemical reservoir of a protoplanetary disk. In this chapter, I present a survey of five FU Ori objects with the goals determining the mass of the disk and envelope structure with an optically thin isotopologue of CO and accounting for molecules across the frequency ranges of 202.7 - 210.8 GHz and 218.2 - 226.0 GHz. We find that $C^{17}O$ is optically thin in all five objects, and a varying degree of molecular complexity that doesn't appear to correlate with luminosity or outburst age.

6.1 Introduction

FU Orionis-type objects (FU Ori) have been theorized to be a common evolutionary phase between the Class I and Class II stages for low-mass pre-main sequence stars (Hartmann & Kenyon, 1996; Quanz et al., 2007; Vorobyov & Basu, 2015). An FU Ori object is classified as such after undergoing a sudden and extreme (several magnitudes) increase in brightness in optical and near-infrared wavelengths. This outburst has been attributed to short-lived (1-15 yrs) and massive accretion events, predicted to accrete up to 10^{-4} - 10^{-5} $M_\odot$/yr (Hartmann & Kenyon, 1996; Audard et al., 2014) onto the star. There are a number of mechanisms that could cause this sudden and fast accretion, including thermal or gravitational instabilities (Bell & Lin, 1994; Armitage et al., 2001; Boley et al., 2006), perturbations from a close-by massive companion (Bonnell & Bastien, 1992), or sporadic infall from the circumstellar envelope (Vorobyov & Basu, 2006; Vorobyov et al., 2013). Robust mass constraints on the disk and inner envelope are essential in determining what mechanism(s) is/are responsible for FU Ori outbursts. Gravitational instabilities require the disk to be relatively massive ($M_{disk}/M_* \gtrsim 0.1$) (Hartmann & Kenyon, 1996; Liu et al., 2016; Cieza et al., 2018) and thermal instabilities require regions of the disk that have high enough opacity to trap heat (Zhu et al., 2009). Regardless of the mechanism, FU Ori systems need to be massive enough to sustain the high accretion rate for many years. The environment and properties of FU Ori objects, focusing on the surrounding envelope and the embedded disk, are essential knowledge for a comprehensive understanding of this key stellar evolutionary phase and planet formation.

Mass is a difficult property to constrain for gas-rich young circumstellar disks. This is due to the fact that the vast majority of disk mass is in H_2 whose lowest energy rotational stages are non-emissve at typical disk temperatures ($\sim$ 20-100 K). The most common tracer of FU Ori disk mass has been millimeter continuum fluxes from the thermal emission of dust (Fehér et al., 2017; Cieza et al., 2018). Disk masses derived from dust observations rests on numerous assumptions to convert observed flux to dust mass and subsequent gas mass. This includes assuming the emission to be optically thin, a uniform temperature of the dust population, the knowledge of the dust optical properties at the given wavelength (i.e. dust mass opacity coefficient, κ_ν, and that the gas-to-dust ratio is the same as in the interstellar mediumAndrews & Birnstiel (2018)). Given the uncertainty in some of these quantities, a secondary mass tracer is necessary to constrain the disk mass.

CO is commonly used as a mass tracer for molecular clouds, protostellar envelopes, and protoplanetary disks, as it is a highly abundant molecule, is chemically stable, and easily detectable. The measured ratio of $CO/H_2 = 10^{-4}$ in the ISM, and is consistent with the ratio found in young Class 0/I disks (Zhang et al., 2020b) (see Figure 6.1). FU Ori objects present a unique laboratory for the purpose of mass determination of young stellar systems due to their recent outbursts. The outburst heats up the surrounding envelope, pushing out the CO snowline beyond its regular radial extent (Cieza et al., 2016), opening up more of the envelope's mass to be probed. The predicted CO snowline location for our sources lies between 142-485 au (see Table 2). The radial location of the CO sublimation front (temperature $\approx$ 20 K) during an FU Ori outburst can almost quadruple or even increase tenfold (at the intermediate stage of luminosity rise, and the outburst maximum respectively) (Molyarova et al., 2018).

^{12}CO is found to be optically thick towards typical molecular clouds and protoplanetary systems, thus can only provide an lower limit to the mass. We then turn to isotopologues of ^{12}CO. ^{13}CO and C^{18}O have often been used to probe higher density regions. C^{18}O emission (both the J= 1-0, and 2-1 transitions) has been assumed to be optically thin, and has been used as the mass tracer for FU Ori objects and other young stellar objects. Recent work has shown, however, that C^{18}O emission may not be completely optically thin. Available observations of FU Ori objects show that C^{18}O J=1-0 can have measured $\tau > 1$ (Fehér et al., 2017). Towards those same disks, emission from the brighter and more abundantly populated J=2-1 lines would have an even higher τ. Recent

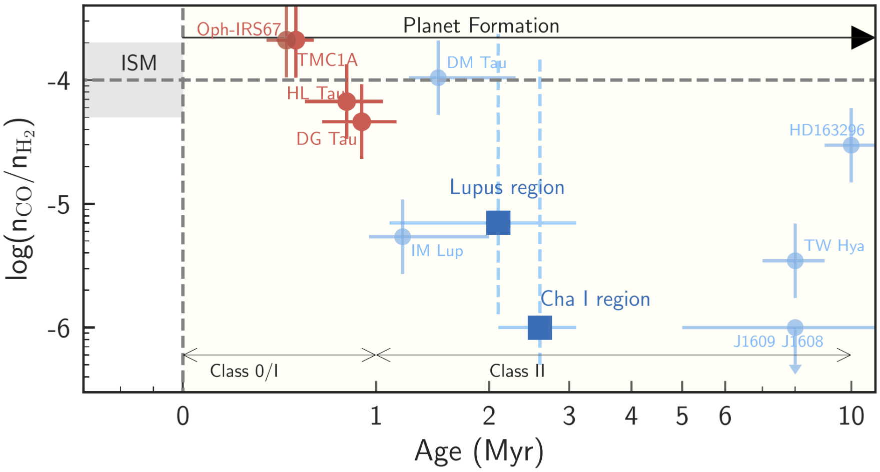

Figure 6.1 *CO gas abundance towards young stellar objects in their protostellar disk (red) and protoplanetary disk (blue). Circles indicate single sources, while squares indicate averages within a star forming region. Source: Figure 3 in Zhang et al. (2021a)*

observations with NOEMA towards three non-FU Ori Class I objects showed that $C^{18}O$ and $C^{17}O$ J=2-1 were both optically thick in the disk region, and $^{13}C^{18}O$ was required to reach optically thin emission levels (Zhang et al., 2020b). Using an optically thin tracer ($C^{17}O$ or $^{13}C^{18}O$) the total mass is determined by the flux, temperature (derived from $C^{18}O$), and assumed abundance of the optically thin tracer to H_2.

FU Ori objects also present a unique glimpse into the full chemical inventory available to actively forming planets. Planets form out of the refractory pebble material, volatile ices and gas. Due to the fact that most Class II protoplanetary disks are below 50 K, most of the volatile reservoir is frozen-out onto grains and thus unobservable in radio wavelengths. In FU Ori objects, a sudden burst of accretion will heat up the disk to high enough temperatures where the icy reservoir will sublimate off into the gas. We present NOEMA observations of five FU Ori-type objects with the primary science targets of ^{13}CO, $C^{18}O$, $C^{17}O$, and $^{13}C^{18}O$. We will use the optically thin tracer to estimate a "disk" and "cloud" mass for each source. Given the wide frequency range of NOEMA, we also have the opportunity to identify molecular transitions outside of CO, and find two distinct classes of molecular complexity among our sources. We discuss the implications of different mass extraction techniques and hypothesize solutions to the chemical complexity we see.

6.2 Source Selection

For our sample, we isolate sources that have been published and observed with NOEMA or ALMA in $C^{18}O$ J=1-0 or 2-1, and are located within the observational range of NOEMA (Fehér et al., 2017; Principe et al., 2018; Ábrahám et al., 2018). There are nine total sources that fit this criteria; we chose the brightest five sources, each with C^{18}O emission peaking directly on source. Within the northern hemisphere, these objects have the highest likelihood of a C^{17}O and ^{13}C^{18}O detection. Previous observations of the sources can be seen in Figure 6.2, and source properties can be found in Table 1 and 2. Our sources range from classic FU Ori objects (V1057 Cyg, V1735 Cyg, V1515 Cyg), to a peculiar source with unique spectral features but otherwise FU Ori characteristics (V1647 Ori), to an EXor/UXor type star with a higher period of luminosity variability (V2492 Cyg). None have quite reached a fully quiescent state, thus remain relatively luminous, between 13.9-150 L$_\odot$. See Tables 6.1 and 6.2 and Figure 6.2 for sources and properties.

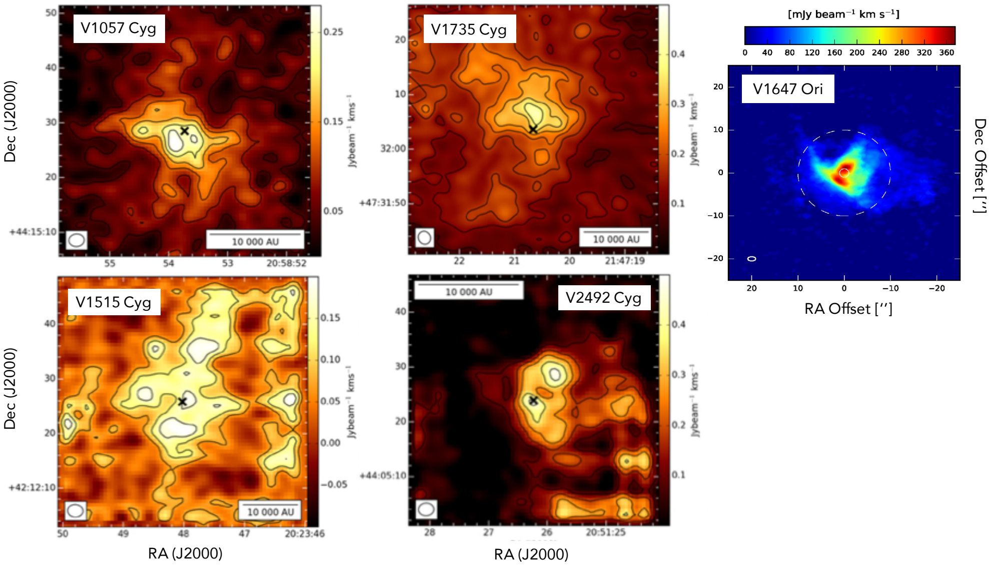

Figure 6.2 *Previous observations of C^{18}OJ=1-0 of V1057 Cyg, V1735 Cyg, V1515 Cyg, V2492 Cyg, and Fehér et al. (2017), and C^{18}OJ=2-1 observation of V1647 Ori Principe et al. (2018)*

6.3 Results

6.3.1 NOEMA Observational Details

These results are derived from NOEMA observations that took place July - October 2021 as a part of project S21AL. Each source was observed for ≈3.4 hrs with a beam sizes ≈ 1.″58 × 1.″50 (v1735 Cyg, V1057 Cyg) 2.″45 x 1.″69 (v1647 Ori) 1.″04 × 0.″92 (v2492 Cyg, V1515 Cyg). The initial round of data quality assurance and reduction was done with a staff member at NOEMA. The raw data was self-calibrated and CLEAN-ed using the GILDAS package MAPPING[1]. The first

---

[1] https://www.iram.fr/IRAMFR/GILDAS

Table 6.1. Source Properties

Name	Optical Spectral Type	Distance [pc]	Type	Outburst Date	References
V1057 Cyg	F7-G3	907^{+19}_{-20}	FU Ori	1970	1,2,3
V1735 Cyg	F0 - G0	691^{+35}_{-38}	FU Ori	1952 - 1965	1,2,3
V1647 Ori	M0	413^{+20}_{-22}	Peculiar[a]	1966-1967, 2004, 2008	1,2
V1515 Cyg	G2-G5	902^{+12}_{-13}	FU Ori	1950	1,2,3
V2492 Cyg	unknown[b]	804^{+24}_{-26}	UX Ori/EX Ori	2010, 2017	2,4,5

Note. — 1: Liu et al. (2018), 2: Gaia Collaboration et al. (2020), 3: Connelley & Reipurth (2018), 4: Hillenbrand et al. (2013), 5: Ibryamov et al. (2018)

[a] CO emission as opposed to absorption in NIR, otherwise it is similar to other FU Ori types

[b] lacks multiple emission lines in IR spectrum, no spectral type determined

step was to find the systematic velocity and correct the UV-tables to the accurate values, which aids in line detection. Next we isolate the continuum by zero-ing out every line and other feature such as dead pixels or end-of-band wiggles. With the continuum left over, we average over every ∼200 channels to compress down to a 2D continuum image. We then CLEAN that image over a number of iteration that leads to a plateau in the total flux in the image. Once the continuum image is found, the self-calibration can be done. In MAPPING there is a GUI that walks through the process. First we find a solution containing a number of iterations and clean components that leads to an increase in the S/N level and a plateau in total flux. That solution is then imposed on the original spectra that contains the emission lines. The self-calibrated image is then continuum-subtracted isolating the emission and other features as before when building the continuum image. For the goal of determining the mass of each source, we utilized the high-velocity resolution spectra and cleaned the ^{13}CO, C^{18}O, C^{17}O and ^{13}C^{18}O images separately, with different CLEAN solutions and masks. V1735 Cyg likely contains significant extended emission, as its solution contains beam artifacts that proved to be less strong if the smallest baselines were not included in the solution. However, to maintain consistency between sources and lines, the full NOEMA configuration including all baseline was used for the final results. To identify lines, the full lower side band (LSB) and upper side band (USB) were used and CLEAN-ed using the same solution. A mask was used for each CLEAN solution that encircled the central mass and decreased artifacts outside of where emission was known to exist. Final moment zero maps for each CO isotopologue along with associated opacities are shown in Figure 6.3-6.7.

Table 6.2. More Source Properties + Previous and Predicted Flux Measurements

Name	$M_{\mathrm{cont}}{}^{a}$ ($M_{\odot}$)	$M_{C^{18}O}{}^{b}$ ($M_{\odot}$)	$T_{\mathrm{env}}{}^{c}$ (K)	L_{bol} ($L_{\odot}$)	R_{CO} (au)	Observed $C^{18}O$ Flux [transition]
V1057 Cyg	0.59	0.32	16.4	100	246	79 [J=1-0]
V1735 Cyg	0.30	0.41	19.7	166	433	139 [J=1-0]
V1647 Ori	0.13	–	20	21	219	400 [J=2-1]
V1515 Cyg	0.04	0.23	11	103	142	147 [J=1-0]
V2492 Cyg	0.50	0.25	23.5	43	198	117 [J=1-0]

Note. — References: Fehér et al. (2017), Principe et al. (2018), Gaia Collaboration et al. (2020), Green et al. (2013), Postel et al. (2019), Aspin (2011)
[a] Envelope + disk mass derived from continuum observations, distance-corrected using recent Gaia data [b] Envelope + disk mass derived from $C^{18}O$ observations, [c] distance-corrected using recent Gaia data For V1057 Cyg, V1735 Cyg, V1515 Cyg, and V2492 Cyg, we list the average envelope temperature, for V1647 Ori a temperature value was not quoted for the gas population, nor was a temperature map publicly available, and so we list the average dust temperature used for the M_{cont} calculation. [d] (Connelley & Reipurth, 2018) and (Kóspál et al., 2013) for V2492 Cyg. [e]The radial location of the CO snowline as estimated by scaling relation using known TW Hya values: $R = 21\mathrm{au}(\mathrm{L_{bol}}/0.28\mathrm{L_{\odot}})^{0.5}$

6.3.2 Calculating Opacities

In our NOEMA sample we have successful observations of ^{13}CO, C^{18}O, and C^{17}O towards all five of our sources. Towards one of them, V1057 Cyg, we also have an unresolved detection of ^{13}C^{18}O. Our ideal total gas-mass tracer will be an optically thin transition of CO, thus we first calculate the optical depths of each of these isotopologues. The brightness temperature of a molecule is defined by:

$$T_B = T_{ex}(1 - e^{-\tau}) \tag{6.1}$$

where T_{ex} is the excitation temperature and τ is the optical depth. Taking the ratio between the brightness temperatures of two isotopologues will provide a relationship between the optical depths of the two lines:

$$\frac{T_B(^{13}CO)}{T_B(C^{18}O)} = \frac{T_{ex}(^{13}CO)(1 - e^{-\tau_{13}})}{T_{ex}(C^{18}O)(1 - e^{-\tau_{18}})}. \tag{6.2}$$

The excitation temperatures of each isotopologue of the same rotational transition can be assumed to be equal. And if you can assume that the ^{13}CO is optically thick, you can simplify this relation to

$$\frac{T_B(^{13}CO)}{T_B(C^{18}O)} \approx \frac{1}{1 - e^{-\tau_{18}}}. \tag{6.3}$$

One can then state that τ_{18} = τ_{13}/X where X is the abundance ratio between the two isotopes. Thus, the ratio of the optical depths is equal to the abundance ratio. in our case we use ratio values consistent with the ISM from Booth et al. (2019): ^{12}C/^{13}C=67, ^{16}C/^{18}C=444, and ^{18}C/^{17}C=3.8. If $R = \frac{T_B(^{13}CO)}{T_B(C^{18}O)}$ then you can express the optical depth of each isotopologue line as follows:

$$\tau_{13} = -\frac{444}{67}\ln(1 - \frac{1}{R}) \tag{6.4}$$

$$\tau_{18} = -3.8\ln(1 - \frac{1}{R}) \tag{6.5}$$

$$\tau_{17} = \tau_{18}/3.8 \tag{6.6}$$

Using the observed flux of each isotopologue, we calculated the optical depths for each observed line. We started with moment zero maps derived from our cleaned spectral cubes using bettermoments (Teague & Foreman-Mackey, 2018). Each moment zero map and optical depth map is found in Figures 6.3 - 6.7. All five sources show optically thin emission in the C^{17}O transition, while C^{18}O is marginally optically thick ($\tau \approx 1$ in most sources), and all ^{13}CO is optically

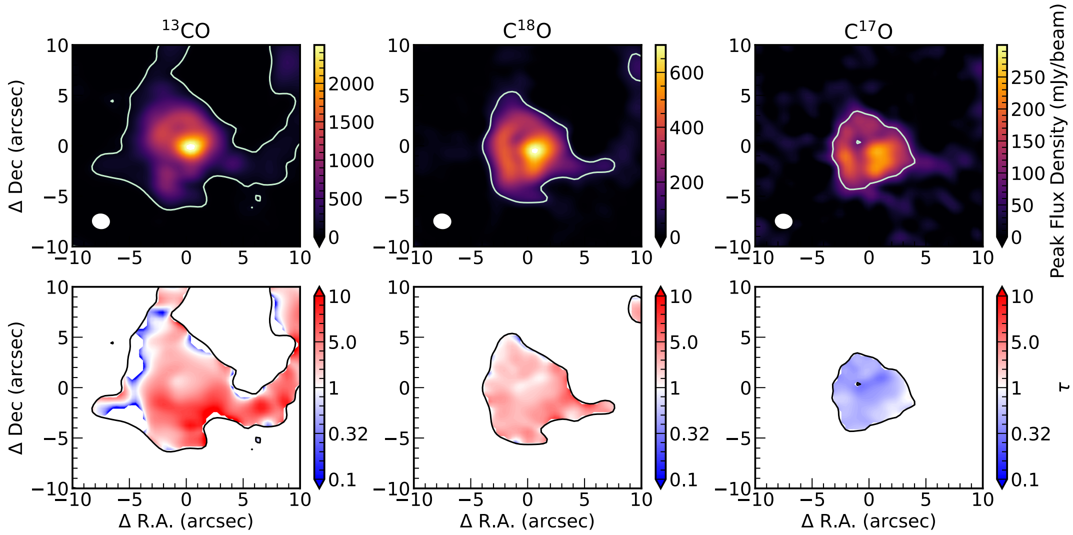

Figure 6.3 *The moment zero map of ^{13}CO, C^{18}O, C^{17}O J=2-1 emission towards V1057 Cyg (top row) and corresponding calculated optical depths (bottom row). The contour line overlaid on the fluxes correspond to the calculated RMS from the full data cube × 10, and only the optical depth within that region is shown.*

thick (see Figures 6.3-6.7). Previous mass estimates of these FU Ori objects were done using C^{18}O J=1-0, which may be optically thick based on these observations. We find C^{17}O to be a better mass tracer than C^{18}O in our spectral setup.

6.3.3 Calculating Masses

The mass of each source is calculated using C^{17}O emission. In an environment that is optically thin and in LTE, the column density of a molecule derived from a certain transition is defined as:

$$N_u^{\mathrm{thin}} = \frac{4\pi S_\nu \Delta\nu}{A_{ul}\Omega \mathrm{hc}}. \tag{6.7}$$

$S_\nu \Delta\nu$ is the integrated flux density, and the observed quantity that is calculated over each pixel over a certain frequency range. That frequency range is defined by the width of the C^{17}O emission profile in frequency space, which we uniformally defined to be limited by where the line hits the derived RMS from when a moment zero map is calculated. See Figure 6.8 for what part of the line the integrated intensity is calculated. A_{ul} is the Einstein-A coefficient that represents the rate in which a transition level is populated, and this is a constant for the C^{17}O J=2-1 transition and equal to $10^{-6.2}$ s^{-1} (source: splatalogue). Ω is the solid angle of the beam.

After the column density of the J=2-1 transition is calculated, an LTE assumption can easily

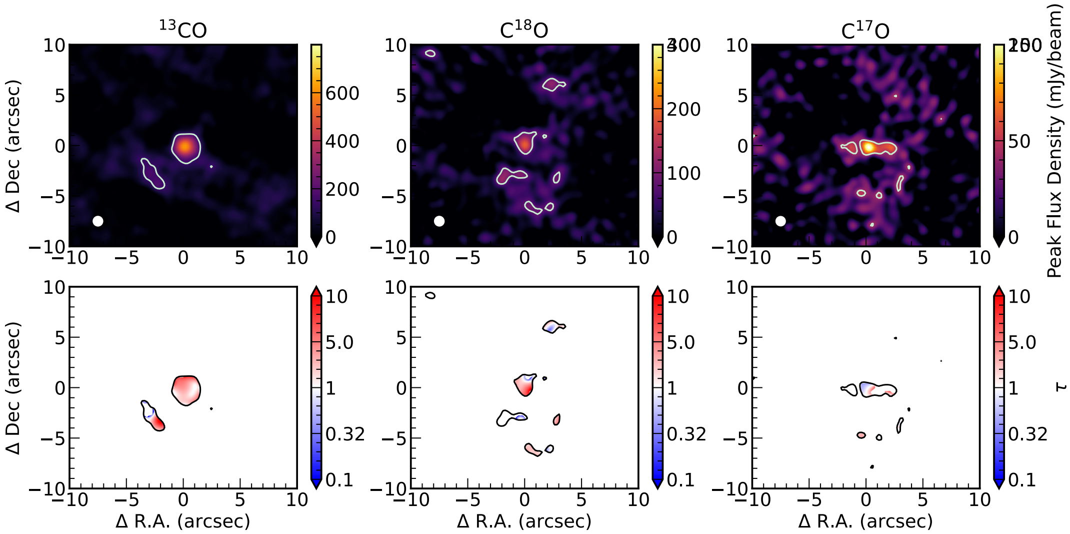

Figure 6.4 *Identical to Figure 6.3 but for V1515 Cyg*

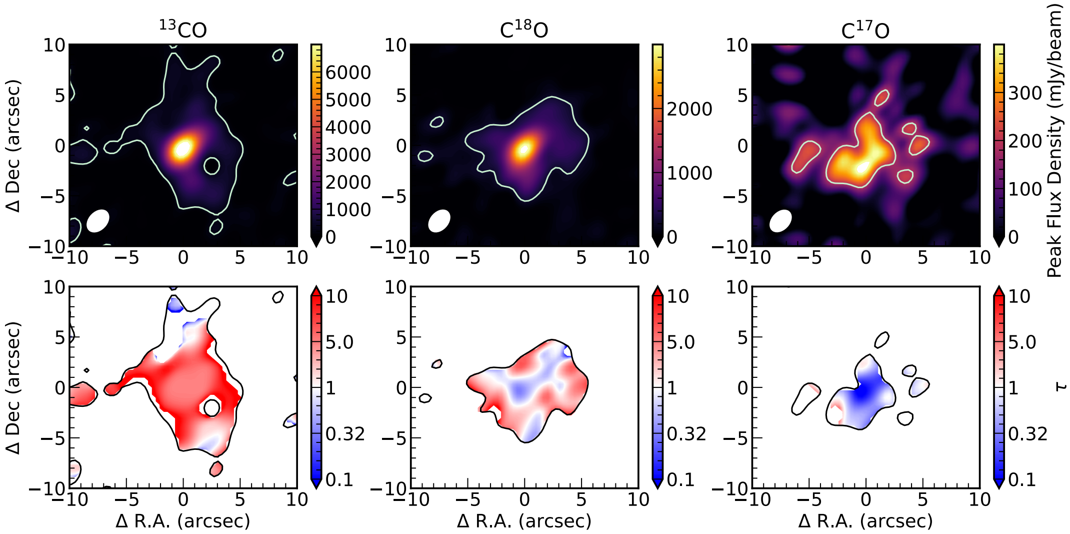

Figure 6.5 *Identical to Figure 6.3 but for V1647 Ori*